UiT
THE ARCTIC
UNIVERSITY
OF NORWAY

Department of Physics and Technology

A comparison between optical and SAR classification results for thin sea ice in Storfjorden

—

Cornelius Quigley

FYS-3900 Master's thesis in physics - May 2017

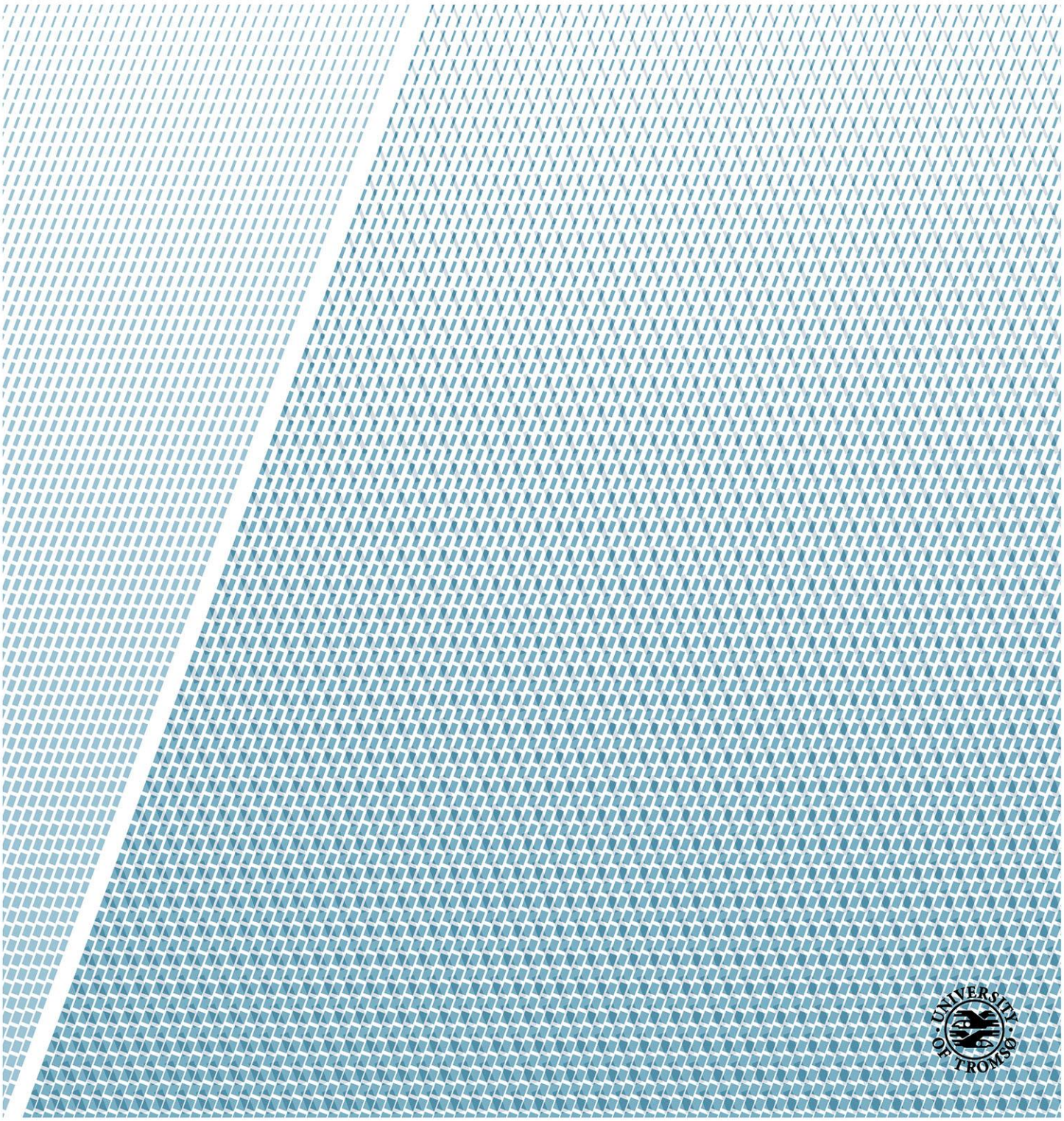

Abstract

According to the scientific consensus, the Arctic is currently in a state of unprecedented change. In recent years, climate change has been identified as the main cause of Arctic sea ice decline. For this reason, the need to have access to timely and cost effective data is of great importance. Remote sensing via Earth orbiting satellites offers extensive data coverage in areas that are typically inaccessible due to their remote location and extreme weather conditions. As well as this, having knowledge of sea ice conditions aids in exploration and navigation.

This thesis is concerned with classifying thin sea ice in Storfjorden using data acquired from both MODIS and Radarsat-2 in order to determine if data from either sources can be considered complimentary to each other. For this purpose, four comparisons were made. These included comparing MODISs 36 band data set with data from Radarsat-2 ScanSAR Narrow and Wide modes. As well as this, a comparison between MODISs 36 band data and data from Radarsat-2 QuadPol mode was made. HEM thickness measurements are also available from a helicopter campaign around the same time the data was taken. From laser altimeter data that accompanied the thickness measurements, a roughness characteristic was derived that was compared against the HEM measured thicknesses.

All MODIS data were screened for corrupted bands. The resulting bands were transformed into a new space via Principal Component Analysis (PCA). The first few components that contained most of the variance of the transformed data set were kept for segmentation. The SAR data was multilooked and feature extracted. The features that were chosen are a set of six basic features that have shown reasonably good results in the segmentation of sea ice previously and are known as the Extended Polarimetric Feature Space (EPFS). This set of features is composed of five polarimetric features plus a feature for non-Gaussianity. All features were segmented using a Mixture of Gaussian algorithm with Markov Random Field based contextual smoothing. The segmented results were compared visually by using all a priori knowledge about the fjord sourced from weather charts and scientific papers. The best results were found for the comparison between MODIS data and Radarsat-2 ScanSAR Wide data. This comparison shows that for a low number of clusters, the segmentation algorithm finds the same surface classes in the MODIS data as it does for the Radarsat-2 data. However, for progressively higher number of clusters of the MODIS data, MODIS reveals information related to the largescale ice types present in the fjord that the SAR is insensitive to.

A literature review of segmentation methods is also presented. This review was conducted by designing a set of search terms related to the segmentation of sea ice data in the Arctic. The results suggest that segmentation of optical data for Arctic sea ice is a relatively under studied area compared to SAR.

Acknowledgments

It would not have been possible to write this thesis without the support, wisdom and guidance of a great many people and I hope that the following words of acknowledgement can go some small way towards conveying the extent of my gratitude. Any and all insights were reached – to paraphrase Isaac Newton's famous saying – by standing on the shoulders of these giants.

Firstly, I would like to thank my supervisor Anthony Doulgeris for his seemingly endless reserves of time, advice and patience, not to mention for his generosity in allowing me to use his classification algorithm. His commitment to helping me see this project through has been so unwavering, and his own contribution to it so invaluable, that I could only understate both.

Likewise, I wish to thank Camilla Brekke for providing additional supervision and allowing me to benefit from her extensive knowledge and experience. I am also extremely grateful to Jacob Grahn, Tamesgan Yitayew and Thomas Kræmer for taking time away from their own research to offer me further advice and support. My thanks also go to Nick Hughes from the Norwegian Meteorological Institute for being on hand to answer various email queries and supply instrumental clarifications.

Finally, I would like to thank my family and friends for supporting me in a myriad of ways throughout the entire process. Whether this involved playing sounding board, providing much-needed distraction or simply sharing – and thus halving – a problem over coffee, the end result has undoubtedly been shaped by these acts of kindness and kinship. I hope one day I can return the favour.

Cornelius Quigley
Tromsø, May 2017

Table of Contents

List of Abbreviations

IR	Infrared
CSA	Canadian Space Agency
NASA	National Aeronautics and Space Administration
NSIDC	National Snow and Ice Data Center
NSR	Northern Sea Route
SAR	Synthetic Aperture Radar
EM	Electromagnetic
RS2	Radarsat-2
MODIS	Moderate Resolution Imaging Spectroradiometer
EPFS	Extended Polarimetric Feature Space
HEM	Helicopter-borne Electromagnetic
FYI	First-Year Ice
MYI	Multiyear Ice
r.m.s.	root mean square
TIT	Thin Ice Thickness
IST	Ice Surface Temperature
IFOV	Instantaneous Field of View
ULS	Upward Looking Sonar
RCS	Radar Cross Section
RAR	Real Aperture Radar
SLC	Single-Look Complex
MLC	Multi-Look Complex
ESO	Earth Observing System
FPA	Focal plane Assembly
ISB	Inter-Scan Banding
ARKTOS	Advanced Reasoning using Knowledge for Typing of Sea ice
EOSDIS	Earth Observing System Data and Information System

FOV	Field Of View
roi	Region of Interest
PC	Principal Components
CPR	Cross Pol Ratio
EPFS	Extended Polarimetric Feature Space
pdf	probability distribution function
FMM	Finite Mixture Modelling
MRF	Markov Random Field
MCTK	MODIS Conversion Toolkit

1 Introduction

1.1 The Importance of Studying Sea Ice

The use of satellites has allowed for the detailed monitoring of the Polar Regions in high temporal and spatial resolutions. Remote sensing of sea ice is conducted in the visible, infrared (IR) and microwave spectral regions. Each has its own capabilities and limitations for sea ice mapping and derivation of ice parameters (Johannessen, et al., 2007). This thesis is concerned with comparing classification results of thin sea ice in Storfjorden using a synthetic aperture radar (SAR) found on board the Canadian Space Agency's (CSA) Radarsat-2 (RS2) satellite and the National Aeronautics and Space Administration's (NASA) Moderate Resolution Imaging Spectroradiometer (MODIS) sensor, a spectroradiometer, found on board both the Terra and Aqua satellites.

The study of sea ice is a field of research that has gained much attention in recent years. Anthropogenic climate change, which has been hotly disputed for decades and dismissed as scientifically unsound is now accepted as a reality (Ho, 2009). According to (IPCC, 2008) eleven of the twelve years between 1995-2006 were the warmest years ever recorded since measurements began in 1850, up until the point of 2006. This report states that this temperature increase is widespread across the entire globe and that temperature increases are greater in the higher, northern latitudes. They cite observations of drastic changes in the Arctic cryosphere as evidence of this change. From satellite data taken since 1978, the annual average arctic sea ice extent has been reduced by 2.7% per decade with larger decreases over the summer months, amounting to 7.4% per decade, according to this report. In agreement with the IPCC, (Serreze, et al., 2006) report that climate models indicate the warming caused by the emission of atmospheric greenhouse gases will be first seen, and will be most pronounced, in the Arctic. The fundamental basis for these projections is that the loss of sea ice and snow cover exposes more sunlight absorbing surfaces, so that the initial heating effects will become more pronounced. This process is also outlined by (Vihma, 2014) and is described as a positive feedback system. The authors of this study conclude by saying that the Arctic, in its current state, is in a period of 'preconditioning' setting the stage for greater changes in the coming decades. They elaborate by saying that this preconditioning, is characterized by warming in all seasons, longer melt seasons and a thinning of the sea ice. This is also reported by (Galley, et al., 2016) who showed that multiyear ice that inhabits the Arctic is being replaced by thinner first year ice. Given that Arctic ice covers an area of 13.83 million square kilometres (according to the National Snow and Ice Data Centre (NSIDC), U.S., as of April 2017) any large scale changes in this region can have significant consequences for the rest of the planet. According to (Ho, 2009) because the Arctic sea ice is melting at an accelerated rate, an ice free Arctic during the summer months may be expected by mid-century.

Despite the obvious challenges climate change poses to humanity, there is another important, albeit unintuitive reason that gives great importance to the study of sea ice. The retreating of the Arctic sea ice, and consequently, the availability of more sea area for exploration has serious industrial and geopolitical consequences for the region. Sea ice restricts maritime activity in the Arctic regions so it is crucial for navigation to have access to synoptic environmental observations of the sea ice and ocean conditions and their forecasts (Ho, 2009). This will become more important as new shipping routes open up in the region. One of the positive consequences of the longer melt season and retreating sea ice mentioned above, is the opening up of the Northern Sea Route (NSR) and the Northeast Passage between Europe and Asia for ship transportation (Ho, 2009). In 2009, it was reported that two German merchant ships were able to traverse the NSR for the first time. Departing from Ulsan in South Korea, they were

able to sail to Rotterdam in the Netherlands via this route instead of taking the usual shipping route through the Suez Canal and the straits of Malacca, and thus saving fuel.

Thus, given the importance of studying the cryosphere in the northern latitudes, and given the fact that the arctic constitutes one of the harshest and most inaccessible environments on the planet due to extreme temperatures, heavy snowfall, strong winds and the polar night, remote sensing via satellites has proven to be an indispensable tool in the continuing campaign to study and understand the Arctic.

1.2 Objective and Contribution: The Complimentary Nature of SAR and Optical Sensors

In today's world, satellites that are orbiting the globe have the capability of acquiring data at different spatial, spectral, radiometric, angular and temporal resolutions (Chuvieco, et al., 2010). Data that is collected over these different domains have the possibility to provide a wealth of knowledge and insight about the scene of an investigation. However, due to a variety of reasons, the data that is collected by an individual sensor may not be sufficient to provide all the information that can be extracted from a particular scene, for a given application. The discipline of data fusion, which has gained interest within the last 25 years, deals with this problem (Pohl, et al., 1998) (Varshney, 1997). An interesting analogy is provided by (Hall, et al., 1997). In their study, they compare the use of data from multi-sensor satellite sources to the receptive capabilities of humans and animals. They describe how animals and humans have evolved the capability to use multiple senses to survive. For example, if an animal wanted to determine if a particular plant was edible, it could use its sense of smell or sight or perhaps both in conjunction to gain important information on the plants edibility. In the same way an animal would use its many senses, we can use the many types of multisensory data available to us, to help us to better understand an observed scene or to improve results for particular applications (Simone, et al., 2002) (Clement, et al., 1993). This is the main motivation of this study. More explicitly, the purpose of this study is to determine if data acquired form synthetic aperture radar (SAR) and optical satellites, can both be used to improve the insights gained from scenes that contain thin sea ice.

It is believed that the data from these two different sources can provide complimentary information given that these two sensors capture different physical aspects of a scene. SAR is sensitive to the geometric structure of a material, its dielectric properties and its roughness characteristics. Optical sensors are sensitive to reflective and emissive characteristics of a material, which both depend greatly on the materials thickness. As an example of the possible complimentary nature of these two sensors, consider the study conducted by (von Saldern, et al., 2004). Using data from an electromagnetic (EM) sounder, they collected sea ice thickness and surface morphology measurements in Storfjorden. The result of their study suggested that the thickness of the sea ice and the surface roughness are correlated. Intuitively, this makes sense, as young thin sea ice tends to be smoother than older, thicker ice. This is also confirmed in (Peterson, et al., 2008) who hypothesized that the ice thickness and ice roughness should be related due to the theory of isostasy. The authors of this study collected thickness and roughness data from a fix-mounted helicopter-borne electromagnetic (HEM) -laser system in the Canadian arctic**.** The authors of this study found relatively good agreement with isostasy assuming constant level ice thickness.

A major component of this study deals with the transformation of input data sets into representative features that can be operated on. This is referred to as feature extraction. When working with data from various sensors, feature extraction is usually one of the first steps that is undertaken in order to generate sensor specific information. This is important when generating features from SAR data and is covered

in section 7.3.10. The feature space that was chosen for the SAR data was the Extended Polarimetric Feature Space (EPFS) outlined in (Doulgeris, 2014). For the case of optical data, the feature generation stage might imply the use of a dimensionality reduction into a space that captures most of the variance of the data set. This is the process of Principle Component Analysis (PCA) and is covered in section 7.3.7.2. At this stage, the many bands that were obtained from sensor were reduced to a few, more manageable bands that were inputted into the algorithm. The obvious benefit of the feature generation stage is that it can make processing of the data set more efficient as it can reduce the amount of redundant information used, which limits the amount of processing time and memory that is needed to be dedicated to a specific task.

The integrated use of data from SAR and optical sensors for the investigation of sea ice is an emerging area of research. (Liu, et al., 2014) for example, generated texture characteristics from SAR data of sea ice and used a PCA method to fuse it with optical data represented in a hue-intensity-saturation (HIS) space. They found that this fusion of data method produces reasonable results in the discrimination of different sea ice types and implied their method was fit for operational use. Despite the fact that there seems to be little research in the area of fusing data from SAR and optical sources for the study of sea ice (probably due to challenges related to cloud cover and the polar night which are major limitations in the field of optical remote sensing) there is strong interest in the segmentation of data from these sensors individually. This is particularly true for SAR data. This will be outlined further in chapter 6.

The ultimate purpose of this study is to provide a comparison between SAR and optical data in order to determine if any complimentary information can be obtained about sea ice from either data type. The term complimentary in this case is taken to mean two things. 1) is it possible to derive similar information from either satellite scene, and 2) can one data type provide information about conditions in the scene that the other data type cannot? In short we are posing the question, can optical and SAR be considered as complimentary sources of information for the retrieval of information over thin sea ice? For this end, comparisons were made between MODIS data and various types of Radarsat-2 SAR data. In particular, three types of SAR data were used. They are; dual-pol ScanSAR Narrow and dual-pol ScanSAR Wide data, both of which are in operational use (Vulpiani, et al., 2012) and QuadPol data. Helicopter thickness data was also available around one of the dates of data acquisition from which a roughness characteristic was derived. This is used to infer a possible relationship between the thickness and the roughness of thin sea ice.

1.3 Structure of the Thesis

This thesis is structured into nine chapters including the introduction.

Chapter 2 provides an introduction to sea ice as a substance and is divided into 3 subsections. The first attempts to provide a discussion on the basic internal structure of sea ice and how it grows as well as outlining the relationship between sea ice and brine. The second focuses on the various types of ice that can be found in nature with emphases on ice that can be encountered in a single growing season. The third subsection provides a discussion on some of the fundamental aspects of sea ice that are most relevant to remote sensing from both the point of view of optical sensors and SARs.

Chapters 3, 4 and 5 provide information relating to the physics of SAR, optical sensors and EM birds respectively. The intent of these chapters is to outline and demonstrate the underlying physical properties by which these sensors operate and to demonstrate that at a fundamental operational level these sensors are vastly different.

Chapter 6 contains a literature review that was conducted with emphases on determining which methods in the past have been implemented for the purposes of segmenting see ice in both SAR and optical imagery. The systematic method that was adopted for conducting this review is outlined as well as the results obtained.

Chapter 7 outlines the methods that were adopted in this thesis. This chapter serves as a departure from the previous, more theoretical chapters and provides information relating to the study site. All methods related to the pre-processing of data as well as an outline of the segmentations algorithm that was used is also presented.

Chapter 8 presents the results for the three dates that were considered. The three dates are, 21 March 2013, which attempted to compare optical to ScanSAR Narrow data, 12 May 2013, which attempted to compare optical to ScanSAR Wide data and 12 May (MODIS measurements taken) and 10th May (RS2 measurements taken) 2013, which attempted to compare optical to QuadPol data. Data from each date is compared for two general cases. The first case considers how the two data types compare for a low number of clusters and the second case considers how the two data types compare for a higher number of clusters. The last comparison looks at thickness measurements taken from the EM bird and a roughness characteristic derived from it.

Chapter 9 contains concluding remarks and proposes future work that can be done in this field of research.

2 Sea Ice

Having an understanding of the basic internal mechanics and composition of sea ice can greatly aid the interpretation of remotely sensed images. This thesis is concerned with the comparison of sea ice as viewed in the microwave and optical domains (Note the optical domain, throughout this thesis, refers to the portions of the EM spectrum that MODIS covers). Thus, having knowledge about how sea ice appears when investigated from these two different points of view is of vital importance, as the physics that underpins these two data types differs greatly. First, a summary of the basic internal structure of sea ice is presented as well as the processes involved in its growth. This section will attempt to outline the basic relationship between sea ice and salt as well as what happens to the salt as sea ice forms and grows. This is followed by a brief description on the various types of ice that can be encountered, which is then followed by a discussion on the various properties of sea ice that are relevant for remote sensing and have an impact on remotely sensed images.

2.1 Basic Sea Ice Structure and Growth

2.1.1 Crystalline Structure of Sea Ice

Sea ice is a crystalline material whose characteristic properties depend on its crystal lattice structure from which it is composed. It is comprised mainly of water ice, sea salt ions, microalgae, gases, trace elements and other impurities (Hunke, et al., 2011). Water ice, is capable of taking on a multitude of different modifications depending on the temperature and pressure under which the water becomes frozen. When water undergoes freezing under equilibrium conditions at the Earth surface, the result is the formation of ice Ih, where 'h' indicates crystal symmetry in the hexagonal system (Petrich, et al., 2010). The molecules of H_2O in ice Ih have a tetrahedral arrangement about each other and have a six fold, rotational symmetry in the Basel plane, the plane of closest packing of atoms in a close-packed hexagonal crystal. An image showing the basic crystal structure of ice Ih is shown below in Figure 2.1

When in a liquid state, water molecules arrange themselves into hydrate shells surrounding impurities (e.g. sea salt molecules) due to the strong polarity of the water molecule. Sea salt ions however are not incorporated into the ice lattice structure when freezing occurs due to constraints on size and electric charge and are retained in the bulk ice material as brine inclusions. A brine inclusion is a liquid inclusion of salt dissolved in water (Petrich, et al., 2010). In fact, when Ih ice forms, most of the major ions that are present in sea water i.e. Na^+, K^+,Ca^{2+},Mg^{21},Cl^-,SO_4^{2-},CO_3^{2-} are also retained in these brine inclusions.

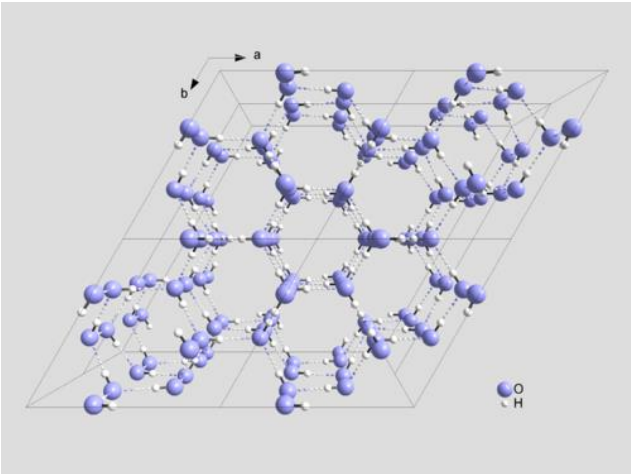

Figure 2.1: Crystal structure of ice Ih. The dashed lines represent hydrogen bonds. Image taken from Wikipedia.

2.1.2 Sea Ice Growth Process

Sea ice begins its life when a layer of seawater at the sea-air interface cools to a temperature of roughly $-1.8^{\circ}C$ under the condition that the underlying seawater has a salinity of roughly 33 ppt (Onstott, et al., 2004). The form that the growing ice takes is dependent on factors such as sea state, wind speed and air temperature at the time of ice formation. As there is a multitude of formation conditions that are conducive for the formation of ice, such as very cold temperatures to temperatures just under $0^{\circ}C$, calm sea conditions to highly agitated wave conditions, the presence of low or high wind speeds or weather or not it is snowing, there are a large number of ice categories that can be produced when ice begins to form (Onstott, et al., 2004).

Under calm conditions, long ice crystals tend to form into a thin, smooth layer of ice at the air-water interface. If wind and waves are present then these fine ice crystals become suspended in the water and frazil ice forms. As ice continues to grow, the action of the wind and waves causes the ice to coagulate and form a soupy layer called grease ice. When the ice reaches a thickness greater than about 1 cm, small clumps of ice will begin to form. This is commonly referred to as pancake ice and is characterized by raised rough edges due to constant between other pieces of ice (Onstott, et al., 2004). Pancake ice typically forms when the weather conditions are rough (Petrich, et al., 2010).

If temperatures are persistently cold, additional freezing along the bottom of sea ice bodies will occur as well as along the sides. Ice that is further grown under calm conditions can be described according to its visual properties which is related directly to its thickness. Such ice types include nilas ice, which has a thickness up to 10 cm, grey ice, which has a thickness between 10 to 15 cm and grey-white ice, which have thicknesses from 15 to 30 cm. After ice has reached a thickness of 30 cm, it is referred to as first-year ice (FYI). There is no upper limit to the thickness of FYI, but generally, it does not attain a thickness greater than 2.5 m (Onstott, et al., 2004). Figure 2.2 below outlines the ice growth process for sea ice in both calm and rough conditions.

If FYI has survived for more than one melt season, it is now referred to as Multiyear ice (MYI). MYI is distinguished from FYI by its greater thickness (usually 1.5 m or greater), its lower salt content (2.5% in MYI vs. 7.7% for FYI) and its thicker snow cover (0.4 m vs. 0.1m for FYI) (Hallikainen, et al., 1992). The types of sea ice that can be formed will be further elaborated in section 2.2.

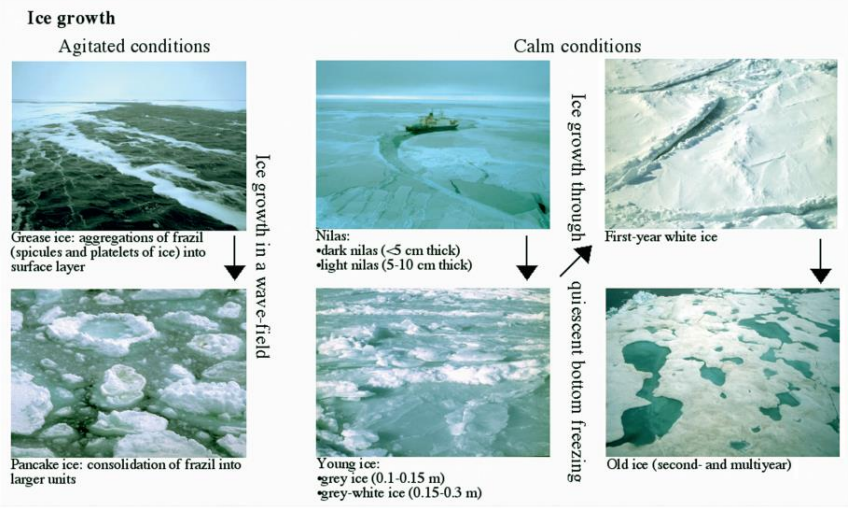

Figure 2.2: Pictures of sea ice taken at various stages of its development. As shown, if ice grows in agitated sea conditions pancake ice with rough, raised edges tend to form. Ice that forms in calm conditions will tend to coagulate into rafting, expansive sheets of ice. Image taken from **(Petrich, et al., 2010)**

2.1.3 Ice Growth and Brine Expulsion

As the ice grows downwards, salt ions are rejected from the ice and a thin layer of brine builds up ahead of the advancing ice-water interface. This thin layer of water is roughly a few millimetres to a few centimetres in thickness. This is due to the crystal structure of the ice as explained in section 2.1.1.

Due to the gradient of salt concentration between the brine and the underlying ocean, salt ions tend to migrate into the less saline ocean. The ice-water interface is at the melting/freezing temperature due to the condition of thermodynamic equilibrium but the presence of salt implies that the freezing point will drop as the salt concentration increases. The result is a heat flux from the relatively warmer water to the now colder interface (Petrich, et al., 2010).

If FYI survives through its melting season, some of the ice that was melted will further flush brine through the ice to the underlying ocean. According to (Peterson, 2017) the main cause of desalination of sea ice is gravity drainage and flushing of meltwater and melt ponds. As reported in this study, the process of gravity drainage will occur once the sea ice has been warmed to a critical temperature by the atmosphere, which increases the permeability of the ice. Plumes of brine are then triggered by meltwater below the ice, which then migrate towards the ocean.

Figure 2.3 shows this process when the ice has reached the critical temperature of T_c. Brines plumes are triggered by the meltwater below the ice by exposing brine pockets or by elevating the freezing point temperature T_f at the interface. This is the reason why the salinity of MYI is less than that of FYI.

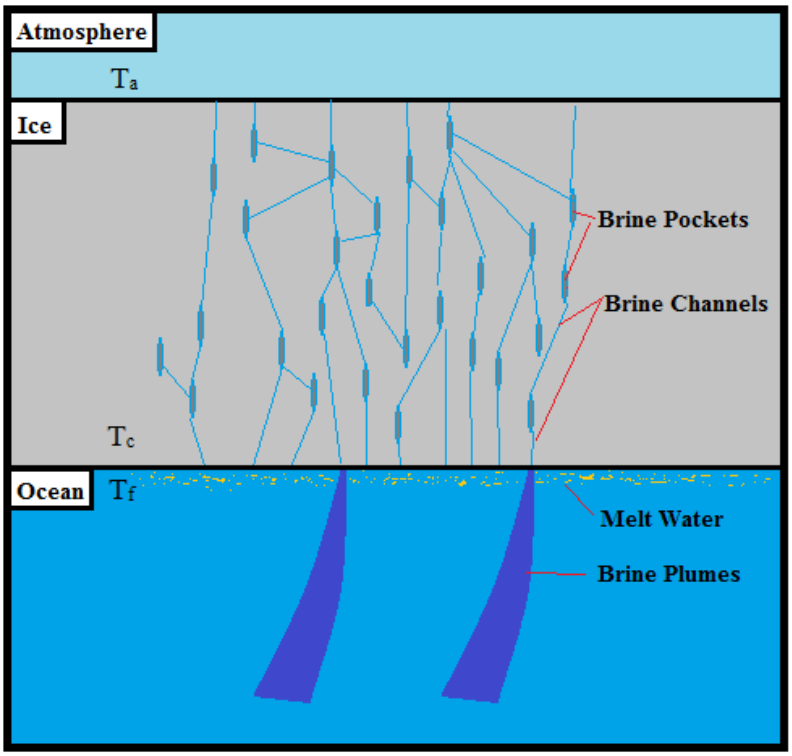

Figure 2.3: Diagram showing an atmosphere-sea ice- ocean set up. Brine inclusions can be seen in the ice as well as brine channels. Gravity drainage and flushing of meltwater and melt ponds cause brine plumes to transport ice into the underlying ocean.

2.2 Sea Ice Types

The previous section dealt with the basic crystalline structure of sea ice and the various processes it undergoes as it ages. This section attempts to describe the various types of sea ice that form along the life cycle of this material. Because the ice that is contained within Storfjorden, for the dates that this thesis is concerned with, is solely FYI (This is demonstrated in section 7.1) this section will deal mostly with the types of sea ice that are encountered in a single growing season and some of their basic characteristics. The aim of this section is to introduce the reader to some of the common nomenclature relating to sea ice. The following brief descriptions of sea ice are taken from (World Meteorological Organization, 1970) and (MANICE, 2005).

2.2.1 New Ice

New ice is a general term for ice that has recently formed and include ice types such as frazil ice, grease ice, slush and shuga. These types of ice are defined by a water mixture of fine ice crystals and are weakly frozen together.

2.2.2 Nilas Ice (up to 10cm)

Nilas ice is described as a thin, elastic crust of ice that is able to bend easily on waves and the swell. This ice type is described as having a matt surface and is up to 10cm thick. Subdivisions of this ice type include dark nilas, which is under 5cm in thickness and is dark in colour and light nilas, which is between 5 and 10cm in thickness and is described as being lighter in colour than dark nilas.

2.2.3 Grey Ice (10-15 cm)

This is a type of young ice. It is not as elastic as nilas and tends to break on swell. This type of ice usually rafts when under pressure.

2.2.4 Grey-white ice (15-30cm)

This is a type of young ice that is between 15-30cm. When under pressure this type of ice is more likely to form ridges than to raft.

2.2.5 FYI (30cm-2m)

This is sea ice that has grown since the last onset of the growing season.

2.2.6 Landfast ice

Landfast ice is a type of ice that forms and anchors itself to the coast. It is most prominent is the Arctic region during the months of October to June and tends to reach its widest extend during the late spring (Divine, et al., 2005). If it is thicker than 2m above sea level, it is then termed an ice shelf.

2.2.7 Drift/pack ice

This is a term used in a broad sense to describe an area of sea ice that is not landfast ice. When the concentrations of ice are high, i.e. 7/10 the term pack ice may be used more than drift ice.

2.2.8 Compact Ice

This is floating ice in which the concentration is 10/10 and little to no water is visible.

2.2.9 Very Close Ice

This is floating ice for which the concentration is 9/10 to 10/10.

2.2.10 Close Ice

This is floating ice for which the concentration is 7/10 to 8/10 and consists mostly of floes in contact.

2.2.11 Open ice

This is floating ice with concentrations of 4/10 to 6/10. It is characterized by the presence of many leads and polynyas. The floes are generally not in contact.

2.3 Physical Properties of Sea Ice Relevant to Remote Sensing

Remote sensing in both the Microwave domain and the Optical domain are reliant on a few basic characteristic properties of sea ice. For The Microwave domain, the modification of the radiation that is generated by the SAR is determined by the dielectric and roughness properties of the ice. In the optical domain, particularly for MODIS bands in the thermal infrared region of the spectrum, the observed signature is determined by the thickness of the ice. The following section gives a basic overview of the properties that can affect the return signal seen at the sensor.

2.3.1 Relative Permittivity/ Dielectric Properties

The relative permittivity, given as

$$\varepsilon = \varepsilon' - j\varepsilon'' \tag{2.1}$$

is a complex quantity that characterizes the electrical properties of a medium. Permittivity in general gives a measure of the resistance that is encountered when an electrical field attempts to form in a medium. The real part, ε', indicates the contrast with respect to free space and the imaginary part indicates the electromagnetic loss of the material. ε' is refered to as the dielectric constant and ε'' the dielectric loss factor. Note: $j = \sqrt{-1}$ (Hallikainen, et al., 1992).

The electrical properties that are inherent to a target have a critical impact on the backscatter of radiation from a SAR sensor and so have an effect on the intensity of the image that is formed. The aforementioned dielectric constant is regarded as a measure of a materials ability to store and transmit electrons and is closely related to conductivity (Chuvieco, et al., 2010).

Due to the fact that water has a dielectric constant roughly equal to 80, the amount of moisture present in a material can have a large effect on the returned signal. In general, the drier a material, the lower dielectric constant it will have.

2.3.2 Roughness Properties

According to (Chuvieco, et al., 2010) the roughness of a surface has a large impact on the intensity of the return signal. They state that, in general the rougher a surface is, the greater the return signal will be. The roughness is a characteristic that is highly dependent on the wavelength and the incidence angle of the radiation. One common criterion for the roughness is the Rayleigh criterion. This is given by the following equation

$$s_h \geq \frac{\lambda}{8} cos\theta \tag{2.2}$$

where s_h is defined as the standard deviation of the height of the surface in question, λ is the wavelength of the incoming radiation and θ is the incidence angle. A consequence of this criterion is that surfaces will tend to look smoother when they are illuminated with radiation of longer wavelength or greater incidence angle than the same surface would look at smaller wavelengths with a smaller incidence angles.

In a more comprehensive view on the subject, the surface roughness i.e. the small-scale geometric shape of the surface, can be statistically described by the root mean square height (r.m.s) h relative to a flat surface. In other words, how rough a surface is, is some measure of how different that surface is from a

plane of perfect smoothness. The r.m.s. roughness is good for getting rid of signs that cancel due to a surface distance being either above or below the mean plane. However, just using the r.m.s. can be deceiving, as it doesn't account for quick vertical variations as a function of horizontal position. Thus, we can also consider the horizontal roughness. This is a measure of how thin or sharp the peaks of a surface are. This is what the correlation length measures and can be thought of as posing the following question, in colloquial terms; 'for what distance, on average, would I have to walk so that I am not on the same bump? In short, the surface correlation function and the associated correlation length are parameters that are used for the horizontal description of the surface roughness (Hajnsek, et al., 2005).

(Drinkwater, 1989) conducted an experiment in the Labrador Sea and suggested that sea ice roughness can be approximated with a Gaussian correlation function for undeformed ice or an exponential correlation function for deformed sea ice. For a more comprehensive view on this subject with respect to sea ice, the reader is referred to (Paterson, et al., 1991), (Kim, et al., 1985) and (Onstott, 1992).

2.3.3 SAR scattering theory

According to (Onstott, et al., 2004) there are in total four parameters that will affect the scattering of SAR radiation off sea ice. They are;

- The roughness of the surface (discussed in 2.3.2)
- The dielectric constant of the ice, both real and imaginary components (discussed in 2.3.1)
- Dielectric discontinuities
- Orientation of the ice, and its features to the SAR

When looking at FYI, new ice and open water, the return to the radar is dominated by the roughness of the surface. This is due to the relatively high salt content of the material. When considering multiyear ice, the backscatter is determined by volume scattering as well as surface scattering and so the dielectric constant of the material is important. In section 7.1 it will be shown that the ice in Storfjorden during the time of data acquisition is FYI and so surface roughness will dominate any interaction between the sea ice and the impinging microwave radiation.

The relationship between the scattered radiation and the ice characteristics is shown below in Figure 2.4. This image shows how for open water and young ice types, surface scattering is dominant. Under these conditions, the ice is termed high-loss. For older ice, the interaction involves volume scattering. Under these conditions, the material is termed low-loss. As sea ice is a highly dynamic material, and is prone to wind and tide induced movement, ridging can occur especially if the ice is thicker than 15cm in thickness. Under these conditions the ridges act as dihedral reflectors and the backscatter to the radar can be significant. It should be noted that this strong backscatter effect is dependant of the orientation of the radar to the sea ice.

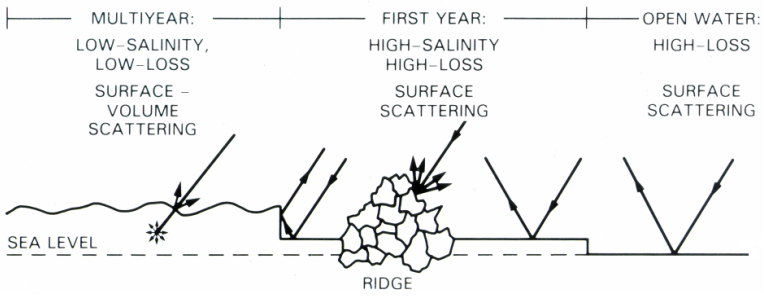

Figure 2.4: Diagram showing how different ice types and ice of different ages can affect the scattering of microwave radiation. Older sea ice tends to be less saline and so the scattering process is dominated by volume scattering as well as surface scattering. First year ice is more saline and so the scattering mechanism tends to be due to surface scattering. The same is true for open water. Ice that become deformed and that forms ridges can act as dihedral reflectors thus increasing the return to the radar. Image taken from **(Onstott, et al., 2004)**.

2.3.4 Ice thickness

2.3.4.1 Emissive Radiation

The relationship between thin ice thickness (TIT) and observed thermal infrared radiation has been well studied since the 70s. (Maykut, et al., 1971) (Groves, et al., 1991) (Yu, et al., 1996) (Yu, et al., 2001) (Adams, et al., 2012) describe a one-dimensional thermodynamic ice model that attempts to derive the ice thickness via an energy balance approach by using the ice surface temperature (IST) as a primary variable. This model takes into consideration contributions due to snow cover, the ice salinity, internal heating due to incoming solar radiation and latent heats of vaporization. Over the past 30 years, this model has been continuously improved. This energy balance model is described visually in Figure 2.5. The model is based on the condition that the entire energy flux entering the atmosphere, denoted by Q_A in Figure 2.5, is equal to the heat flux that is conducting through the ice. Mathematically, the model is given by the following equation;

$$Q_A = Q_0 - H_0 - E_0 \tag{3.3}$$

where Q_0 is the net radiation balance, H_0 is the sensible heat flux and E_0 is the latent heat flux. Ice will begin to form if the energy flux to the atmosphere, Q_A, is less than zero and the water temperature is at the freezing point.

The calculation of Q_0 is found via the equation;

$$Q_0 = L\downarrow - L\uparrow \tag{4.4}$$

Where both the downward and upward, longwave radiation, $L\downarrow$ and $L\uparrow$ are derived using the Stefan-Boltzmann's law;

$$L\downarrow = \varepsilon_a \sigma T_a^4 \tag{5.5}$$

Where ε_a is the atmospheric emission coefficient and σ is the Stefan-Boltzmann constant.

$$L\uparrow = \varepsilon_s \sigma T_{IST}^4 \tag{6.6}$$

Where ε_s is assumed to be 1 according to (Rees, 1993). T_{IST} is the ice surface temperature that is derived from the thermal infrared MODIS bands (band numbers 31 and 32).

H_0, E_0 are paramterized in a number of ways. Currently, the state of the art is the approach adopted by (Adams, et al., 2012). They implemented the approached defined by (Launiainen, et al., 1990) who outlined an iterative bulk approach, which included modelling the atmospheric stability using the Monin-Obukhov similarity theory.

The calculation of Q_I is given by;

$$Q_I = k_i\left(T_{IST} - T_f\right)/h_i \tag{7.7}$$

Where h_i is the TIT and T_f is the freezing temperature of sea water. This equation models the conductive heat flux through an ice layer without snow cover and can be modified to include a thin snow layer. (Wang, et al., 2010) elaborates on different modifications that are available in the literature for modelling snow cover.

In summary, the heat flux from the underlying ocean is modified by the sea ice. In an IST image, which is derived directly from the MODIS bands, the general rule of thumb is that thicker ice appears cooler and thinner ice appears warmer. As an example, consider Figure 2.6. This is an IST image and shows the sea ice that inhabits Storfjorden. The thicker landfast ice appears cooler and the open water appears to be the warmest. The drift ice appears to have an intermediate temperature. This image shows directly the relationship between the thickness of the ice and the upwelling thermal radiation.

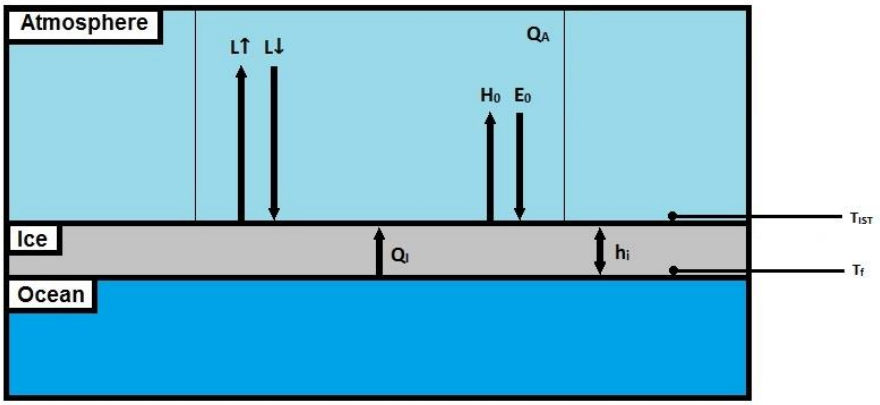

Figure 2.5: Diagram showing an atmosphere-ice-ocean set up. This model is based on the condition that the entire energy flux entering the atmosphere, denoted by Q_A, is equal to the heat flux that is conducting through the ice, denoted by Q_I.

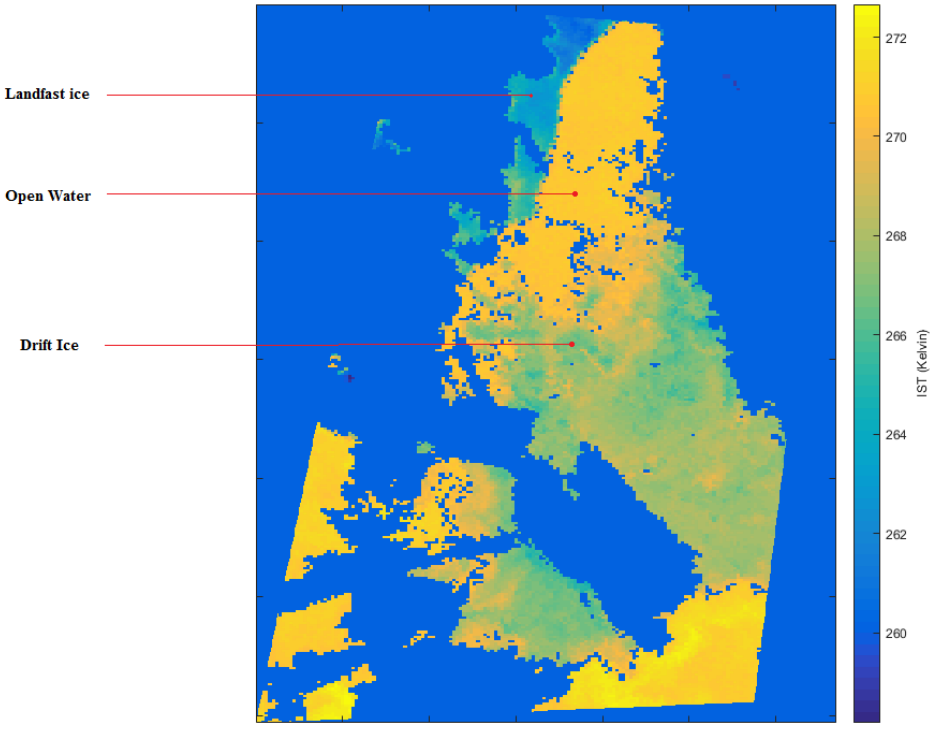

Figure 2.6: IST MODIS image of Storfjorden taken on 12 May 2013. Three distinct surface types can be distinguished in this image. The Landfast ice, which is expected to be the thickest, is observed to be the coldest. The open water is observed to be the warmest and the floating drift ice is observed to have intermediate temperature values. This image shows how the thickness of the overlying sea ice can effect the up-welling thermal radiation from the ocean.

2.3.4.2 Reflected Radiation

The albedo of a substance is defined as the fraction of incident radiation that a surface reflects. Radiation that is not reflected by the surface is absorbed (Coakley, 2003). A study conducted by (Perovich, 1998) found that the albedo for ice decreases as it gets thinner with open water having the lowest albedo of all and new dry snow having the highest albedo. This is confirmed by (Allison, et al., 1993) who in conducted a field study in the Antarctic by measuring the spectral albedos for nilas, young grey ice, grey white ice, snow-covered ice and open water between the spectral regions of 420 and 1000nm. They found that the albedos of various ice types rose with increasing ice thickness and snow thickness. An image showing their results is shown below in Figure 2.7. This figure clearly shows how the albedo of these various ice types changes the thicker the ice becomes across this spectral region.

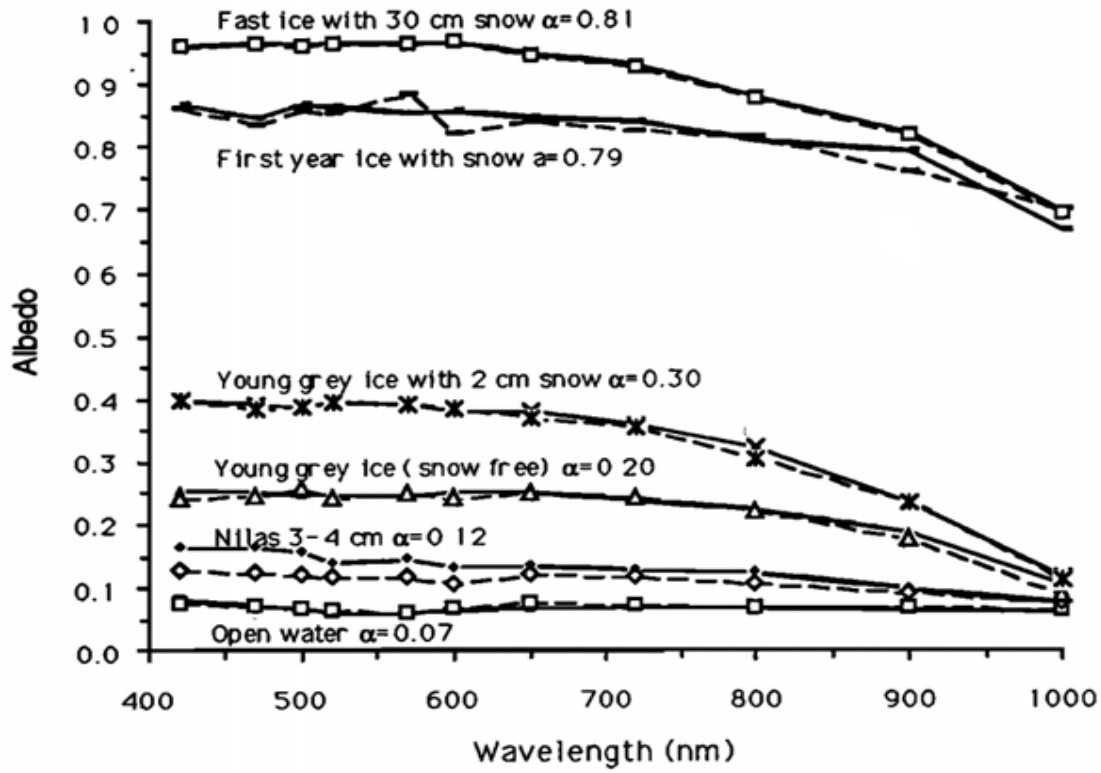

Figure 2.7: Graph showing the spectral albedo form various ice types between 420 and 1000nm of the EM spectrum. As can be seen the albedo of sea ice increases as the thickness of the ice increases. Open water was found to have the lowest albedo with a value of 0.07 and landfast ice with snow cover was found to have the highest albedo with a value of 0.81. Image taken from (Allison, et al., 1993).

3 Synthetic Aperture Radar Imaging

This chapter gives a brief introduction to the fundamental working principals of SAR. This includes a treatment of the radar equation, SAR imaging geometry, resolution, speckle and frequency. SAR polarimetry is also discussed as well as a short discussion on SAR sensors and their modes of operation. The objective of this chapter is to introduce the reader to the theory of SAR sensors. Chapter 4 does the same for optical imaging sensors.

3.1 Radar Equation

One of the most fundamental methods to describe the interaction of an electromagnetic wave with a target is via the radar equation. This equation expresses the relation between the power that is intercepted by a ground target and the power that is reradiated by the same target in the form of a scattered wave (Lee, et al., 2009).

The total power that is incident on a scatterer is given by the following formula

$$P_g = \frac{P_t A_g G_t}{4\pi R} \tag{3.1}$$

P_g is the power that is incident on the scatterer, P_t is the power transmitted by the sensor, A_g represents the effective area presented by the scatterer and G_t is the gain of the antenna. The factor of $\frac{1}{4\pi R}$ represents the decrease in power density over the slant range R.

Conversely, the expression for the total power received at the sensor is given by

$$P_r = \frac{P_{g'} A_t G_g}{4\pi R} \tag{3.2}$$

Where P_r is a quantity representing the total power received at the sensor, A_t is the effective area of the receiver which is given by $\frac{G_t \lambda^2}{4\pi}$ where λ is the wavelength. $P_{g'}$ is a quantity reprsenting the power that is reradiated by the ground target and G_g expresses the gain of the ground in the direction of the sensor.

Using the two equations for P_g and P_r it is possible to derive a general relationship between P_r and P_t resulting in what is known as the radar equation

$$P_r = \frac{G_t^2 \sigma \lambda^2}{(4\pi)^3 R^4} P_t \tag{3.3}$$

σ is the radar cross section (RCS) and is defined as the cross section of an equivalent ideal isotropic scatterer that generates the same amount of scattered power density as the object in question (Lee, et al., 2009). The RCS is thus given by

$$\sigma = 4\pi r^2 \frac{\left|\vec{E}_s\right|^2}{\left|\vec{E}_I\right|^2} \tag{3.4}$$

Where the numerator and denominator of the above equation indicate the power of the scattered and incident electromagnetic waves respectively. r indicates the distance between the target and the receiving system.

3.2 Imaging Geometry and resolution of SAR systems

In SAR imaging there are two directions that need to be defined. The first is the *azimuth* direction, and is defined as the direction of motion of the sensor platform. The second is the *range* direction, and is defined as the direction perpendicular to the motion of the sensor platform.

The sensor illuminates a strip of ground to one side of the nadir track of the platform. The side looking configuration of the SAR system is necessary in order to eliminate any ambiguities that might arise from two symmetric equidistant points (Elachi, et al., 2006).

The portion of the EM spectrum that SAR operate in ranges from centimetres to many tens of meters. For a real aperture radar (RAR), this poses a problem of resolution when working in this region. Consider the following equation for the resolution of a real aperture system

$$R_S = \frac{\lambda h}{d} \tag{3.5}$$

where λ is the wavelength of the radiation, h is the height of the observation and d is the diameter of the antenna. Due to the fact that when we have a large value for h, as we do for space borne antennas, having a reasonable resolution would require an unrealistically large antenna. This problem can be remedied by artificially synthesising a virtual antenna. This is the fundamental concept behind SAR (Chuvieco, et al., 2010).

The method by which a SAR's virtual antenna is synthesized is via the Doppler effect, which is the change is observed frequency caused by the relative motion between the sensor and the target. The radar emits repeated pulses of energy at microwave frequencies toward the ground. As the platform orbits, the pulses that are emitted are scattered back in the direction of the satellite with different frequencies than they originated with. According to (Elachi, et al., 2006) if it is known from where the backscattered radiation was emitted, the discrimination of the surface being observed would be as accurate as observing the scene with an antenna the size of the initial and final phases of the satellite orbit. Thus, in accordance with equation 3.5 above, an antenna that provides high spatial resolution can be achieved.

As an example consider a radar sensor that is moving with a velocity v and with a length L. The footprint of the main beam will be

$$\mathcal{L} = \frac{2\lambda h}{d} \tag{3.6}$$

As the sensor moves, consecutive echoes are recorded at various points $X_1, X_2, X_3, \dots, X_n$ along the line of flight. This is shown below in Figure 3.1. It can be seen that the largest array that can be realized is $\mathcal{L}$. The beam width of this array is

$$\theta_s = \frac{\lambda}{\mathcal{L}} = \frac{L}{2h} \tag{3.7}$$

The resulting footprint on the ground will be

$$X_a = h\theta_s = \frac{L}{2} \tag{3.8}$$

This quantity is known as the Azimuth resolution. This is an unintuitive result as it suggests that the resolution in azimuth does not depend on the height of the sensor above the ground and that a finer

resolution can be achieved by using a smaller antenna. The explanation is as follows; if the sensor is further away, the footprint on the ground is larger, thus a larger synthetic array can be formed. This implies a finer synthetic beam can be generated which counteracts the increase in distance. If the antenna is smaller, the footprint is larger and so too will be the synthetic array. This implies a finer synthetic beam and thus a more fine resolution (Elachi, et al., 2006).

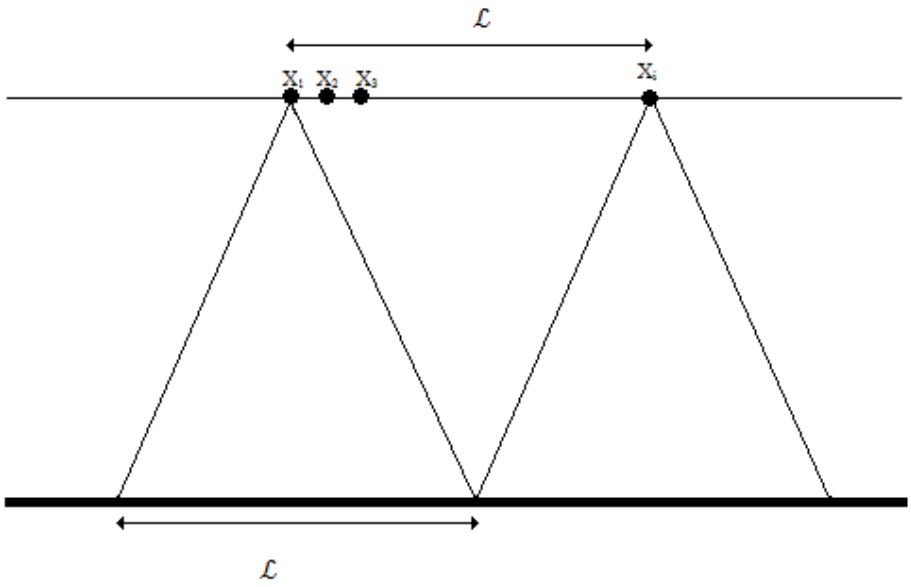

Figure 3.1: Method of forming the synthetic array. The array is formed by moving a single antenna along the track above which takes measurements at each point X_i. The length of the synthesized antenna is L.

The resolution in the range direction will have a different formulation than the one in the azimuth direction. Two points can be distinguished in this direction if the pulses scattered from these points returning to the sensor arrive at different times. More strictly, these two points can be distinguished if their ground distances are greater than half the pulse length. It needs to be greater than half, as the pulse needs to travel the intermediate distance between the two points and back. This discrimination is also dependant the angle of incidence θ. This implies the pulse should be as short as possible to receive a fine resolution. The fundamental problem with this is that we need to increase the amplitude in order to keep the SNR high. It is difficult to design such systems that short, high amplitude pulses. In order to solve this the emitted pulses are modulated (Elachi, et al., 2006). In summary the radar range resolution is given by

$$X_r = \frac{c}{2Bsin\theta} \tag{3.9}$$

where c is the speed of light, θ is the local angle of incidence and B is the spectral bandwidth. The bandwidth has the form $B = 1/\tau$ where τ is the pulse length.

3.3 Frequency

The frequency of operation of a SAR is a very important consideration in the design phase of a sensor. This is due to the fact that radiation of varying wavelengths will interact differently with the surface roughness and dielectric properties of the target in question. The EM waves of sensors that employ radiation of short wavelengths will interact with small surface elements in a target and will have low penetration depths and will also be sensitive to heavy rain. The opposite is true for signals of longer wavelength which tend to have higher penetration capabilities and are less prone to interference from atmospheric constituents.

Radars typically operate in the microwave region of the electromagnetic spectrum with wavelengths ranging from 1 mm to 100 cm (0.3 GHz – 300 GHz). This region is further divided into smaller bands. The Ka-, K, and Ku- bands have the shortest wavelengths and range between 0.75 and 2.5 cm. Larger bands, such as the X, C, S, L and P bands range from 2.5 to 120cm. Table 1.1 shows the microwave frequency bands just cited.

Table 3.1: Microwave frequency bands as outlined in **(Moreira, et al., 2013)**

Frequency Band	**Ka**	**Ku**	**X**	**C**	**S**	**L**	**P**
Frequency [GHz]	40-25	17.6-12	12-7.5	7.5-3.75	3.75-2	2-1	0.5-0.25
Wavelength [cm]	0.75-1.2	1.7-2.5	2.5-4	4-8	8-15	15-30	60-120

3.4 Speckle

Speckle is a characteristic of coherent imaging systems and occurs due to the coherent interference of waves that are reflected from many scatterers in each resolution cell of a scene. As a result, pixels within an image will display variations from one pixel to the next that manifests itself as a granular like pattern. This pattern is often called ‘’salt and pepper’’ noise. Since this noise is due to the constructive and destructive interference of waves, it is not noise in the classic sense, but rather the radar signature of a point on the surface under the given circumstances and also carries information (Lee, et al., 2009), (Oliver, et al., 2004). A consequence of this is that speckle cannot be removed by an increase in the transmit power of the signal as it has a multiplicative character, meaning its variance increases with its intensity (Moreira, et al., 2013).

Speckle can occur even within uniform areas. This greatly complicates the analysis of SAR images and can serve to reduce the effectiveness of image segmentation and classification techniques. A common process of reducing speckle in SAR images is *multilooking*. Multilooking is the process of dividing a full aperture into a *N* sub apertures (known as looks) and then processing each look independently to form *N* intensity or amplitude SAR images. The *N* images are then summed together to form an *N*-look SAR image (Lee, et al., 2009). This can be done in the image formation stage or can be done in the spatial domain by averaging over a neighbourhood of pixels. Despite the fact that multilooking causes a reduction in the resolution of the image, it greatly increases the interpretability of a SAR image. Speckle suppression will be discussed in more detail in section 7.3.9.

3.5 SAR Polarimetry

In contrast to optical sensors that can image over a broad portion of the EM spectrum, SARs generally only image over a small bandwidth. What SARs lack in radiometric resolution however, they make up for in their ability to measure and interpret the polarization of transverse EM waves. In the following section a description of SAR polarimetry is given. In order to present a complete and through introduction to SAR polarimetry the following section begins with a brief discussion on Maxwell's equations and then proceeds to describe the polarization states for transverse EM waves. The following discussion is as presented as it is given in (Oliver, et al., 2004).

3.5.1 Monochromatic Electromagnetic Plane Waves

The time-space behaviour of electromagnetic waves can be modelled by Maxwell's equations given as

$$\vec{\nabla} \wedge \vec{E}(\vec{r},t) = -\frac{\partial \vec{B}(\vec{r},t)}{\partial t} \tag{3.10}$$

$$\vec{\nabla} \wedge \vec{H}(\vec{r},t) = \vec{J}_T(\vec{r},t) + \frac{\partial \vec{D}(\vec{r},t)}{\partial t} \tag{3.11}$$

$$\vec{\nabla} \cdot \vec{D}(\vec{r},t) = \vec{\rho}(\vec{r},t) \tag{3.12}$$

$$\vec{\nabla} \cdot \vec{B}(\vec{r},t) = 0 \tag{3.13}$$

where $\vec{E}(\vec{r},t)$, $\vec{H}(\vec{r},t)$, $\vec{D}(\vec{r},t)$ and $\vec{B}(\vec{r},t)$ are the electric field, magnetic field, electric induction and magnetic induction of the wave respectively. The total current density is given by $\vec{J}_T(\vec{r},t) = \vec{J}_a(\vec{r},t) + \vec{J}_c(\vec{r},t)$ where $\vec{J}_a(\vec{r},t)$ represents the source term and the conduction current density, $\vec{J}_c(\vec{r},t) = \sigma\vec{E}(\vec{r},t)$ is a quantity that depends on the conduction of the medium σ (Lee, et al., 2009). These field and induction relations can be related via the following equations

$$\vec{D}(\vec{r},t) = \varepsilon\vec{E}(\vec{r},t) + \vec{P}(\vec{r},t) \tag{3.14}$$

$$\vec{B}(\vec{r},t) = \mu\left[\vec{H}(\vec{r},t) + M(\vec{r},t)\right] \tag{3.15}$$

where $\vec{P}(\vec{r},t)$ and $M(\vec{r},t)$ are the poarization and magnetization vectors and ε and μ are are the mediums permitivity and permeability respectively.

The equation of propagation of an EM wave, for a linear medium, is found by inserting equations (3.10) - (3.13) and equations (3.14) and (3.15) into the vector identity $\vec{\nabla} \wedge \left[\vec{\nabla} \wedge \vec{E}(\vec{r},t)\right] = \vec{\nabla}\left[\vec{\nabla} \cdot \vec{E}(\vec{r},t)\right] - \Delta\vec{E}(\vec{r},t)$. The equation of propagation is thus given by

$$\Delta\vec{E}(\vec{r},t) - \mu\varepsilon\frac{\partial^2\vec{E}(\vec{r},t)}{\partial t^2} - \mu\sigma\frac{\partial\vec{E}(\vec{r},t)}{\partial t} = \frac{1}{\varepsilon}\frac{\partial\vec{\nabla}\rho(\vec{r},t)}{\partial t} \tag{3.16}$$

If the analysis is constrained to monochromatic waves of constant amplitude the right side of equation (3.16) is assumed to be null $\frac{\partial\vec{\nabla}\rho(\vec{r},t)}{\partial t} = 0$. This is equivalent to assuming that the propagation medium is free of mobile charges, which is the case for plasmas.

Equation (3.16) can be simplified by considering the complex expression $\underline{\vec{E}}(\vec{r})$ for $\vec{E}(\vec{r},t)$ given as

$$\vec{E}(\vec{r},t) = Re\left[\underline{\vec{E}}(\vec{r})e^{j\omega t}\right] \tag{3.17}$$

Equation (3.16) can then be written as

$$\Delta\vec{\underline{E}}(\vec{r}) + \omega^2\mu\varepsilon\left(1 - j\frac{\sigma}{\varepsilon\omega}\right)\vec{\underline{E}}(\vec{r}) = \Delta\vec{\underline{E}}(\vec{r}) + \underline{k}^2\vec{\underline{E}}(\vec{r}) = 0 \tag{3.18}$$

The second term on the far left of equation (3.18) contains the complex dielectric constant and is given by;

$$\underline{\varepsilon} = \varepsilon - j\frac{\sigma}{\omega} \tag{3.19}$$

Next, we can write the complex wavenumber as

$$\underline{k} = \omega\mu\varepsilon\sqrt{1 - j\frac{\sigma/\omega}{\omega}} = \beta - j\alpha \tag{3.20}$$

The electric field can be represented in an orthogonal basis $(\hat{x}, \hat{y}, \hat{z})$ and defined so that $\hat{k} = \hat{z}$. The expression for the electric field then takes the form

$$\vec{\underline{E}}(z) = \vec{\underline{E}}_0 e^{-\alpha z} e^{-j\beta z} \tag{3.21}$$

In the time domain, this expression takes the form

$$\vec{E}(z,t) = \begin{bmatrix} E_{0x}cos(\omega t - kz + \delta_x) \\ E_{0y}cos(\omega t - kz + \delta_y) \\ 0 \end{bmatrix} \tag{3.22}$$

For a fixed time t_0 the electric field is composed of two orthogonal sinusoids. The polarization of the wave can be considered the shape the wave traces over a plane perpendicular to the dierection of propagation. For cases when $\delta = \delta_y - \delta_x = 0$ the wave is lineraly polarized and the electric field is a plane wave traversing a plane at an angle φ to the $\hat{x}$ axis. For cases when $\delta = \delta_y - \delta_x = \frac{\pi}{2} + k\pi$ and when E_{0x} and E_{0y} are equal the resulting wave rotates about the $\hat{z}$ axis and traces out a circle. In any other case, the resulting wave describes a helical trajectory about the $\hat{z}$ axis resulting in an elliptical shape.

3.5.2 Polarization diversity

SAR systems typically employ radiation of both linear *horizontal* (H) and *vertical* (V) polarization states. SAR systems are diverse in their polarization characteristics and can employ varıous combinations of H and V polarization states. Combinations of sent and received polarized energy include; HV, indicating radiation that had a horizontal polarization when being sent and a vertical polarization upon return, VH indicating radiation that had a vertical polarization when being sent and a horizontal polarization upon return and VV and HH indicating radiation that had both vertically and horizontally polarization states when being transmitted and vertically and horizontally polarization states upon being received respectively.

Types of SAR that employ the various polarimetric channels available include;

- Mono-polarization: these are the simplest types of imaging radar and can receive one the same (like) polarization that was sent. These polarization channels correspond to HH and VV
- Dual-polarization: these types of sensors are able to transmit on one polarization and receive simultaneously on two polarizations, one being the like polarization state and the other being the cross polarization state. These polarization channels correspond to HH/HV or VV/VH.

- QuadPolarization: these are sensors where the transmitted polarizations are multiplexed H and V and the received polarizations are simultaneous H and V. These polarization channels correspond to HH, VV, HV and VH.
- Compact-polarization: these types of sensors are capable of transmitting on only one polarization and are able to receive on two orthogonal polarizations while retaining their relative phase.

Note; the above information was taken from (Raney, 2011).

3.5.3 Representation of Multipolarization Data

The scattering process that is occurring at the target can be expressed with the following formula

$$\underline{E_S} = \frac{e^{-jkr}}{r}[S]\underline{E_J} = \frac{e^{-jkr}}{r}\begin{bmatrix} S_{HH} & S_{HV} \\ S_{VH} & S_{VV} \end{bmatrix}\underline{E_J} \tag{3.23}$$

here S is the scattering matrix (also known as the Sinclair matrix). This complex scattering matrix describes the transformation of the transmitted wave into the received wave. The elements of the scattering matrix are the complex scattering amplitudes $S_{IJ} = |S_{IJ}|exp(\iota\varphi_{IJ})$ where the subscripts I and J indicate the associated recieved and transmitted polarizations. The $\frac{e^{-jkr}}{r}$ factor indicates the phase shift and the attenuation for a spherical wave with a radius equal to the distance between the scatterer and the sensor. k is the wavenumber and is equal to $2\pi/\lambda$. The scattering matrix is determined by transmitting radiation in two orthogonal polarizations and receiving in two orthogonal polarizations where the transmitted and received polarization bases are commonly the same (Moreira, et al., 2013).

The scattering matrix describes the deterministic i.e. point like, scatterers that change the polarization of the wave but it does not describe the depolarization of the incident radiation for the case of distributed scatterers. Distributed scatterers are considered to be an ensemble of deterministic scatterers. The scattering matrix that is measured then consists of the coherent superposition of each individual scattering matrix from the scattering points that compose the resolution cell. In order to characterize fully the behaviour of the scattered radiation from the dispersed scatterers in each resolution cell a second-order statistical formalism is adopted (Moreira, et al., 2013).

The most common approach to portray the distributed scatterers is via the $3x3$ coherency matrix $[T]$ (or via the $3x3$ covariance matrix $[C]$) which is defined as the outer product of the three-dimensional Pauli scattering vector $\vec{k}_p$ (or lexicographic scattering vector $\vec{k}_L$). Scattering vectors are often employed for the analysis of polarimetric data as opposed to the S-matrix for ease of use. These scattering vectors are defined as

$$\vec{k}_p = \frac{1}{\sqrt{2}}[S_{HH} + S_{VV}, S_{HH} - S_{VV}, 2S_{XX}]^T \tag{3.24}$$

$$\vec{k}_L = \left[S_{HH}, \sqrt{2}S_{XX}, S_{VV}\right]^T \tag{3.25}$$

The S_{XX} arises from the case of receprocity. This occurs when the difference between the cross-polarization channels is small on average and thus the cross-pol terms can be replaced by the term $S_{XX} = \frac{1}{2}(S_{HV} + S_{VH})$. Data that has this format is called single-look complex (SLC) (Eltoft, et al., 2015).

Multilooking the Hermitian outer product of the $\vec{k}_p$ or $\vec{k}_L$ vectors results in the $[T]$ or $[C]$ matrices and are defined as

$$C = \langle \vec{k}_L \vec{k}_L{}^{\dagger} \rangle = \frac{1}{L} \sum_{i=1}^{L} \vec{k}_{L_i} \vec{k}_{L_i}{}^{\dagger} \text{ and } T = \langle \vec{k}_p \vec{k}_p{}^{\dagger} \rangle = \frac{1}{L} \sum_{i=1}^{L} \vec{k}_{p_i} \vec{k}_{p_i}{}^{\dagger} \tag{3.26}$$

Respectively where the subscript † refers to the conjugate transpose and L indicates the number of looks. Data presented in this format is called multi-looked complex (MLC).

3.6 Radarsat-2: Sensing Modes

Radarsat-2 is a commercial SAR that was launched in December 2007 by the Canadian space agency. This satellite is a C-band SAR with the capability to acquire data in HH, HV, VV and VH polarizations. The resolution of SAR can range from 1m in Spotlight mode to 100m in ScanSAR Wide Beam mode. A brief discussion on the different modes of acquisition is presented below.

3.6.1 ScanSAR

This imaging mode has a nominal resolution of 25m and a swath width of 300km for ScanSAR Narrow and a nominal resolution of 50m and a swath width of 500m for ScanSAR Wide. Data acquired in this mode is available in either Single or Dual polarization. The ScanSAR imaging modes acquire images of very wide swaths and are ideal for the use in applications that require large area coverage. The ScanSAR mode is suitable for the monitoring of offshore areas and has proven indispensable in the investigation of ice mapping, oil slick monitoring and ship detection.

3.6.2 Fine QuadPol

This imaging mode has a nominal resolution of 8m and a swath width of 25km.The data that is acquired in this mode is available in four combinations of polarization, HH, HV, VV and VH. While the spatial resolution of this sensing mode is quite high, its small swath width makes it impractical for large scale monitoring.

4 Optical Imaging

The following chapter is designed to illustrate the physics behind the operation of optical sensors. The chapter begins with a brief discussion on what a spectroradiometer is which is then followed by a description of the physical quantities it measures i.e. radiance and emissivity.

4.1 What is a Spectroradiometer?

MODIS stands for Moderate Resolution Imaging Spectroradiometer. Before a discussion on the underlying physical principals of optical imaging can be presented, the question of what an imaging spectroradiometer is, and what its capabilities are, must first be addressed.

According to (Ohno, 2007) a spectroradiometer is a device that measures the spectral quantities of light sources. Such quantities include the spectral irradiance, the spectral radiance, the spectral radiant intensity and the total spectral radiant flux. A spectroradiometer consists of a few distinct components each of which serves a different function. Fore optics on the instrument collect the incoming radiation and direct it to a monochromator, which then separates the radiation into its constituent wavelengths. Once the light is separated in this fashion, it is directed towards a detector where it is converted into an electrical signal.

4.2 Method of Imaging

MODIS is known as an across track scanner. This is the most common type of acquisition method used in optical satellite missions. In this type of configuration, the previously mentioned fore optics consists of a set of lenses and mirrors that oscillate perpendicularly to the satellite track (Chuvieco, et al., 2010). Figure 4.1 shows a diagram of this basic acquisition method. In this diagram, the scanning mirror assembly is marked with a letter A Each line is scanned from one side of the track to the other using this rotating mirror set-up. As the satellite moves forward, each successive scan generates a two-dimensional image of the Earth's surface. Internal detectors that are sensitive to specific ranges of the EM spectrum measure the incident energy in each band; this is marked with a B. The instantaneous field of view (IFOV), marked with a C, of the sensor and the altitude of the platform, determine the ground resolution of the cell being observed, marked with a D, and thus the spatial resolution. The angular range of the scanning mirror (110º for the case of MODIS) determines the size of the swath width, marked with an F.

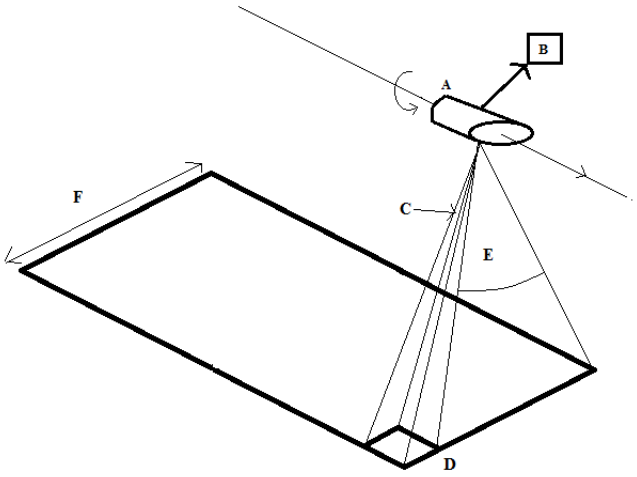

Figure 4.1: Basic set-up of an across track scanner. The scanning mirror (A) collects radiation which is then passed to internal devices (B). The IFOV (C) is and the sensor altitude determine the ground resolution (D). The angular range of the mirror assembly determines the swath width (F).

4.3 Radiance and Emissivity

As mentioned above, the fundamental physical quantities of measurement in optical sensors are radiance and emissivity. These two aspects are defined and described below.

4.3.1 Radiance

In order to describe what radiance is in a comprehensive sense a few quantities need to be first defined. The following definitions were sourced from (Elachi, et al., 2006) and (Hecht, 2002). We begin with the describing *Radiant Energy*. According to the authors just cited, *Radiant Energy,* is the energy that is carried by an EM wave. This quantity provides a measure of the wave's ability to do work by either heating an object of by changing its state. The rate in time, in which *Radiant Energy* passes a certain point, is referred to as the *Radiant Flux*. The *Radiance* is the *Radiant Flux* per unit solid angle that is leaving an extended source in a particular direction per unit area projected in that direction. This quantity has the units of watt/steradian m^2.

4.3.2 Emissivity

Objects that have a temperature above absolute zero ($0\ K\ or\ -273.15\ ^{\circ}C$) emitt EM radiation. How much energy that is emmited, and at which wavelengths most of the radiation is emitted, depends on the *emissivity* and the *kinetic temperature* of the surface (Prakash, 2000). The emissivity of a body refers to its ability to emit radiation when compared to a blackbody. All natural terrains have a lower efficiency in converting heat to radiation than blackbodies and the emissivity is expressed as

$$\varepsilon(\lambda) = \frac{S`(\lambda, T)}{S(\lambda, T)} \tag{4.1}$$

which is the radiant emittance of the terrain to the radiant emittance of a blackbody of the same temperature (Elachi, et al., 2006).

4.4 Spatial Resolution of Optical Sensors

The following brief discussion on the resolving power of optical sensors was taken form (Townshend, 1980) and (Chuvieco, et al., 2010) and is designed to give a brief overview of the topic of spatial resolution of optical sensors.

The spatial resolution refers to the minimum size of objects on the ground that can be separately distinguished or measured. According to (Townshend, 1980) there is no single adequate measure of spatial resolution, and the entire concept is more complex than this initial intuitive definition. The authors write that the definition of spatial resolution can be assigned to one of four categories;

- geometrical properties of the imaging system
- the ability to distinguish between point targets
- the ability to measure the periodicity of repetitive targets
- the ability to measure the spectral properties of small finite targets

The first two categories are the most relevant forms of spatial resolution and so will only be discussed here as a discussion of the other two are beyond the scope of this study. The reader is referred to (Townshend, 1980) for more information.

In the first category, the only measure that needs to be taken into consideration is the IFOV. This is generally regarded as the most intuitive measure of spatial resolution. This is also one of the most widely quoted resolution measures for optical satellite systems and is given below in equation 4.2.

$$IFOV = \frac{Hd}{f} \tag{4.2}$$

where H is the altitude of the satellite, d is the detector size and f is the focal length of the imaging system. In simple terms, the IFOV is defined as the area on the ground that is viewed by the instrument from a given altitude at any given time. Note however, the IFOV does not necessarily provide the smallest dimension of the objects that are able to be detected. An object that is smaller than the size of the IFOV may be able to be detected especially if it is sufficiently brighter or darker than its surroundings. Note also that the alignment of such objects will also play a role in their detectability.

In the second category, the most common definition for resolution is given by the Rayleigh criterion. This criterion is generally accepted as the criterion for the minimum amount of detail that is able to be resolved in an image. According to (Hecht, 2002) this is given by the minimum resolvable angular separation or the angular limit of resolution and given by;

$$\Delta\theta = \frac{1.22\lambda}{D} \tag{4.3}$$

where λ is the wavelength of the incoming radiation, and D is the diameter of the imaging system.

4.5 MODIS Satellites

As already stated, MODIS is an instrument on board NASA's Earth Observing System (ESO) Terra and Aqua satellites. MODIS is able to image in 36 spectral bands and has a total of 490 detectors located on four focal plane assemblies (FPA) (Xiong, et al., 2005)

Terra was placed into orbit in 1999 at 705km above sea level, in a near-polar, sun synchronous orbit. Aqua was launched in 2004 and was as well was placed into a near-polar sun-synchronous orbit at an altitude of 703 km above sea level. The two satellites offer complete global data coverage every 1-2 days at three primary spatial resolutions i.e. 250m, 500m and 1000m. Data from the sensor ranges from roughly $4\mu m$ to roughly $12\mu m$ in wavelength. This high radiometric resolution, combined with the highly precise geolocation of the image pixels (to within approximately 200m) make it an ideal source for investigating geophysical phenomenon (Wright, et al., 2002).

5 EM bird

The EM bird is an electromagnetic sounding device that is dedicated to the measurement of sea ice thickness. Sea ice thickness is a very important geophysical variable, and apart from upward looking sonar (ULS), electromagnetic induction thickness sounding is the only way to directly measure this variable (Haas, et al., 2007). EM birds can be operated from a variety of platforms including ships (Haas, 1998) (Haas, et al., 1999) or fixed manmade structures such as oil platforms or lighthouses (Haas, et al., 2003). However, the best way to measure the thickness of sea ice is via airplane (Multala, et al.) or by mounting the EM bird onto a helicopter (Kovacs, et al., 1987) (Kovacs, et al., 1990) (Haas, 2004) (Haas, et al., 2006). This is commonly referred to as helicopter-borne electromagnetic sounding (HEM).

This chapter is intended to give a brief introduction to the basic physical principals behind the operation of this device.

5.1 Physical principal behind HEM sounding

The EM sensor system is composed of a laser altimeter and a series of transmitter and receiver coils whose purpose is the transmission and reception of EM fields of low frequency. The EM components of the device are sensitive to the height above the seawater surface i.e. the interface between the ice layer and the underlying water. The laser altimeter simultaneously measures the height of the device above the ice and snow layer. The difference in the two height measurements corresponds to the total thickness of the ice layer (i.e. sea ice plus snow). The resulting thickness measurement has a nominal uncertainty of 0.1% for level sea ice with errors up to 50% over highly ridged areas (Johansson, et al., 2017). This is shown in the diagram in Figure 5.1 below. As can be seen the thickness of the ice snow layer, z, is found via the equation

$$z = h_w - h_i \tag{5.1}$$

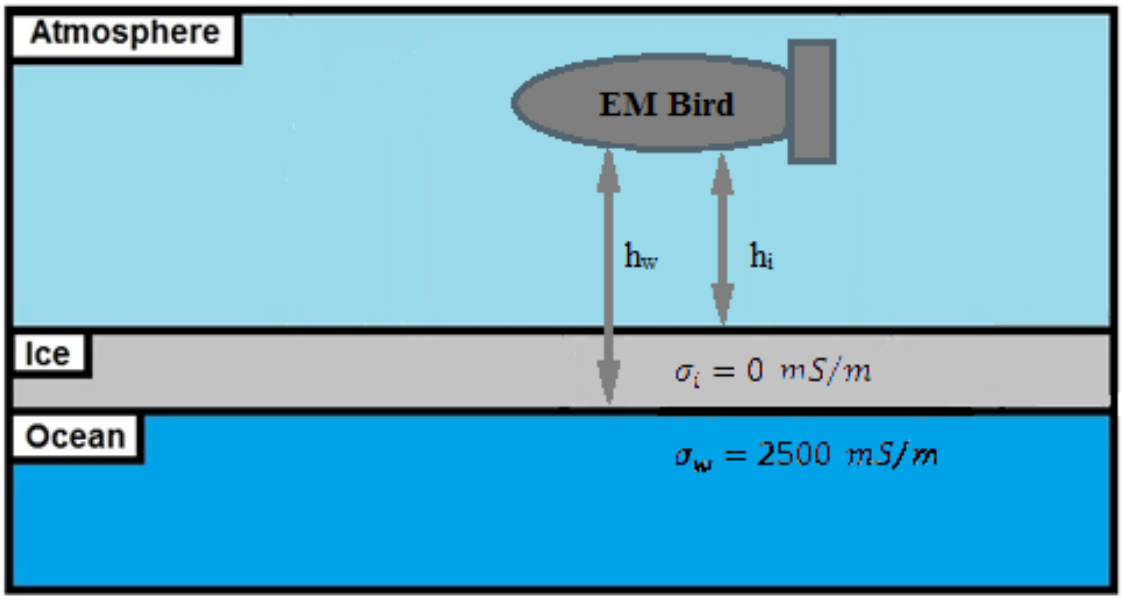

Figure 5.1: The transmitter and receiver coils provide a measurement on $\boldsymbol{h_w}$ the laser altimeter provides a measurement on $\boldsymbol{h_i}$. The ice thickness is found via equation 5.1. $\boldsymbol{h_w}$ is able to be determined due to the vast disparity between the conductivity of the water and the conductivity of the sea ice.

The laser altimeter works on the basis of bouncing light off the surface below and measuring the time it takes for the light to return to the device. The height above the ice snow layer is then calculated by simply multiplying the time it took for the light to make one round trip by the speed of light.

The height from the ice-water interface is calculated by having a transmitter coil produce a primary magnetic field H_P which induces eddy currents to flow in nearby conductors. In this system, the sea water is a conductor while the ice layer is not. This is shown in Figure 5.1 where the conductivity of the seawater is denoted as $2500\ mS/m$ while the conductivity of the ice is $0\ mS/m$. The eddy currents produce a secondary magnetic field H_S, which is detected by the receiver coil along with H_P. Through the use of bucking coils and system electronics, the effects of the primary field at the receiver coil is cancelled out. The measurement of H_S is then converted into a distance measurement to the conductor through various calculations (Kovacs, et al., 1987). This principal is further illustrated in Figure 5.2.

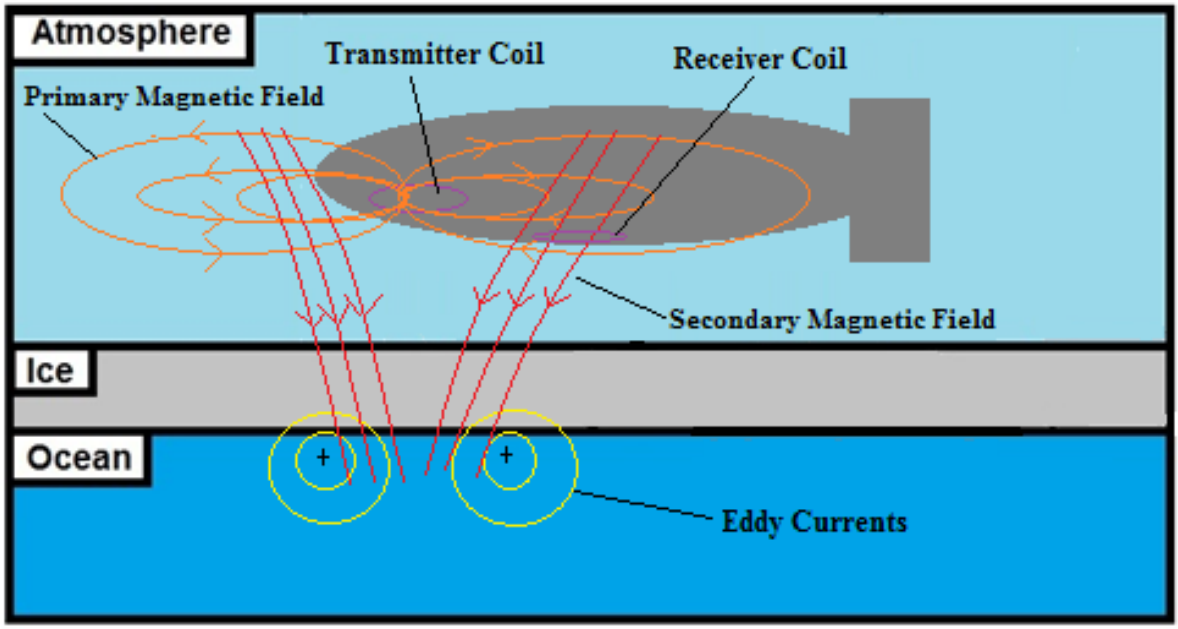

Figure 5.2: The principle by which $\boldsymbol{h_w}$ is determined is shown. The Transmitter coil produces a primary magnetic field H_P which induces eddy currents in nearby conductors (sea water in this case). These eddy currents produce their own magnetic fields H_S. The receiver coil acts to separate out the contribution of H_P to the magnetic field measured at the receiver coil via a series of system of electronics and bucking coils. The measured H_S is then converted to a the value $\boldsymbol{h_w}$.

5.2 HEM Data

The HEM data that is used in thesis was acquired on 11 May 2013 over the Eastern part of the Fjord. The observed ice thickness were taken mainly over the landfast ice that was present and some open water. The tracks that the helicopter took are shown below in Figure 5.3 and Figure 5.4. Figure 5.3 shows the HEM data in blue as well as the footprints of the three SAR data types that were taken i.e. the ScanSAR Narrow data, taken March 21, the ScanSAR Wide data taken May 12 and the QuadPol data taken May 10. Figure 5.4 shows a close-up of the area that the HEM flew over. As can be seen the area is highly congruent with the footprint of the QuadPol data. The HEM data was acquired in intervals of 3-5 meters.

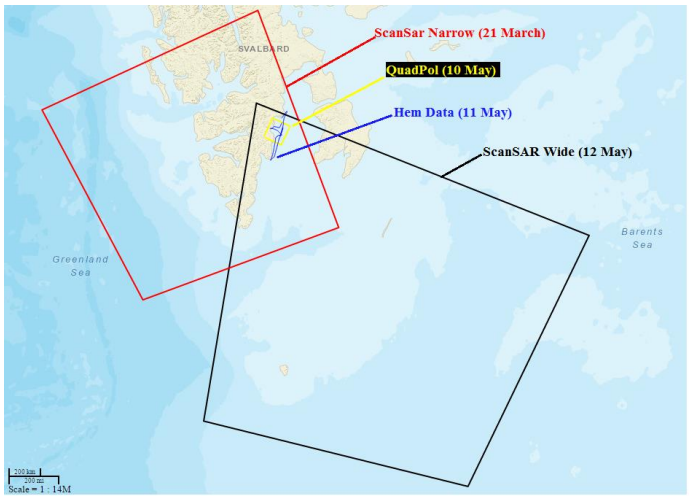

Figure 5.3: Location of HEM data as well as showing the footprint of the three SAR data sets that were used in this thesis.

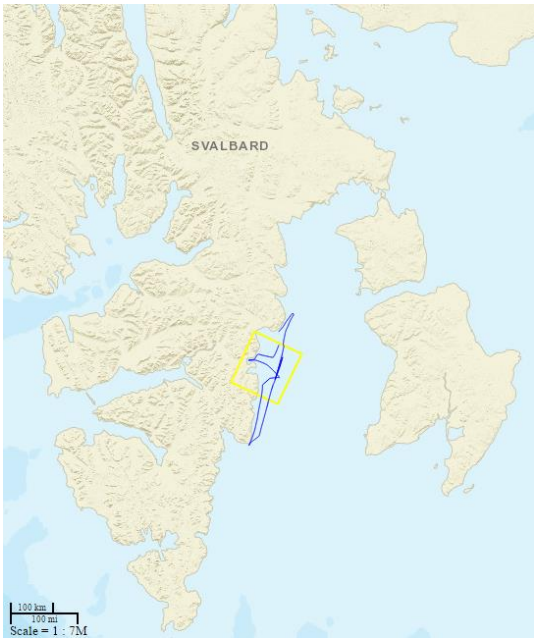

Figure 5.4: Close-up of the area where the HEM data was taken. This area is comprised mostly of landfast ice. The yellow square shows the footprint of the QuadPol data.

6 Literature Review: Methods of Segmentation for Sea Ice from Satellite Imagery

This review focuses on examining the various techniques that have been reported to date in relation to classifying or segmenting sea ice data collected by both optical and SAR sensors. The method in which this review was conducted was inspired by (Joshi, et al., 2016) who conducted a literature review comparing the use of optical data and radar data for land use mapping and monitoring. While the authors of this study compiled an in depth, comprehensive review of this field of research, the literature review presented here is only designed to serve a broad illustration of the major trends in the area of sea ice segmentation and classification.

6.1 Literature Review

In order to get a broad overview of the literature pertaining to these subjects, a set of structured queries were inputted into the Web of Science (http://apps.webofknowledge.com/) using a combination of key terms and their synonyms that were deemed most likely to be found on articles of interest. The search terms can be seen below in Table 6.1. The results were restricted to articles and reviews and led to a gross selection of 376 papers relating to the segmentation of sea ice in the SAR domain and 91 papers in the optical/thermal domain. Based on the abstracts of these papers, papers where key terms were present but that did not address segmentation of data were excluded. Papers that did not address segmentation of sea ice in particular, but that were orientated towards other aspects of the cryosphere were also excluded as well as papers that dealt with the investigation of sea ice from platforms that were not satellites i.e. ships or upward looking sonars etc. Those papers that dealt with areas of the Earth's surface not in the Arctic, for example the Baltic or Antarctica, were also excluded due to the differences in material and geographic properties that may affect the ice properties and growth. This resulted in a selection of 129 papers that dealt with segmentation of SAR data and 3 papers that dealt with segmentation of optical/thermal data.

The resulting set of studies, 132 in total, were analysed with respect to two target questions. These questions are as follows:

Q1) What methods have been performed/implemented in the past to segment or classify optical/thermal data with respect to the investigation of sea ice?

Q2) What methods have been performed/implemented in the past to segment or classify SAR data with respect to the investigation of sea ice?

As well as these two primary target questions, a number of sub questions were formulated to guide the review. These are:

SQ1) What sensors/sensor data have been used in the past for the investigation of sea ice?

SQ2) What were the principal applications for segmenting the sea ice data?

SQ3) How are the investigators distributed by country and over what time period were these investigations carried out?

Table 6.1: List of search terms entered into the web of knowledge and the gross and net number of papers that were found.

Search Terms	Gross Results	Net Results
(radar OR microwave* OR SAR*) AND (segment* OR classif* OR pattern recognition) AND (sea ice OR sea-ice) NOT (oil OR passive)	376	129
(thermal OR optical) AND (segment* OR classif* OR pattern recognition) AND (sea ice OR sea-ice) NOT oil	91	3

6.1.1 Results for Optical/Thermal Data

As already stated only three papers were found that dealt with segmentation of sea ice data in the optical/thermal domain. These three shortlisted studies were published between 1994 and 2016 by 3 first-authors based in the U.S. and Germany. One of the studies (Massom, et al., 1994) used AVHRR/2 data and two of the studies (Willmes, et al., 2015) and (Willmes, et al., 2016) used MODIS thermal infrared data.

Note. AVHRR is the Advanced Very High Resolution Radiometer and is considered the predecessor to MODIS. It has five spectral bands ranging between $0.63 - 12\mu m$.

(Massom, et al., 1994) attempted to only classify four broad surface categories in the Bering Sea. Those were namely open water, new ice (this included grease ice, dark nilas and pancake ice), young ice (which includes light nilas) and thick ice (which includes (first-year ice and landfast ice). The authors implemented a thresholding segmentation method that separated these ice types based on their spectral signatures in near infrared (NIR) and thermal infrared (TIR) regions of the EM spectrum. Spectral peaks in these bands were based on a priori empirical data. The authors concluded that the key to clear category discrimination lay in the use of the TIR AVHRR/2 bands as these bands allowed for the clear discrimination between regions where a marked thermal contrast exists but where the spectral albedos were similar.

(Willmes, et al., 2015) and (Willmes, et al., 2016) both performed segmentation on the ice surface temperature MODIS product (MOD/MYD29). (Willmes, et al., 2015) implemented a number of techniques to segment out leads from the surrounding ice. Their methods included implementing a set of non-parameterized global thresholding techniques such as iterative selection, Otsu's method, the minimum error threshold method and the maximum entropy thresholds method to create a binary image aimed at segmenting the image into two brightness classes within a given histogram of grey values. The authors approach works well for the segmentation of leads that are sufficiently wide but had difficulty identifying narrow leads or leads that had thin ice. (Willmes, et al., 2016) implemented a binary segmentation procedure to identify leads from MODIS TIR data on a daily time scale. They implement the same segmentation procedures as those implemented in (Willmes, et al., 2015) to generate pan-Arctic lead maps for the years 2003 to 2015 between the months of January to April.

6.1.2 Results for SAR Data

Given that 129 results were found that dealt with the segmentation of SAR data, it was decided to choose only a subset of these papers and demonstrate their methods. Because of this, the 10 papers that had the most citations were chosen. The reasoning behind this approach being that papers that are heavily cited will be most representative of this field of research. The results are shown below in Table 6.2.

Table 6.2: Ten papers with the highest number of citations that dealt with the segmentation of SAR imagery for sea ice in the Arctic.

Study	Country	Times Cited	Sensor
(Deng, et al., 2005)	U.S.	96	Radarsat-1
(Clausi, et al., 2004)	Canada	84	Radarsat-1
(Clausi, 2001)	Canada	81	Radarsat-1
(Soh, et al., 2004)	U.S.	40	Radarsat-1
(Haverkamp, et al., 1995)	U.S.	39	ERS-1
(Bogdanov, et al., 2005)	Russia, Germany, Norway	38	ERS-1,Radarsat-1
(Ochilov, et al., 2012)	Canada	34	Radarsat-1
(Geldsetzer, et al., 2009)	Canada	33	ENVISAT
(Maillard, et al., 2005)	Canada	30	Radarsat-1
(Zakhvatkina, et al., 2013)	Russia, Norway	30	ENVISAT

The 10 studies cited above in Table 6.2 were published between 1995 and 2013 by 9 first authors based mainly the U.S. and Canada. One of the studies was a collaboration between researchers based in Russia, Germany and Norway while another was a collaboration between researchers based in Russia and Norway. Seven of the studies based their findings on data collected from Radarsad-1, two of the studies based their findings on data from ERS-1 (European Remote Sensing) and two of the studies based their findings on data taken from ENVISAT (Environmental Satellite).

Out of the ten studies cited above the most popular classification method was unsupervised segmentation via Markov Random Field (MRF). (Deng, et al., 2005), (Clausi, 2001), (Clausi, et al., 2004), (Ochilov, et al., 2012) and (Maillard, et al., 2005) implemented this method.

According to (Deng, et al., 2005) one of the most common segmentation methods is the one proposed by (Haverkamp, et al., 1995). (Haverkamp, et al., 1995) proposed the methods of segmentation known as dynamic thresholding. In this method, thresholding values are chosen from small local regions, which are then used to threshold the entire image. This method accounts for the local variance in the scene. (Soh, et al., 2004) also implemented this method as well as two other segmentation methods i.e. unsupervised clustering and watershed merging. Their research was orientated towards designing an automated, intelligent and operational system for sea ice image analysis. They called their system Advanced Reasoning using Knowledge for Typing Of Sea ice (ARKTOS). The work of (Bogdanov, et al., 2005) and (Zakhvatkina, et al., 2013) was based on implementing a neural network for sea ice segmentation and (Geldsetzer, et al., 2009) were able to discriminate various sea ice types based on a decision tree classifier and statistical thresholds.

6.1.3 Conclusion

This review was based on looking for scientific papers that dealt with the segmentation of data from optical sources and SAR sources individually. Thus, papers that dealt with the segmentation of data that was fused from these two sensors, such as (Liu, et al., 2014), was excluded. As can be seen from Table 6.1 there seems to exist a disparity between the amount of research being conducted within these two domains. In others words, research into the segmentation of SAR for sea ice in the arctic seems to be more active than segmentation of optical data for sea ice in the arctic. One reason for this disparity may

be due to the fundamental nature of these two sensors. Optical sensors such as MODIS are passive and so rely on solar radiation that is reflected from the Earth. The obvious drawback to this is that optical sensors are then susceptible to cloud cover and the polar night. The benefits in using SAR is that it is an active sensor which means it is its own source of illumination and operates at wavelengths that render the effects of could cover negligible. Given the benefits of using SAR as opposed to optical sensors for arctic monitoring it is reasonable to assume that there is a greater interest in SARs over optical sensors for these purposes.

It is interesting to note that the very few papers that were found, for the segmentation of optical data, were all skewed towards the TIR range of the EM spectrum. TIR is emissive and is very useful in determining the thickness of sea ice up to 80cm thick (Yu, et al., 1996). The use of the TIR bands however is a highly active area of research in the endeavour to determine the thickness of thin sea ice. This is covered in detail in section 2.3.2.1. It is hypothesized that if terms relating to thickness determination were included into the search terms in Table 6.1, then the net number of results relating to segmentation in the optical domain would be higher.

7 Methods

This chapter is intended to illustrate the more practical aspects involved in this thesis and is intended to serve as a departure from the previous chapters, which were more theoretical in nature. First, a description of the study area is presented, which is based on a priori knowledge available from scientific literature and freely available ice charts from the Norwegian met office. First examining what conditions were like at the time the data was collected can help in interpreting results at a later stage. Next all data sets that were used in this study are described in detail, as well as the pre-processing steps that were applied to them. A discussion on the polarimetric features that were extracted from the SAR data are discussed as well as a brief introduction to the theoretical basis for the segmentation algorithm that was used, i.e. Mixture of Gaussian segmentation with Markov random smoothing. This chapter concludes by describing the method in which the comparison was carried out.

7.1 Study Site

Storfjorden constitutes a large, north-south orientated, 300-km-long, expanse of water located between the islands of Spitsbergen, Barentsøyga and Edgøya in the Southeastern part of the Svalbard archipelago in the Arctic Ocean. This area is located between 76° 40`N - 78° 40`N and 16° 40`E - 23° E. Two shallow straits, Heleysundet and Freemansundet, connect Storfjorden with the Barrents Sea in the Northeast part of the bay. Figure 7.1 shows Storfjorden enclosed within a red polygon.

Figure 7.1: The Svalbard Archipelago showing the Storfjorden area enclosed within a red polygon. Image taken from worldview.earthdata.nasa.gov.

Storfjorden is home to a large latent heat polynya that is the result of persistently strong northerly to northeasterly winds. These off shore winds serve to export ice out of the fjord resulting in enhanced ice production due to the exposure of the water surface to the atmosphere. The cooling of water at the surface and the ice growth that follows, increases the level of salt present in the water and results in brine rejection. This brine-enriched surface water sinks to the sea floor and flows to deeper parts of the fjord where it is eventually makes its way into the Fram Strait at the southern end of the bay (Haarpainter, et al., 2001).

A twelve year study between the years of 2002/2003 – 2013/2014 was conducted by (Preußer, et al., 2015) for Storfjorden between the months of November to March. Thin ice thickness values were calculated using MODIS IST data combined with ECMWF ERA-Interim atmospheric reanalysis data in a thermodynamic ice growth model proposed by (Yu, et al., 1996). From this, the authors were able to calculate associated quantities such as polynya area and total ice production over this twelve year period. They found that within the course of an average winter season, ice with thicknesses below 10 cm were most prevalent within the Storfjorden basin and tended to be concentrated in the Eastern part of the fjord. The mean polynya area was found to be 4555.7 ± 1542.9 km^2. Ice production rates were observed to be 26 cm d^{-1} at their maximum, and the average ice production rate observed over an entire winter was observed to be 28.3±8.5 km^3. The authors of this study suggest that despite the relatively short period of 12 winter seasons that were used for this study, a positive trend of about 20.2 km^3 of ice production per decade was detected. This is in contrast to a negative trend in ice production observed prior to 2002, according to the authors.

Figure 7.2 shows the relative frequency distribution of TIT (i.e. ice with thicknesses ≤ 0.2 m) within Storfjorden between January and March for each year between 2003 and 2014 as reported by (Preußer, et al., 2015). As can be seen, thin ice is generally found in the eastern part of the Fjord while thicker ice was generally found in the western part of the Fjord.

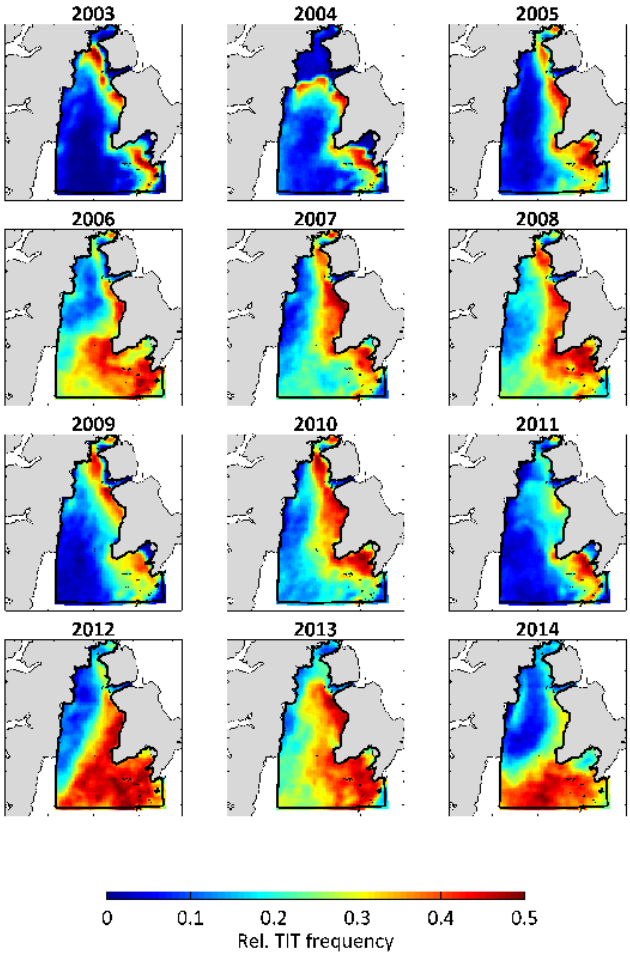

Figure 7.2: Relative frequency distribution of ice with thicknesses ≤ 0.2 m within Storfjorden between between January and March for each year between 2003 and 2014. Image taken from **(Preußer, et al., 2015)**.

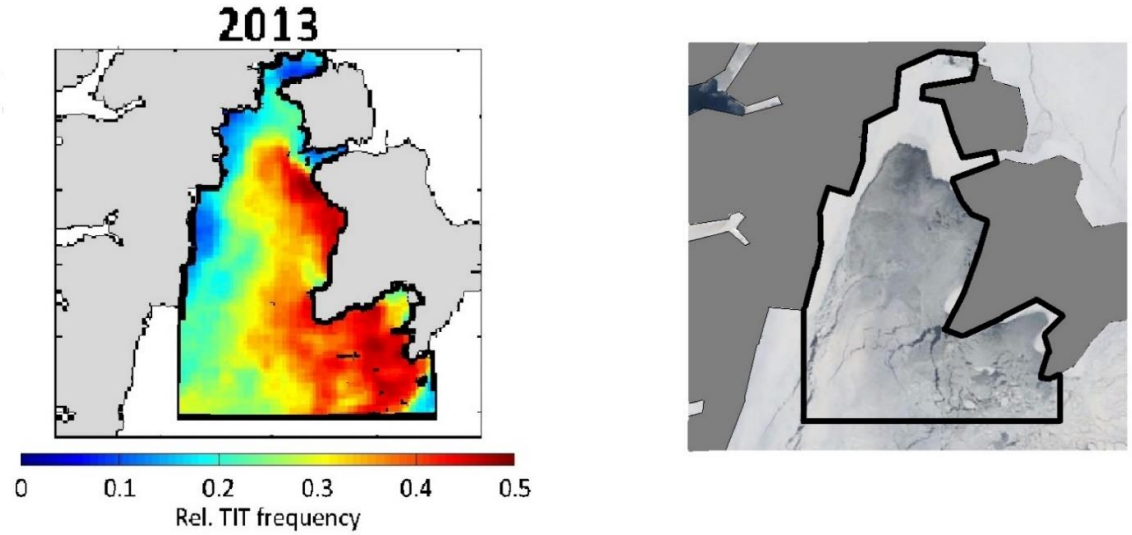

Figure 7.3: (Left) panel in Figure 7.2 corresponding to the winter season of 2013 **(Preußer, et al., 2015)**, (Right) a MODIS true colour image corresponding to the same area displayed in (Left), Image taken from worldview.earthdata.nasa.gov. The corresponding regions of ice with varying thickness in (Left) can be distinguished in (Right).

Figure 7.3 shows the panel in Figure 7.2 corresponding to the year 2013 (Figure 7.3 (Left)) alongside a truecolor MODIS image for Storfjorden taken on March 21 2013 (Figure 7.3 (Right)). (Note: data from the 21 March is used in this study and will be explained in more detail in the next section). The land has been masked out and the polygon that is present in Figure 7.3 (Left) has been applied to the Figure 7.3 (Right). Upon visual inspection, it is easy to see that areas of low thin ice occurrence, marked in blue in Figure 7.3 (Left), correspond to areas where landfast ice is present in Figure 7.3 (Right). This can be seen in the Northern and Western parts of the bay. The areas in Figure 7.3 (Left) where the thinnest ice is present, marked in red to green, can be seen also in Figure 7.3 (Right) where the darker grey tones indicate areas of thin ice.

In addition to this information, it is also possible to determine whether the ice present in the fjord is MYI or FYI. As already explained in chapter 3, FYI is ice that appears within a single growing season whereas MYI is ice that has survived at least one melting season. The two types differ greatly in characteristics such as salinity, thickness and roughness (Carsey, 1992).

The ice that is present in Storfjorden during the time of investigation is all FYI. This is easily demonstrated in Figure 7.4, which shows a MODIS truecolor image of Storfjorden, acquired by the Terra satellite, on 15 August 2012 i.e. the late summer before the dates this study is concerned with. This image shows Storfjorden ice-free. This indicates that any ice, that is observed during the periods of March and May, appeared within the fjord over the previous 5 to 6 months to data acquisition.

Figure 7.4: MODIS Terra truecolor image of Storfjorden captured on August 15 2012. As can be seen there is no ice present in the fjord at this time indicating that any ice present in the 2013 images is FYI. Image taken from worldview.earthdata.nasa.gov

7.1.1 Ice Charts and atmospheric data

Two periods of time were chosen in this study for the purposes of comparison. The first being the 21 March 2013. This date was chosen as data from both MODIS and RS2 (dual-pol ScanSAR Narrow) were available that overlapped exactly in time at a period of low cloud cover.

The second period of time chosen, were the consecutive days of 10th/11th/12th of May 2013. The reason for choosing this period, was that thickness measurements from a HEM campaign were available on 11 May, a QuadPol SAR measurement was available on 10 May and RS2 (dual-pol ScanSAR Wide) and MODIS measurements were available at a cloud free period on 12 May. These two measurements were made roughly an hour apart. The MODIS data was acquired at 04:15 in the morning, the RS2 at 05:20.

In order to gain a deeper understanding of the ice conditions in Storfjorden for those dates, ice concentration charts were downloaded from the Norwegian Meteorological Institute (polarview.met.no). These charts are based on the manual interpretation of data from RS2 (dual-pol ScanSAR Wide data). These charts were available for the dates of 21 March, 10 May and 13 May and are discussed below. Also shown in the following subsections are atmospheric data from the two weather stations closest to Storfjorden, those being the weather stations at the Longyearbyen airport and the island of Hopen. Storfjorden lies roughly half way between these two points and data from these sites can provide an overview about the weather conditions in the fjord leading up to, and including the time of data acquisition. The locations of these stations, relative to Storfjorden can be seen in Figure 7.5, marked with black squares. Storfjorden is marked with a black polygon.

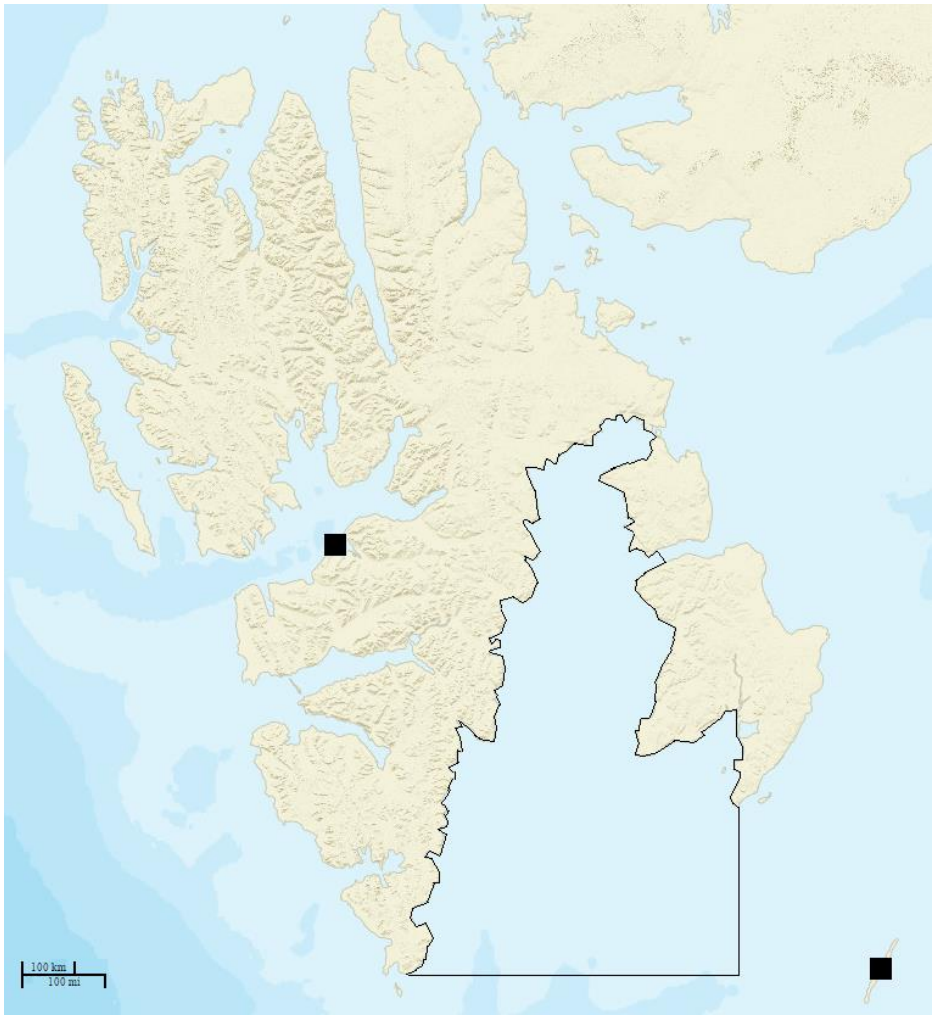

Figure 7.5: Positions of the weather stations on Hopen island (bottom right) and Longyearbyen airport (mid-left) marked with black squares. The Storfjorden area is marked with a black polygon. Image taken from Google Earth.

7.1.1.1 21 March

Shown below in Figure 7.6 is the ice concentration chart for 21 March 2013. As can be seen this corresponds somewhat to the images in Figure 7.3. Thicker landfast ice can be found to the Northern and Western parts of the fjord. Areas within the Fjord designated with the colours red, orange and yellow were found to be drift ice, i.e. ice that moves due to effects from the wind or underlying currents. The concentration of the drift ice is in close resemblance to the results found in (Preußer, et al., 2015) and from Figure 7.3 (Left). We can see that there is a higher concentration (90%) of drift ice in the western part of the fjord, followed by ice of lesser concentrations in progression to the Eastern parts of the fjords. These concentrations range from 70-80% for areas marked in Orange to 40-70% for areas marked in yellow. As can be seen, there are no large areas of open water within the fjord, which is in direct agreement with the true colour image shown in Figure 7.3 (Right).

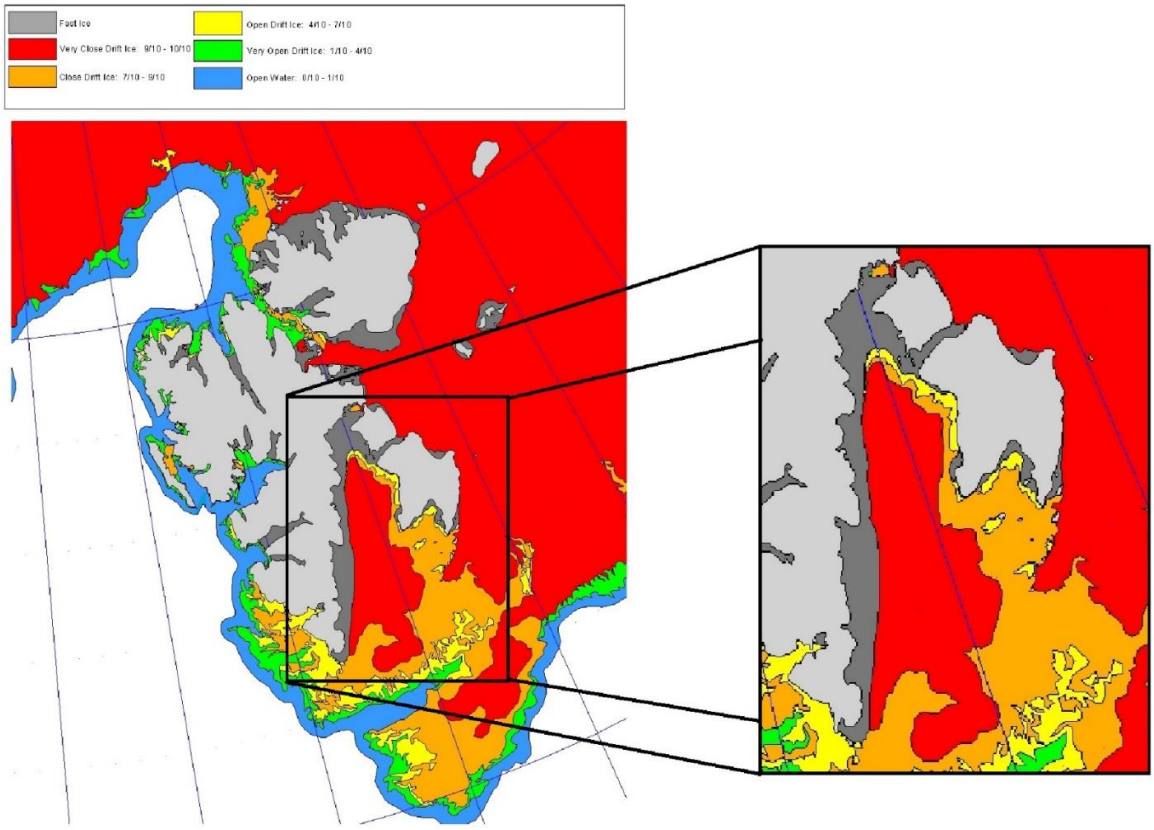

Figure 7.6: Ice concentration chart for 21March 2013 taken from the met office website polarview.met.no. Areas of land fast ice can be seen in this is chart which can also be seen in Figure 7.3. No major areas of open water is present in this chart which is in direct correspondence with Figure 7.3 (Right).

Shown below in Figure 7.7 are the air temperatures and relative humilities for March 21 and the 7 days leading up to it. Measurements are taken at hourly intervals. The time of acquisition from both MODIS and Radarsat-2 is denoted by the vertical dashed line. Looking at the air temperatures over the course of the entire 8 days, it can be seen that the temperatures measured from these two locations seems to be roughly correlated despite the fact that the weather stations that took the measurements, are about 300km apart. Especially interesting is the fact that at the time of data acquisition the temperature measurements are very similar and nearly coincide. Over the course of this 8-day period the minimum and maximum

air temperature, measured from Hopen Island, was -19.1 ºC and -4.4 ºC respectively while those measured from Longyearbyen airport were -16.7 ºC and -4.9 ºC respectively. The maximum temperature difference between the two data sets over the course of this 8-day period was 4 ºC. The temperature measured at the two stations for the time that the satellite data was acquired is -10.5 ºC and -11.8 ºC from Hopen Island and Longyearbyen respectively.

The measurements for the relative humidity are more divergent with data from Hopen Island yielding larger values for humidity across most of the 8-day period. The maximum difference in humidity between measurements made from these two sites was 40% across this period. Like the measurements for air temperature, the measurements for humidity made at the time the satellite data were taken are nearly the same. Hopen Island is 74% while that at Longyearbyen airport is 77% for this time.

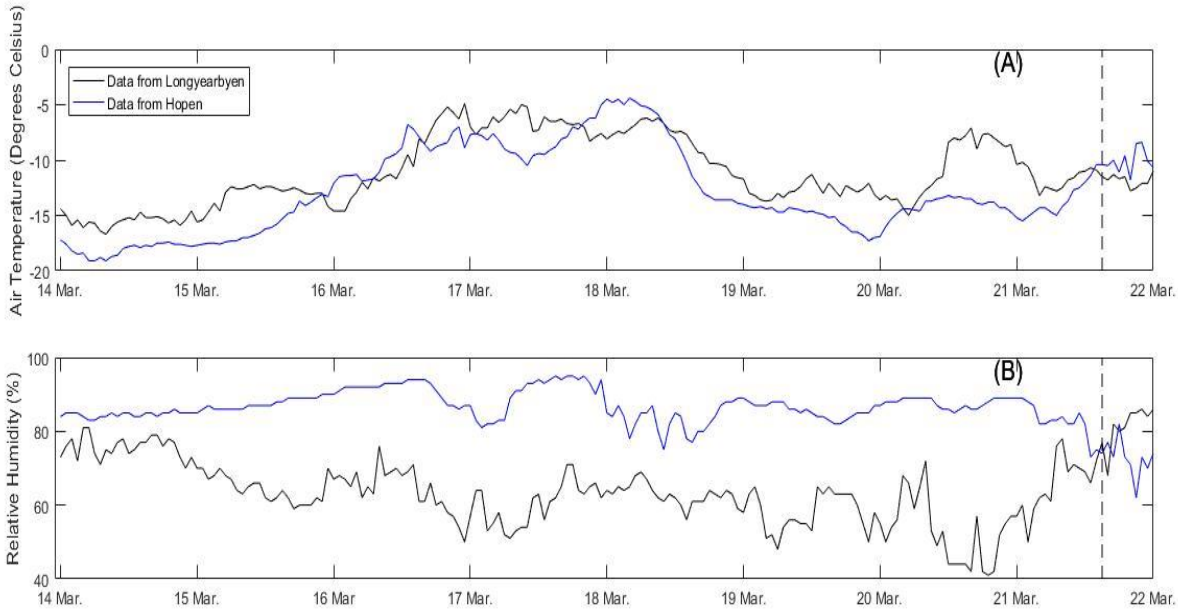

Figure 7.7: (Top) Air temperature as measured on Hopen island and at Longyearbyen airport. (Bottom) Relative humidity measured at the same locations as in (Top). Both sets of measurements are for 21st March 2013.

Figure 7.8 shows a graph for wind velocities measured over the same period along with the relative wind directions that are associated with these measurements. Firstly, it is easy to see that the measurements for wind velocity are very similar to each other but the associated wind directions are in opposition. Measurements made at the Svalbard airport favour a north westerly direction while measurements made from Hopen Island favour a south westerly direction. It is speculated that the reason for this discrepancy is due to the fact that the Longyearbyen airport is situated at the end of a north west – south easterly valley that may be prone to localized wind tunnelling effects. Hopen Island is situated in the open ocean and so is probably more indicative of the large scale wind behaviour in the region. The minimum value for the wind velocity measured from Hopen Island, for this period, was 0.6 m/s while the maximum was 11.2 m/s. The minimum for wind speed measured from the Longyearbyen airport was 0 m/s while the maximum was 13.7 m/s.

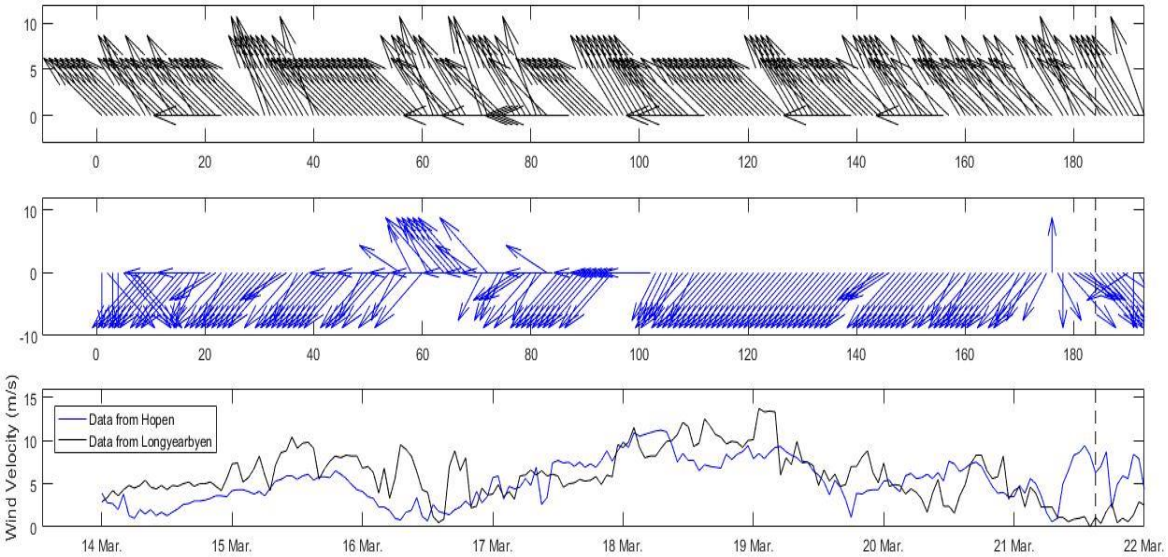

Figure 7.8: (Top) Wind directions as measured at Longyearbyen airport, (Middle) Wind directions as measured on Hopen Island, (Bottom) wind velocity as measured at both locations.

7.1.1.1 10th/11th/12th/13th May

Figure 7.9 (Top, left) and (Bottom, left) show ice charts for the dates of 10th and 13th of May 2013 (Note: charts from these dates were chosen as there was no ice chart available for 12 May 2013). Alongside these ice charts, in Figure 7.9 (Right), the true colour MODIS satellite image of Storfjorden on 12 May 2013 is also shown. In this image, a land mask that roughly corresponds to the land mask seen in the ice charts is applied. Note; due to the cloud cover observed in the right part of the image, the land mask diverges slightly to the one seen in Figure in the ice charts. Since this figure as just for illustration, these differences are not critical.

Like the chart displayed in Figure 7.6 land fast ice is still visible in the Northern and Westerly part of the bay and can be clearly seen in Figure 7.6. Due to the onset of the melting season, open water is now visible in both charts. It is interesting to note that the nature of the ice concentration changes from Figure 7.9 (Top, left) to Figure 7.9 (Bottom, left). In Figure 7.9 (Top, left) large swaths of drift ice that were designated in red, as very close drift ice, are then designated as close, open and very open (orange, yellow, green) drift ice in Figure 7.9 (Bottom, left). This serves to illustrate that Storfjorden is a highly dynamic fjord and that ice conditions can change in a short period, two days in this case. The MODIS image in Figure 7.9 (Right) closely resembles the chart in Figure 7.9 (Bottom, left). While the presence of the land fast ice in both charts closely resembles that in the true colour image, the different gradations of drift ice, illustrated in Figure 7.9 (Bottom, left) can be seen visually in Figure 7.9 (Right).

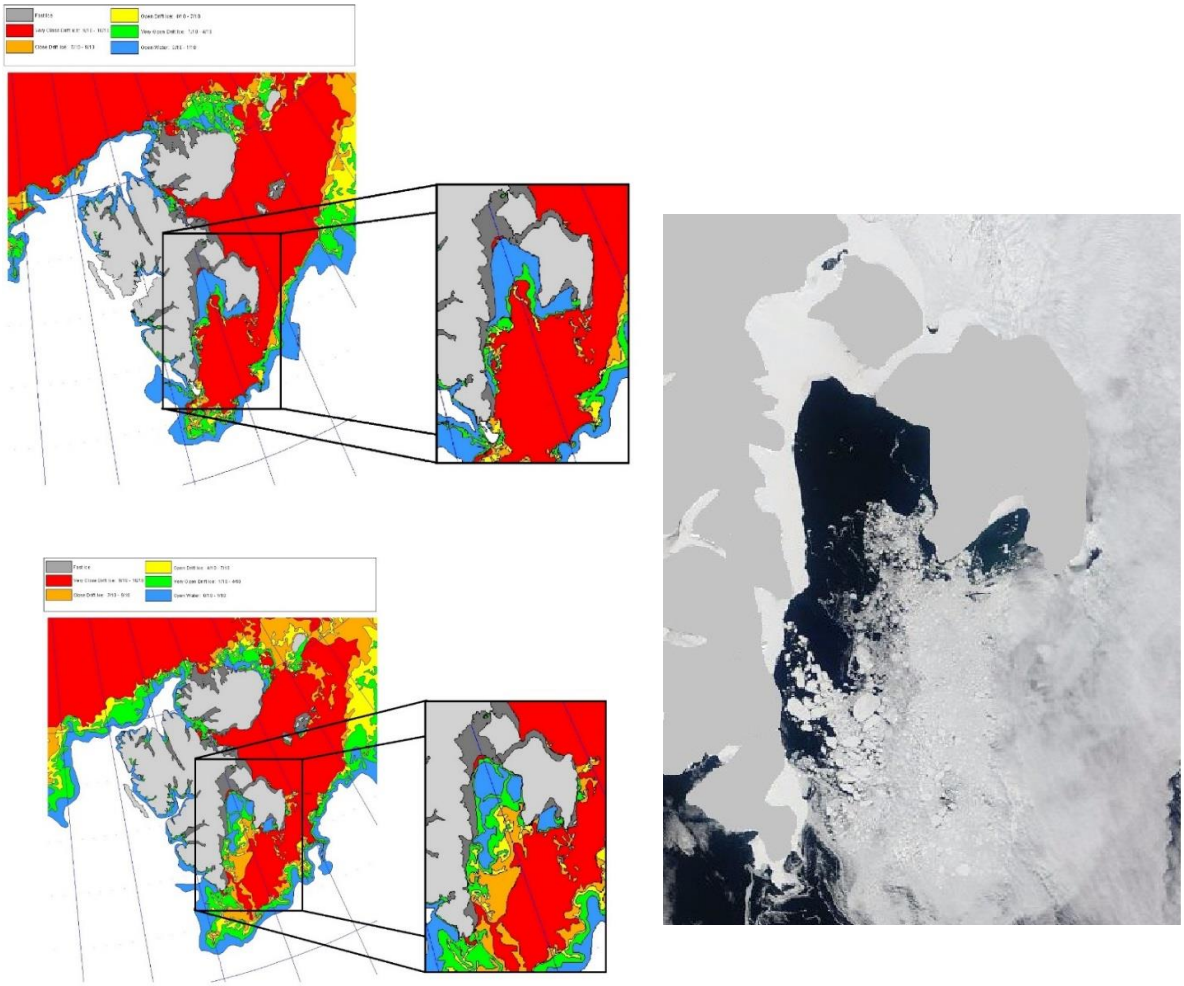

Figure 7.9: (Top, left) Ice concentration chart for the 10 May 2013, (Bottom, right) Ice concentration chart for the 10 May 2013, both top left and bottom left are taken from the met office website polarview.met.no (Right) True colour MODIS satellite image of Storfjorden, on 12 May 2013. Image taken from worldview.earthdata.nasa.gov

Figure 7.10 shows the data for air temperature taken between the 5 May 2013 and 14 of May 2013. The four vertical lines indicate the time of data acquisition from a particular sensor. In the same manner employed in the previous section, the graph shows data for air temperature in the top panel and humidity in the bottom panel, again both taken from the weather stations on Hopen Island and the Longyearbyen airport. Looking at the graph, we can see that the temperature measured at these two locations appears to be highly correlated. The horizontal dashed line in Figure 7.10 (Top) indicates a temperature of 0ºC. It can be seen that between the 10 and 11 of May, temperatures greater than 0ºC were recorded. The presence of temperatures greater than 0ºC indicates that there may have been some melting of the sea ice occurring. This may explain the differences in drift ice composition seen in the ice charts made for the 10 and 12 of May in Figure 7.9.

In contrast to Figure 7.7 (Bottom), the values for humidities shown in Figure 7.10 (Bottom) seem to be correlated, especially in the final half of the observation period. Again, like Figure 7.7 (Bottom) values for humidity taken from Hopen Island are higher than those taken at Longyearbyen airport. This can be explained by the fact that Hopen is situated in the open ocean whereas Longyearbyen is nestled in an inlet on the island of Spitzbergen.

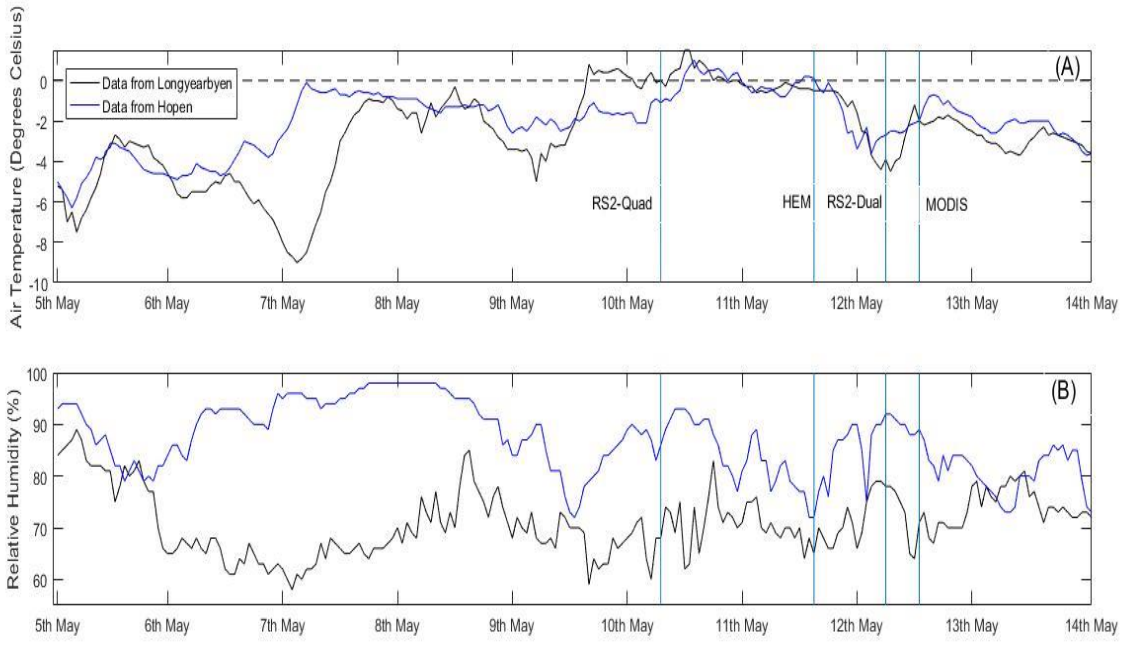

Figure 7.10: (Top) Air temperature as measured on Hopen island and at Longyearbyen airport. (Bottom) Relative humidity measured at the same locations as in (Top). Both sets of measurements are for 12 May 2013.

Figure 7.11 below shows the wind speed data for the same period as in Figure 7.10. Similar to Figure 7.8 the wind data from Longyearbyen seems to be biased towards blowing in a north west direction whereas the wind observed at Hopen island seems to be biased towards blowing in a direction south westerly direction. This can be seen in the first half of the observation period when the wind was at its strongest. At the time of satellite observations, the wind from both observation points behaves erratically, favouring primarily a northeasterly direction between the dates 10th and 11th of May (when the QuadPol measurement was made) and favouring no particular direction from the middle of 11 May onwards when the wind speed was at its lowest.

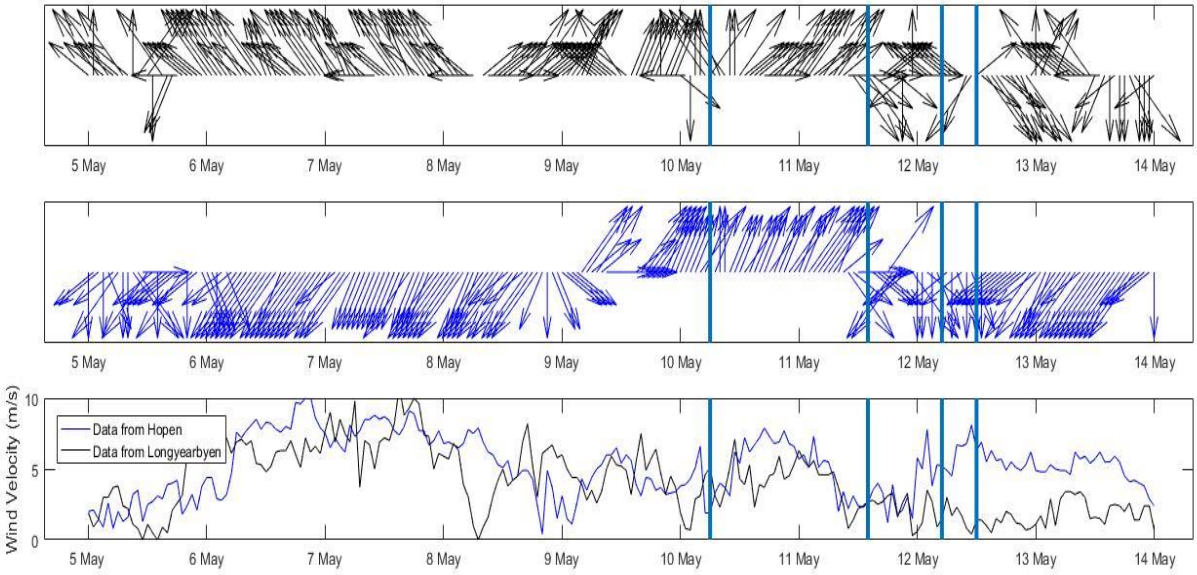

Figure 7.11: (Top) Wind directions as measured at Longyearbyen airport, (Middle) Wind directions as measured on Hopen Island, (Bottom) wind velocity as measured at both locations. Vertical blue lines indicate the time when a particular measurement was made and have the same meaning as those in Figure 7.10 .Both sets of measurements are for 12 May 2013.

7.2 Data sets

7.2.1 MODIS Data

MODIS operates on board both the Terra and Aqua satellites. Data is acquired by MODIS in 36 spectral bands that span the electromagnetic spectrum from 0.405 to 14.385 μm at resolutions of 250m, 500m, and 1,000m. Figure 7.12 shows the distribution of MODISs spectral response functions for the 36 bands throughout the EM spectrum.

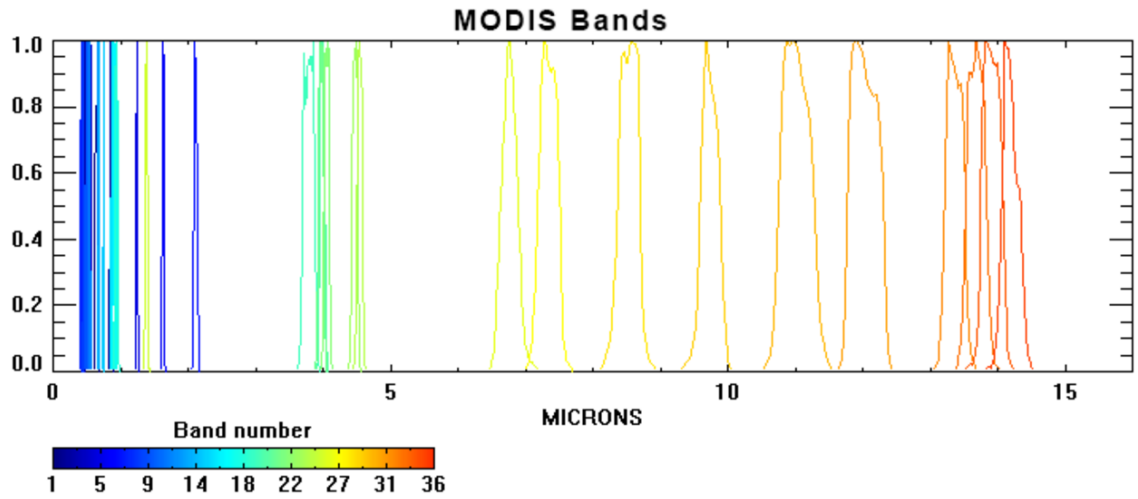

Figure 7.12: The distribution of MODIS's 36 bands spanning the EM spectrum from 0.405 to 14.385 μm. Image taken from http://gsp.humboldt.edu/olm_2015/Courses/GSP_216_Online/lesson3-1/resolution.html.

In this thesis, data from the following MODIS Terra and Aqua products are used;

- Calibrated Radiances 5-Min L1B Swath 250m (MYD02QKM/MOD02QKM)
- Calibrated Radiances 5-Min L1B Swath 500m (MYD02HKM/MOD02HKM)
- Calibrated Radiances 5-Min L1B Swath 1km (MYD021KM/MOD021KM)

The MYD02QKM/MOD02QKM products contain geolocated and calibrated radiances for MODIS bands 1 and 2 at 250m resolution, the MYD02HKM/MOD02HKM products contain geolocated and calibrated radiances for MODIS bands 1 through 7 at 500m resolution and the MYD021KM/MOD021KM products contain geolocated and calibrated radiances for all 36 MODIS at 1KM resolution.

Each scene has a nominal swath size of 2330km across track and 2030 km along track. This constitutes roughly 5 minutes of flight time (Hall, et al., 2004). These data products are freely available from the US National Aeronautics and Space Administration's (NASA) Earth Observing System Data and Information System (EOSDIS).

Cloud cover, is a persistent problem when working with optical data. Because of this, a MODIS cloud mask product (MOD/MYD35) is applied to the data to exclude cloudy regions. The MODIS cloud mask is a level 2 product that indicates a level of confidence whether a given field of view (FOV) is cloud free or not and has spatial resolutions of 250 and 1000m (Ackerman, et al., 1998). In order to derive the cloud mask, radiances from up to 14 spectral bands are used (Frey, et al.). The data from the visible channels are not applicable at night for cloud mask generation. Because of this, the quality of the cloud mask during the day is higher than that at night.

In summary, all MODIS products that are used in this study are stated below in Table 7.1.

Table 7.1: MODIS products that are used in this study

MODIS Product	Description
MYD02QKM/MOD02QKM	250m res. reflective bands
MYD02HKM/MOD02HKM	500m res. reflective bands
MYD021KM/MOD021KM	1000m res. reflective and emissive bands
MOD/MYD35 (taken from MOD/MYD29)	1000m res. cloud mask

7.2.2 Radarsat-2 Data

As previously stated, the bands commonly used in microwave remote sensing range from 0.75 to 100 cm. Given that the band with the longest wavelength in MODIS is band 36, with a maximum wavelength of 14.385 μm, Radarsat-2 data occupies a region of the EM spectrum populated by radiation of lower frequency and lower energy. Table 7.2 shows these bands in ascending order on the EM spectrum.

Table 7.2: Bands frequently used in Microwave Remote Sensing. Table taken from **(Chuvieco, et al., 2010)**. N/A= values not given.

Name	Width (cm)	Central Value (cm)
Ka	0.75-1.10	N/A
K	1.10-1.67	1.0
Ku	1.67-2.40	N/A
X	2.40-3.75	3.0
C	3.75-7.50	5.6
S	7.50-15.00	10.0
L	15.00-30.00	23.0
P	30.00-100.00	70.0

As previously mentioned, RS2 is a C band SAR. Thus, it operates in the region of 3.75 to 7.50 cm. Since it is an active sensor, it can produce electromagnetic waves with electric field components of various orientations relative to the direction of propagation. As already stated, RS2 has four possible transmit-receive polarization combinations; HH, VV, HV and VH. These combinations are referred to as polarimetric channels. Two different RS2 data sets are used in this thesis. The first is a Dual-pol data set, which contains the channels HH and HV. Dual-pol data was obtained and used for both 21 March and 12 May. The second data set used is a QuadPol data set that was acquired on 10 May 2013. This data set contains all four polarimetric channels.

NOTE: Radarsat-2 data products are provided by the MDA corporation.

7.2.3 HEM data

The HEM data that was used in this thesis was provided by Gunnar Spreen at the Norwegian Polar Institute, Tromsø, Norway

7.3 Data Pre-processing

Data pre-processing refers to the acts of manipulation applied to data sets before the primary goal of an investigation is performed. In this way, pre-processing can be considered as a way of "getting the data ready" before the primary objective of a study is applied e.g. classification or fusion etc. As this study is concerned with the comparison of data from two different sensors, MODIS and RS2, having images that are aligned and overlap, pixel for pixel, is of great importance. The pre-processing steps that are performed in this study are done so to meet this end. Figure 7.13 shows a schematic of the individual steps that were applied to the data sets. All pre-processing was performed using MATLAB and ENVI.

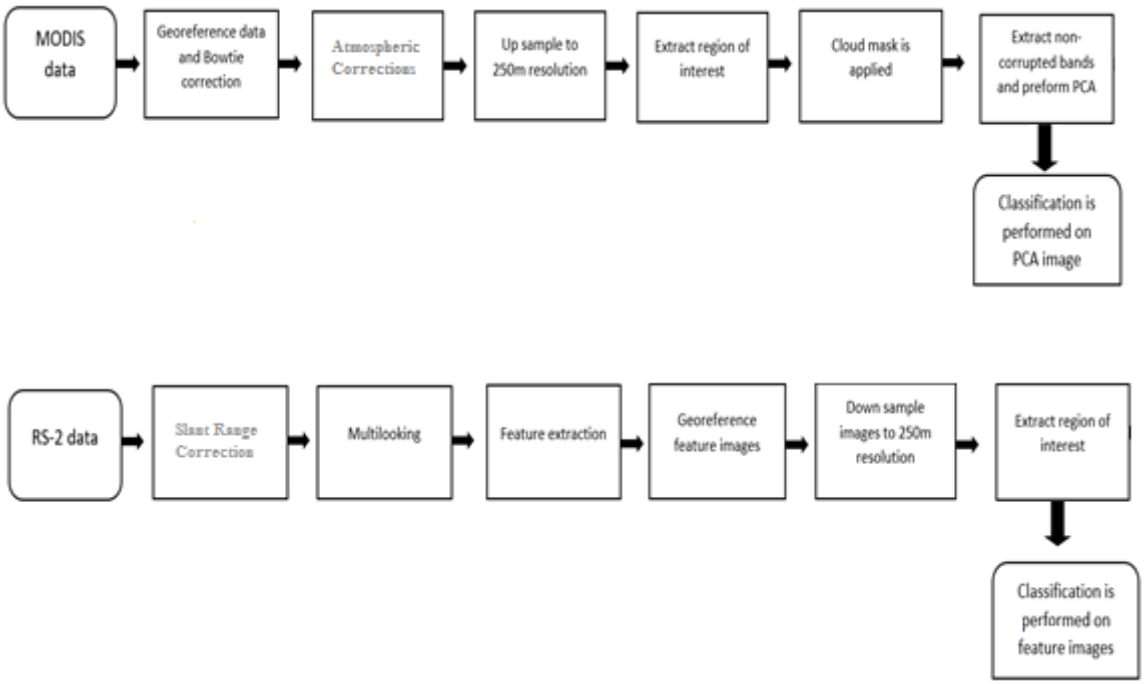

Figure 7.13: Schematic diagram showing all pre-processing steps applied to the data from both sensors.

In the sections below, each one of these steps is described. As can be seen from Figure 7.13 some steps are common to both sensors while some steps are exclusive to a particular sensor. In the sub-title for the description of each step, the indicators of *MOD* or *RS2* are used to imply if a particular step has been applied to data from either MODIS or RS2, or both, respectively.

7.3.1 A Short Note about datums and projections.

The following subsections serve to provide a brief introduction into the theory of geodetic datums and map projections. When working with satellite data, particularly for the purposes of comparison or data fusion, it is important to use cartographic systems that are consistent across all images.

7.3.1.1 Datums

In order to measure the coordinates of positions on the surface of the Earth, it is required to have a corresponding set of points or surfaces, which provide a reference. The shape of the Earth surface can be approximated by an irregular surface called the geoid. The irregularities and undulations in this shape are a product of the inhomogeneous distribution of mass within the crust of the Earth. These irregularities are small on the scale of the Earths size, and as a consequence, results in the geoid resembling an oblate spheroid of rotation, with the appearance of bulging at the equator and flattening towards the poles. Figure 7.14 shows the geometric figure of an oblate spheroid generated by rotating an ellipse about its minor (North-South) axis.

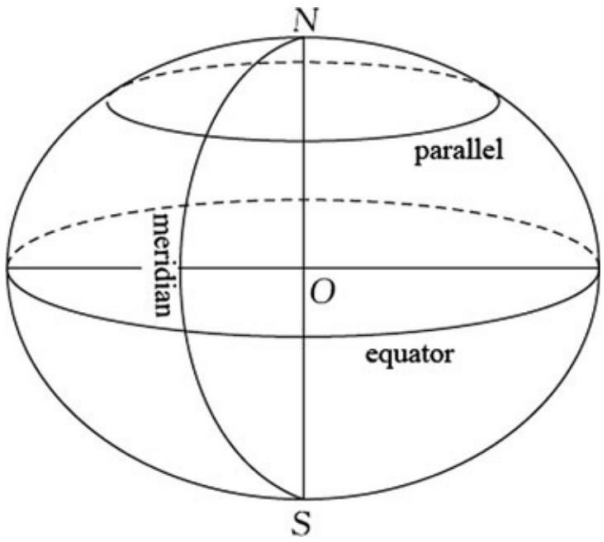

Figure 7.14: Oblate spheroid obtained by rotating an ellipse about the minor axis. Image taken from **(Lu, et al., 2014)**

In the field of geodesy, the shape that is used to approximate the geoid is referred to as the Earth ellipsoid. This ellipsoid is specified by four primary parameters, a the semi major axis, f the flattening parameter, M the mass of the ellipsoid and the angular velocity ω. a and f represent the geometric properties of the Earth, M indicates the physical properties of the ellipsoid and ω indicates its speed of rotation. These model ellipsoids are referred to as geodetic datums (Lu, et al., 2014).

The World Geodetic System (WGS84) is the standard datum used today in Global Positioning Systems (GPS) and is the datum specified in all RS-2 and MODIS (Nishihama, et al., 1997) products. Throughout the pre-processing stage, all data is processed in reference to this datum.

7.3.1.2 Projections

Datums are used to model the surface of the Earth, as it exists in 3-dimensional space. However, maps and images are flat, so the coordinates that define these have to be in plane coordinates. Projection is the process of establishing one-to-one relationships between geodetic coordinates, provided by the datum, and the plane coordinates of a map. Put another way, a map projection is methodical

representation of the Earth's surface on a flat plane. Over small areas, the surface of the earth can be approximated by a flat plane but over larger areas, distortions become apparent in the representation of the earth surface. Since introducing distortions is inescapable, the choice of projection is dictated by the characteristics that the user wishes to show accurately at the expense of others (Snyder, 1987).

There are three main types of main distortions, those being of area, distance and angle. It is possible to have a projection with a particular distortion reduced to zero, such as when we choose to work with an equiangular projection or equivalent (equal-area) projections, for example. Distortions like these can also coexist with one another but within a certain degree. Any projection will introduce distortions due to the undevelopable nature of the reference ellipsoid.

The projection that was chosen in this study was UTM. The UTM projection is a conformal projection in that it preserves angles. It was developed by the U.S. army in 1947 for the purpose of developing large-scale global military maps. In this system, the earth is divided into 60 zones between the latitudes of 84ºN and 80ºS where each zone is 6º wide in longitude. The 60 zones are labelled from 1 to 60 in ascending order beginning from the 180th meridian. There are further letter designations running from south to north as shown below in Figure 7.15. The grid square covering the Svalbard archipelago is marked in red in this figure and has a grid number of UTM 33 X. Each geographic location in the UTM projection system is given in terms of *x* and *y* coordinates that are in meters. If the ellipsoid and the hemisphere, i.e. North or South, are known, then only the zone number and the *x* and *y* coordinates are required to define a point (Snyder, 1987). Throughout the pre-processing stage of this study, all data was brought to the UTM 33N projection.

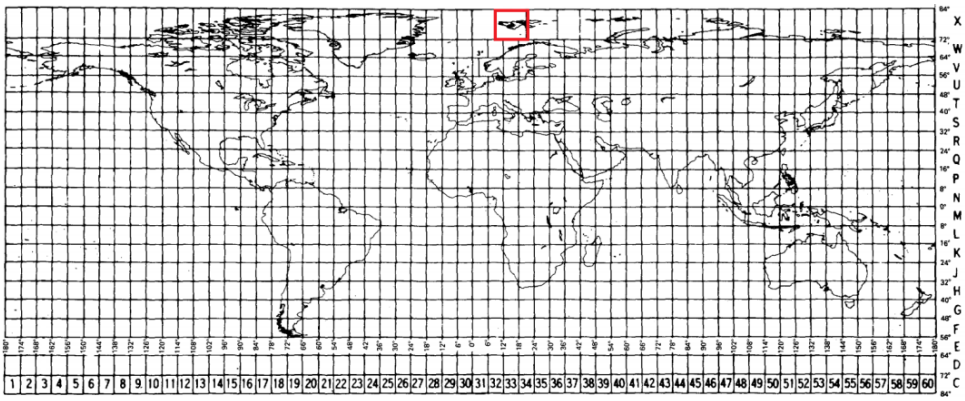

Figure 7.15: Image showing the layout of the UTM grid system. The Svalbard archipelago is marked with a red square designated by the box 33 X.

7.3.1.3 Georeferencing (MOD, RS2)

In a general sense, georeferencing can be considered the means of aligning one or more images with a different data source, like a map for example (Le Moigne, et al., 2011). When we perform georeferencing we are assigning geographic coordinates to each of the pixels in an image. In this study, the emphasis was on comparing images from two different data sources. For this end, the data from MODIS and RS2 were georeferenced to the UTM 33N projection outlined in the previous section. All georeferencing was conducted using ENVIs built in functions. The MODIS conversion toolkit (MCTK), a plug-in for ENVI, was utilized for the ingestion and georeferencing of the MODIS products used.

7.3.2 Bowtie correction (MOD)

The bow tie effect is a problem that is inherent to optical imaging systems that employ a scan mirror assembly. In MODIS, the Instantaneous Field of View (IFOV) of the rotating mirror remains constant throughout the scan cycle. As a result, more ground is imaged at the extremities of a scan than at the nadir. The extremities being located at -55º and +55º off nadir. This is a panoramic distortion that is exacerbated by the Earths curvature (Souri, et al., 2013). The Bowtie effect becomes apparent at 15º off nadir. Figure 7.16 shows a diagram of three scan lines, ranging from 0º at centre to 55º at the extremities, with overlapping due to the bowtie effect. The degree of this overlap ranges from 10% at scan angles of 24º and increases to almost 50% at the edges of the scan (Souri, et al., 2013). ENVI employs a re-projection method that offsets the bowtie effect in level 1B and level 2 MODIS data products.

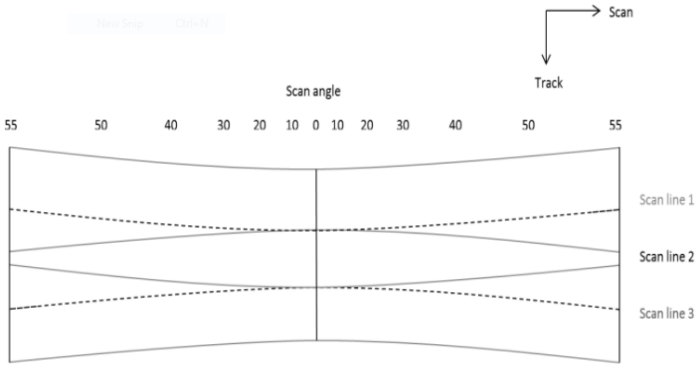

Figure 7.16: Diagram showing the bowtie effect. The edges of the scan lines are wider than that in the centre. Image taken from **(Souri, et al., 2013)**.

Figure 7.17 shows the bowtie effect as seen in the portion of the MODIS data that corresponds to Storfjorden. This is a red band image taken on 21 March 2013. As can be seen in the image, Storfjorden lies close to the edge of the scene so is prone to this distortion. This can be seen clearly by looking at the doubling effect of the open lead located in the Westerly part of the fjord. After the correction is performed, this effect disappears.

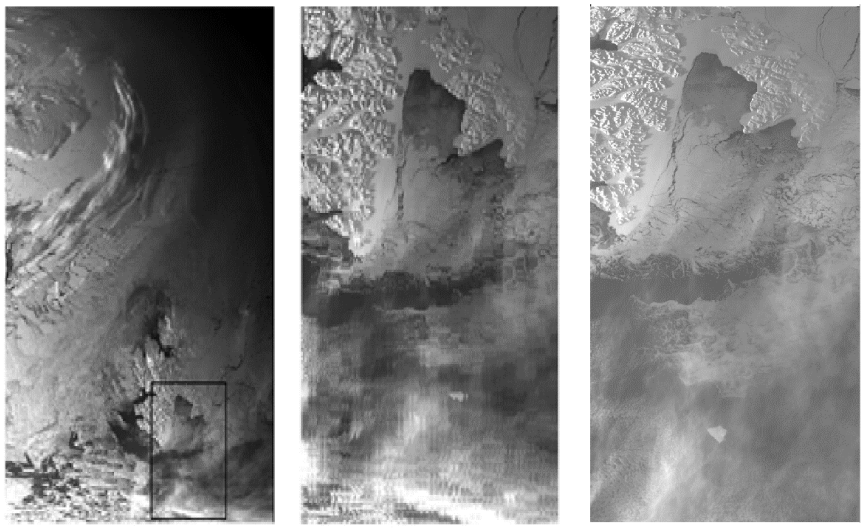

Figure 7.17: (left) Red, 250m resolution band from MODIS taken on 21 March. (Middle) Portion of (Left) that corresponds to Storfjorden. The bowtie effect can be clearly seen, especially in the doubling effect of the leads in the fjord. (Right) After the bowtie correction has been performed, bowtie effect disappears.

7.3.3 Atmospheric Correction (MOD)

A fundamental problem that occurs when dealing with data from optical sensors is that the radiation that impinges upon the sensor is modified by atmospheric constituents. The interaction of EM radiation with a planetary atmosphere is determined by the characteristics of the propagating wave (mainly wavelength) and the characteristics of that atmosphere i.e. pressure, temperature and amount and type of suspended particulates (Elachi, et al., 2006). The reason the Earth's atmosphere is highly interactive with radiation in this region of the EM spectrum, i.e. radiation in the optical/infrared region, is because its atmosphere is composed mostly of carbon dioxide, nitrogen, water vapour and ozone. The size of these atmospheric constituents are on the same scale as the wavelengths in this region. This is not the case for radiation from SAR sensors, as wavelengths in this region are in the order of centimetres to tens of centimetres. This means the atmosphere is mostly transparent to radiation form SARs.

ENVI hosts a number of methods that can be implemented when performing atmospheric correction. A summary of these methods is presented in table 7.3 below as they are stated on the Harris Geospatial website (Note: Harris Geospatial is the organization that develops ENVI).

Table 7.3: List of methods for performing atmospheric correction as stated on the Harris Geospatial website

Correction Name	Description
QUick Atmospheric Correction (QUAC)	This is an automated correction method that retrieves the spectral reflectance from multispectral images.
IAR (Internal Average Relative Reflectance) Reflectance	This method is used to normalize images to a scene average spectrum. This method is good for reducing hyperspectral data to relative reflectance in places where there is no knowledge of the ground conditions. This method works best for areas that are very arid and have little vegetation. In this method, an average spectrum is calculated from the entire image, which is divided into the spectrum of every pixel in the scene in question.
Log Residuals	This correction technique is constructed to eliminate the following from satellite scenes; instrument gain, solar irradiance, topographic effects, atmospheric transmittance, and albedo effects from radiance data by creating a pseudo reflectance image that is effective in analysing absorption features that are related to minerals.
Dark Subtraction	Subtracts a pixel value that represents the darkest point in any image band e.g. an area where shadow exists. The basic idea is that dark areas reflect no light and so any measurements made here must be the result of atmospheric scattering. This 'atmospheric value' is then subtracted from the rest of the image.
Flat Field	This method involves selecting a region of interest over a spectrally flat area from the data. The average spectrum of this region of interest is then used as a reference spectrum, which is then divided into the spectrum of each pixel in the image.
Empirical Line	This method uses at least one field, laboratory or other such reference spectrum in order to force the spectral data from the viewing sensor to match it. This method is equivalent to removing the solar irradiance and the atmospheric path radiance from the data.
Thermal Atmospheric Correction	This correction technique removes the contributions from the atmosphere for the thermal infrared domains i.e. for data between 8 and 14 μm. This correction method assumes that the atmosphere is uniform over the entire scene and that a blackbody like surface is present within the scene. Using this and after performing some regression analysis the atmospheric upwelling and transmission are derived and offset from the original data.

Given that there are numerous approaches that can be taken when performing atmospheric correction the question now arises; which one is the most appropriate for the case at hand? A Brief discussion on why some of the methods, mentioned in Table 7.3 above, are inappropriate for the task at hand is presented below.

- According to the Harris Geospatial website, QUAC is best suited for scenes that contain a number of diverse materials. They indicate that diverse materials implies the presence of things such as soil, water, artificial structures and vegetation. They also state that this method of correction is inappropriate over oceans or large bodies of water. Given that the area of Storfjorden is relatively homogenous in that it contains mostly only ice and water this method was not considered.
- The IAR method was cited as being appropriate for areas that are very arid and with no vegetation. While the polar regions are technically termed deserts due to the lack of precipitation that occurs they can also be quite humid as evidenced by the graphs in Figures 7.7 and 7.10. For this reason this method was also discounted.
- Flat field: This method requires selecting an area in the image that is of known 'flat reflectance' according to the website. This is taken to mean; an area in the image is to be selected that has homogenous reflectance values. Since this is a priori information that is not available and it was wished not to make assumptions about the scene this method was discounted.
- Empirical line: This method requires a priori information that was not available, thus it was discounted as viable.
- Thermal Atmospheric Correction: This method is only suitable for data that is between 8 and 14 μm. This means, this method is only applicable to 6 of the 36 MODIS bands, those being 29-34. While this does correct for most of the thermal infrared bands it does not correct all of them e.g. bands 35 and 36. For this reason, this method was discounted.

There were two considerations for the case of atmospheric correction; dark subtraction and Log Residuals.

Dark subtraction is a simple and effective technique to be used on multispectral data (not hyperspectral data) for the purposes of haze removal. This method was applied to MODIS reflective bands. The method of dark subtraction does not work well for emissive bands and so the method of log residuals was applied here.

7.3.4 Upsampling to 250m (MOD)

As already stated in section 7.2.1, three sets of MODIS data were used in this study. The resolutions of these data sets were 250m, 500m and 1000m. While the 250 meter resolution data contains more spatial detail, it but does not have a great deal of spectral resolution, there are only 2 bands in the 250m data sets. The 500m data contains less spatial detail than the 250m data, but has higher spectral resolution as it contains 7 bands at 500 meter resolution. The 1000m data has the lowest spatial resolution but contains the largest spectral resolution as it contains all 36 bands. Figure 7.18 illustrates this point clearly showing the specific bands that are available at each resolution.

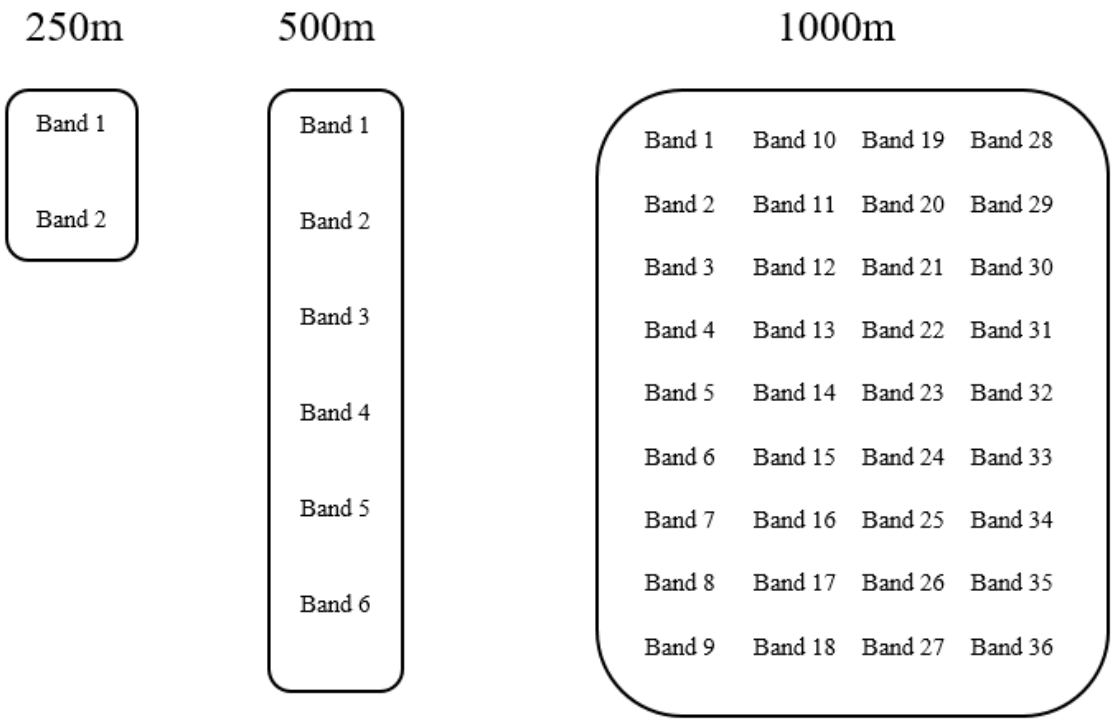

Figure 7.18: Diagram showing the availability of bands at each resolution.

In order to take advantage of the full spectral capabilities of MODIS, every band needs to be brought to a common resolution. The term resolution here refers to the pixel spacing of the data. In order to achieve this, the process of upsampling is employed where all bands were upsampled to a resolution of 250m, if they were not already at that resolution. The desired outcome of this processing step is to have a 36 band data set that takes full advantage of the spatial and spectral capabilities of MODIS. A schematic of the outputted data set is shown below in figure 7.19. This "new" data set contains the bands with the best spatial resolution, all at 250m resolution.

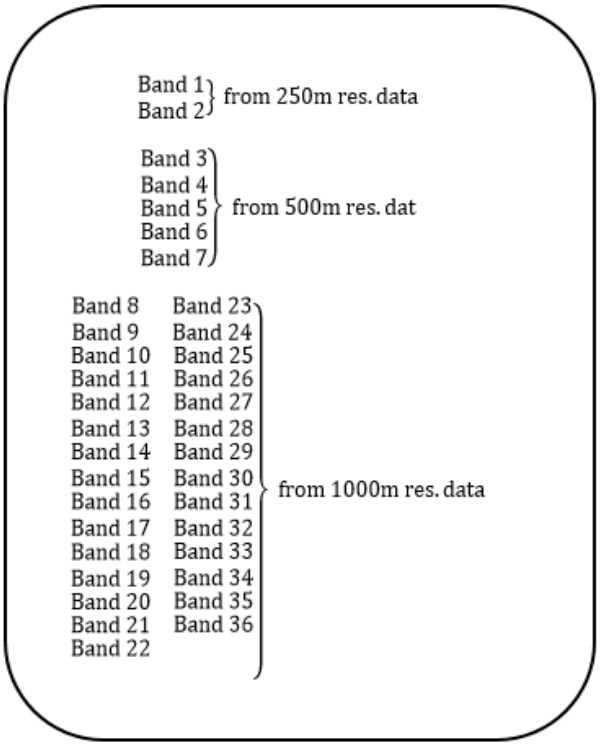

Figure 7.19: Diagram showing the makeup of the 36-band data set after upsampling is performed.

Upsampling is performed on the georeferenced, 500m and 1000m resolution data sets. In these data sets, each pixel can be considered as having sides of length 500m and 1000m on the ground respectively. The effect of upsampling is that each pixel of side length 500m and 1000m in the original data set, is split into sets of 4 and 16 pixels, where each pixel now has a side length of 250m. This is shown below in Figure 7.20.

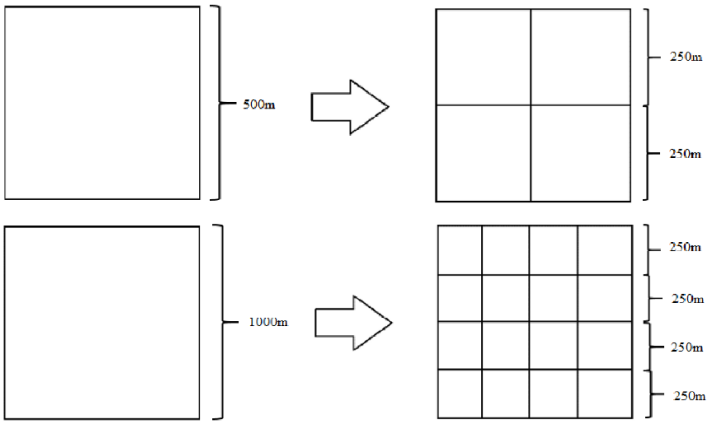

Figure 7.20: pixels in the original 500m and 1000m data sets before and after upsampling was performed.

ENVI offers three methods to perform upsampling, Nearest Neighbour, Bilinear and Cubic Convolution. The method that was chosen to arrive at the results illustrated in Figure 7.20 was nearest neighbour interpolation. This is the simplest and least computationally intensive option to perform upsampling and does not introduce intermediate averaged values between adjacent pixels.

7.3.5 Extracting regions of interest (MOD, RS2)

When working with satellite imagery, single observations can span many hundreds of kilometres. In the case of MODIS level 1B products, each scene typically has dimensions of 1354 x 2030 km (NASA, 2009). The RS2 dual-pol ScanSAR Wide data sets have dimensions of 500 x 500km (Zakhvatkina, et al., 2017). Thus, isolating a region of interest that will form the basis for a study is of great importance.

The process that was taken is this; first, the coordinates of the corners of the SAR image were found. These four coordinates were used to extract a rectangular roi from the original MODIS data. This is shown below in Figure 7.21 for the 21 March data.

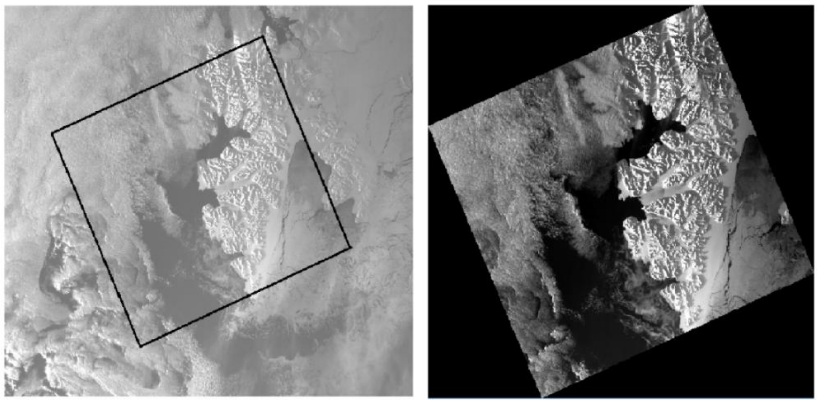

Figure 7.21: (Left) original MODIS data (red band is shown in image) with the region of interest that corresponds to the footprint of the ScanSAR Narrow image. (Right) the roi that was extracted from (Left).

Figure 7.22 shows the region of interest that was extracted from the image in Figure 7.121(b). This region was extracted in order to mask out the land and to exclude any region where there are shadowing effects from the surrounding mountains.

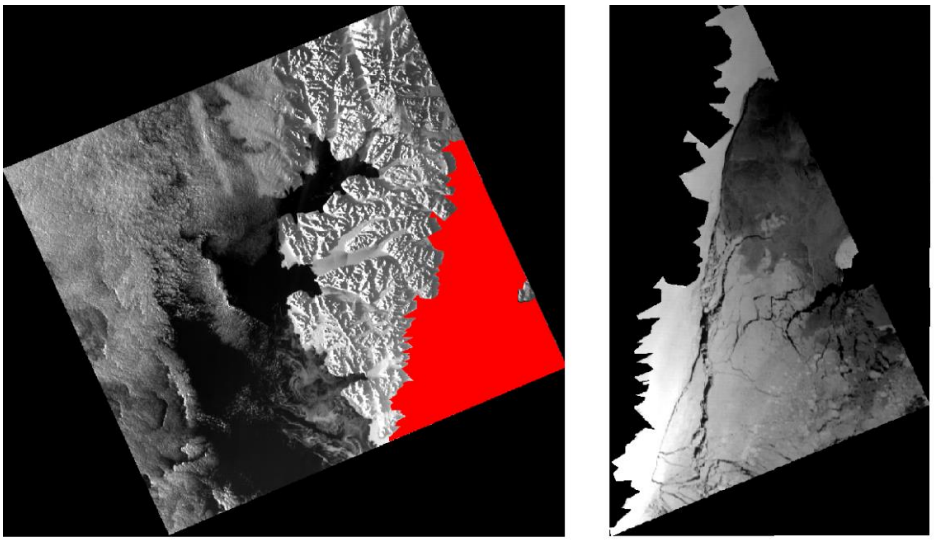

Figure 7.22: (Left) the roi highlighted in red, (Right) the extracted roi from (Left).

For the SAR data, extracting a region of interest is the last step in its pre-processing chain. Once all data has been multilooked, georeferenced, features extracted and downsampled, the same roi that is displayed in Figure 7.22 (Right) is extracted. This is shown in Figure 7.23. This image shows the roi of the Cross Pol Ratio (CPR) feature image, which will be explained in section 7.3.10, after it has been extracted. This image has the same dimensions, pixel for pixel, as the image in Figure 7.22 (Right).

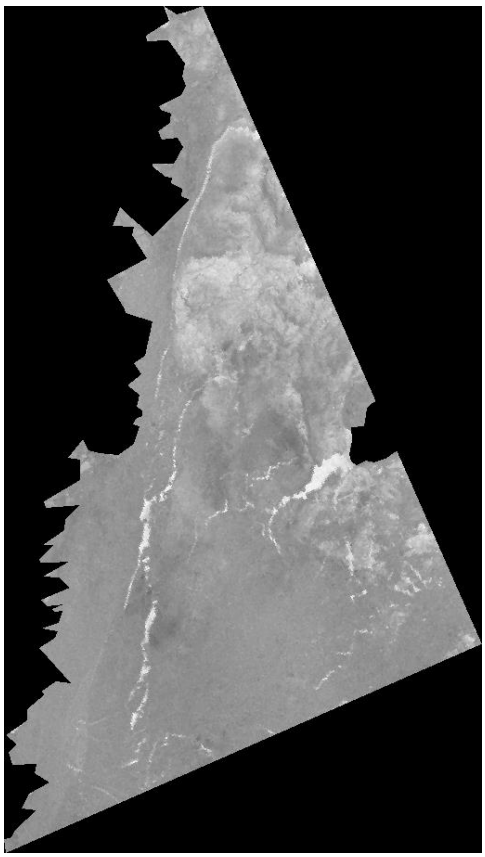

Figure 7.23: roi image of the CPR feature. This feature image has the same dimensions as the MODIS roi image in Figure 7.22 (Right).

7.3.6 Applying a Cloud Mask (MOD)

As already stated in section 7.2.1, cloud cover is a persistent problem that needs to be addressed when dealing with data obtained from optical satellites. While no cloud cover is present in the March 21 data, there is cloud cover in the MODIS scenes obtained on May 12. This is shown below in Figure 7.24, which shows a red band image of the Storfjorden archipelago taken at 04:15 in the morning. As can be seen in this image, cloud cover is clearly visible over the Eastern part of the fjord and at some locations around the Western part of the fjord. In order to mask this, the MODIS cloud mask product, MOD/MYD35, is used. This cloud product was obtained from the MODIS IST product (MOD/MYD29) which contains both the cloud and land masks. This is shown below in Figure 7.25. As can be seen the land mask is shown in a dark blue, the cloud cover is indicated by light blue and data visible to the satellite is indicated by the colour yellow. The cloud mask from the IST product has a resolution of 1000m.

As already stated in section 7.2.1 the cloud mask is generated by using up to 14 spectral bands. Table 7.3 shows which bands were used in the mask generation. This table is taken from (Ackerman, et al., 1998).

At periods of low illumination, the accuracy of the cloud mask is at its lowest. This is because at low illumination clouds and sea ice share similar reflectance characteristics at visible wavelengths. There is also the added problem that temperature inversions can cause the surface temperature of the sea ice to be colder than the clouds further obscuring the results of the final cloud mask generation (Hall, et al., 2004). In general, the absolute accuracy of the MODIS cloud mask product is unknown (Hall, et al., 2004).

Table 7.3: Bands that contribute to the cloud mask generation. The third column indicates weather a band is used in the cloud mask via a Y for yes and N for no.

Band	Central Wavelength (μm)	Used in Cloud Mask Generation
1 (250m)	0.659	Y (clouds, shadow)
2 (250m)	0.865	Y (low clouds)
3 (500m)	0.470	N
4 (500m)	0.555	N (snow)
5 (500m)	1.24	Y (snow)
6 (500m)	1.64	Y (snow, shadow)
7 (500m)	2.130	N
8	0.415	N
9	0.443	N
10	0.490	N
11	0.531	N
12	0.565	N
13	0.653	N
14	0.681	N
15	0.750	N
16	0.865	N
17	0.905	N
18	0.936	Y (low clouds)
19	0.940	Y (shadows)
26	1.375	Y (thin cirrus)
20	3.750	Y (shadow)
21/22	3.959	Y(21)/N(22) (window)
23	4.050	N
24	4.465	N
25	4.515	N
27	6.715	Y (high moisture)
28	7.325	N
29	8.550	Y (midmoisture)
30	9.730	N
31	11.030	Y (window)
32	12.020	Y (low moisture)
33	13.335	N
34	13.635	N
35	13.935	Y (high cloud)
36	14.235	N

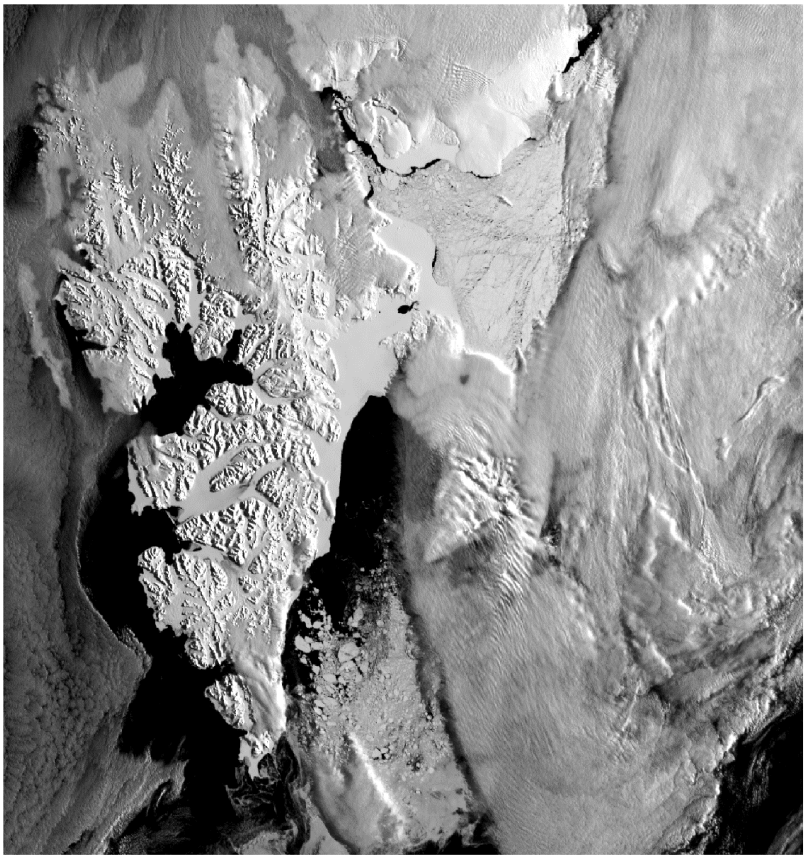

Figure 7.24: Red band image of the Storfjorden archipelago taken at 04:15 in the morning on May 12. Clouds are clearly visible mainly over the Eastern part of the Fjord and partially over the western part.

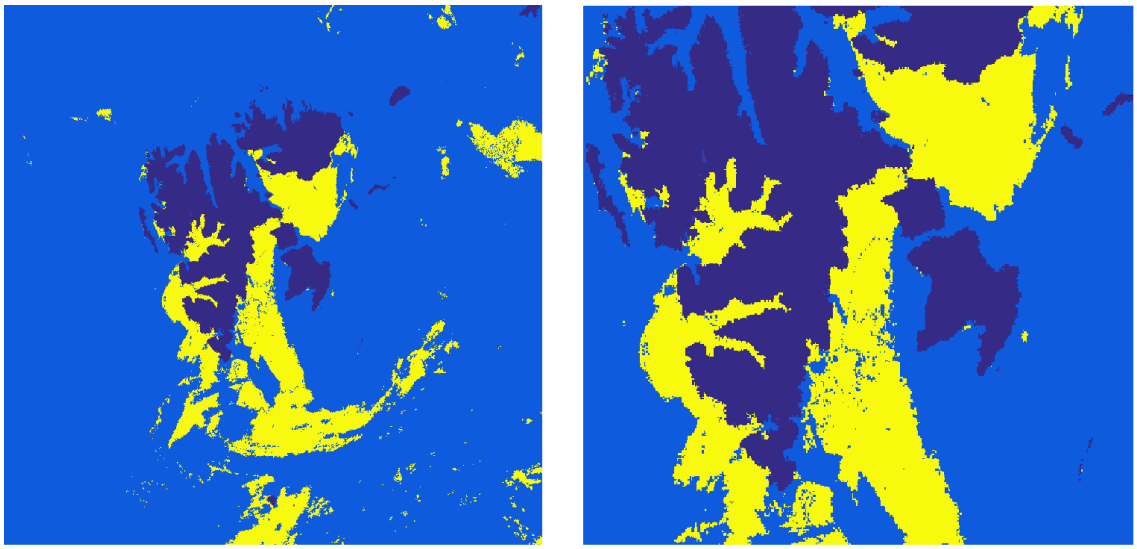

Figure 7.25: (Left/Right) Land and cloud mask taken from the MODIS IST products (MOD/MYD 29). Cloud is indicated by the light blue, land is indicated by the dark blue and area devoid of cloud is indicated by yellow.

7.3.7 Extracting non corrupted bands and performing PCA (MOD)

7.3.7.1 Corrupted bands

The MODIS data contains 36 bands. While this represents a wealth of spectral information not all bands will be suitable for use, due to the presence of missing lines and pixels. Missing lines in satellite data can be the result of sensor performance, communication problems or interferences and can look like anomalous lines that are highly contrasted with their surroundings (Chuvieco, et al., 2010). Some examples of bands with missing lines are shown below in Figure 7.26. This image shows bands 5, 27, 29 and 30 from the 21 March observation. As can be seen, the lines present are highly destructive and obscure much of the data.

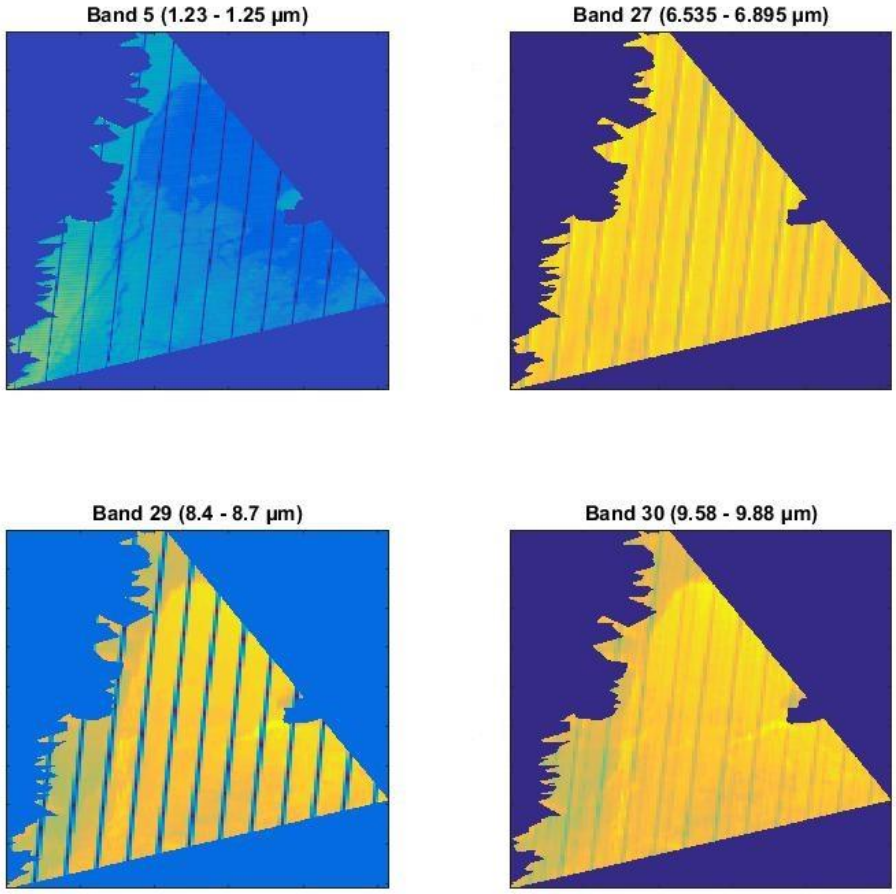

Figure 7.26: Images of bands 5, 27, 29 and 30 from the 21 March observation. As can be seen these bands contain corrupted lines which obscure much of the data.

(Chuvieco, et al., 2010) outlines several techniques that can be employed for the restoration of missing lines and pixels. Based on the work of (Cliff, et al.) and (Campbell, 1981),they note that pixels that are in close proximity to each other have a tendency to be spatially auto correlated to each other. Based on this vicinity criterion, they define various methods of restoration such as a simple substitution of DLs by previous values:

$$DL_{i,j} = DL_{i-1,j} \tag{7.1}$$

Where $DL_{i,j}$ represents the digital value of the pixel in the line i and column j, a substitution of missing pixels by the averaged value of the previous and subsequent pixel values:

$$DL_{i,j} = INT\{(DL_{i-1,j} + DL_{i+1,j})/2\} \quad (7.2)$$

Where the term $INT\{\_\}$ indicates a rounding off and, estimating the values of defective pixels from another band that is highly correlated with the defective band (Bernstein, et al., 1984).

$$DL_{i,j,k} = (s_k/s_r)\{DL_{i,j,r} - (DL_{i+1,j,r} + DL_{i-1,j,r})/2\} + (DL_{i+1,j,k} + DL_{i-1,j,k})/2 \quad (7.3)$$

Where s_k and s_r are the standard deviations of the band that is to be restored and the secondary band respectively.

Despite the availability of these restoration techniques, it was decided that any bands that displayed these anomalies would be discarded. This is because Storfjorden represents a relatively small geographic area and these anomalous bands introduce a large uncertainty about the true ice conditions that these lines obscure. This is shown below in a georeferenced image of band 29 from the 21 March data set in Figure 7.27. The portion of this image shown on the right shows that these lines occur roughly every 10 pixels with the lines having a spacing of 3 pixels in length. Each pixel in this image has a pixel size of 250 x 250m meaning the lines obscure 750m of ground pixels in width (as seen with pixels numbered 1, 2 and 3 in the Figure below.). Due to this, it was preferred to use bands where the certainty of ice conditions at each pixel was higher.

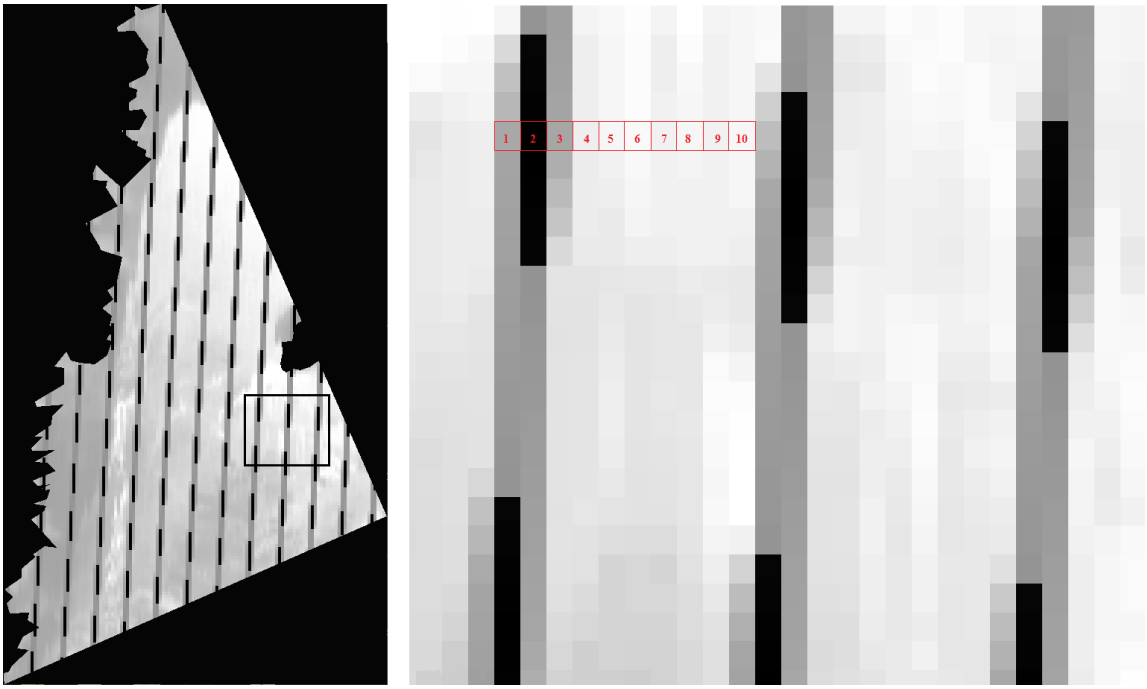

Figure 7.27: (Left) Image of band 29 from the 21 March observation. As can be seen, lines corrupting the data set are running down the length of the image. (Right) A close up showing three of the lines in (Left). Between the starting points of each line is roughly 10 pixels with the lines being three pixels in width.

7.3.7.2 PCA

After all bands with anomalous, corrupted lines were discarded, PCA was performed. The goal of PCA is to reduce the dimensionality of data sets that have large numbers of interdependent variables while at the same time attempting to retain as much of the variation in the data set as possible. The method by which this is achieved is by transforming the data to a new set of variables. These new variables are called principal components (PCs) and are uncorrelated and are ordered so that the first few will possess most of the variation that was present in all of the original variables.

The following brief summary of PCA was taken from (Jolliffe, 2002) and gives the standard derivation of PCs that are given in terms of eigenvectors and the covariance matrix.

Let $\mathbf{x}$ be a vector that contains p random variables. The goal is to seek a few derived variables that will preserve most of the information given by the variances and correlations of the random variables. The first step of PCA is to look for a linear function $\mathbf{c_1 x}$ of the elements of $\mathbf{x}$ that have maximum variance. Here, $\mathbf{c_1}$ is a vector containing p constants $c_{11}, c_{12}, \dots, c_{1p}$. Thus, we have

$$\boldsymbol{c_1 x} = c_{11}x_1 + c_{12}x_2 + \cdots c_{1p}\,x_p = \sum_{j=1}^{p} c_{1j}x_j \tag{7.4}$$

Once this is done, the next step is to find a linear function $\mathbf{c_2 x}$ that is uncorrelated with $\mathbf{c_1 x}$ and having maximum variance. The kth linear function, $\mathbf{c_k x}$, that is found will have maximum variance subject to the constraint that it is uncorrelated with $\mathbf{c_1 x}$, $\mathbf{c_2 x}$, … , $\mathbf{c_{k-1} x}$. The kth variable that is derived is the kth PC. The number of PCs that are found should equal the number of random variables that were in the original vector $\mathbf{x}$ but it is assumed that in general most of the variation in $\mathbf{x}$ will be accounted by the first few PCs.

The number of PCs that are kept depends on how much of the variance each one contained. For the 21 March observation the first 3 PCs out of 14 were kept. These 3 PCs contained 99,05% of the variance cumulatively. For the 12 May observation 4 PCs out of 18 were kept. These contained 97,56% of the variance cumulatively.

7.3.8 Converting Slant Range resolution to Ground Range resolution (RS2)

In SAR data, there are two common range measurements that are put to use. The first being the slant range R_0 and the second being the ground range R_g (Oliver, et al., 2004). Similar to any other radar, SAR measures the period of time between pulse transmission and pulse reception. This pulse travels along a straight line between the sensor and the surface of the Earth. The time delay that is associated with a reflection is changed into a distance measure. The distance measured along the line of sight from the sensor to the ground is referred to as the slant range. SAR sensors sample the return signal at periodic intervals in this direction.

This constant sampling in the range direction does not correlate to a constant sample spacing on the ground plane. This difference in sampling spacing between the slant plane and the ground plane is unique to radar images (McCandless, et al., 2004). The differences between these two types of resolutions is shown below in Figure 7.28. As can be seen, the slant range resolution δ_r has a constant value but the corresponding the ground range resolution δ_g differs.

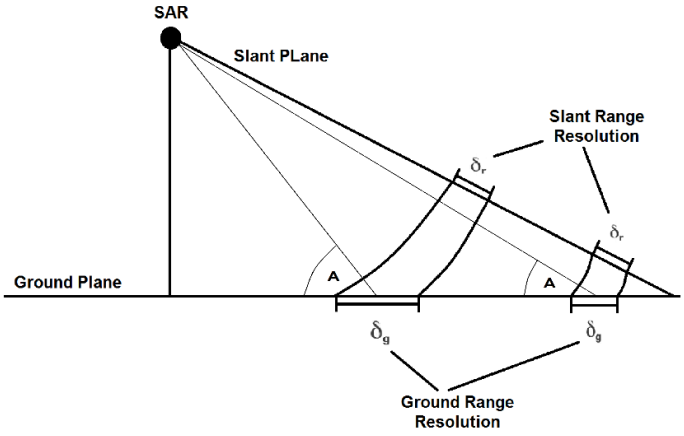

Figure 7.28: Diagram showing the differences between slant range resolution and ground range resolution.

The ground resolution is a function of the sensors grazing angle. The grazing angle is the angle between the line connecting the sensor and the point of Earth being viewed and the local tangent at that point. This is indicated by the letter A in Figure 7.28. Converting the slant range pixels to ground range will produce ground range pixels of differing sizes across the image. In order to offset this additional resampling is applied (McCandless, et al., 2004).

All RS2 ScanSAR products have been converted from slant range resolution and are provided in ground range resolution. RS2 QuadPol products are not corrected in this way and so must be converted in the pre-processing stage. However, it should be noted that in this study, this step was omitted due to time constraints.

7.3.9 Multi-looking (RS2)

As already mentioned in section 3.4, multi-look averaging, i.e. averaging over a specified neighbourhood of pixels, is a method that is applied to radar images in order to reduce the speckling effect. In this study the dual-pol ScanSAR Narrow data that is used, has a pixel spacing of 25m while the ScanSAR Wide data has a pixel spacing of 50m. Note: the ScanSAR products typically have pixel spacing's of 12.5m but are 2-look and 4-looked averaged before they become commercially available. The RS2 Fine-Quad data has a nominal pixel spacing of 4.7 x 5.1m in slant range.

As the MODIS data came in resolutions of 250m, 500m and 1000m, it was decided to multi-look the RS2 data so that it would have comparable resolutions to the MODIS data. For this end, the RS2 data set was 400-look averaged (20 in azimuth, 20 in range) for the ScanSAR Narrow data set, 100-look averaged (10 in azimuth, 10 in range) for the ScanSAR Wide data set and 1550-look averaged (50 in azimuth, 31 in range) for the QuadPol data set. The ScanSAR data was multilooked to this degree so as to bring the resolution roughly to 500m. This was done to avoid the so-called scalloping effect that is common in ScanSAR images. This is elaborated on in section 8.1.1. The QuadPol data was segmented to bring its resolution to 250m approximately.

The effect of performing multilooking can be seen below in Figure 7.29. This Figure shows the original HH band for the ScanSAR data taken on March 21 on the far left panel and has a region of interest indicated by a black square. The image second from the left, shows the region of interest without multilooking performed. The third and fourth images from the left show the region of interest that has been 100-looked and 400-looked respectively. As can be seen the effect of performing multi-looking with kernels of larger size is to degrade the resolution of the image. A notable advantage of performing multilooking is that specific features/structures that might not be visible in the original speckle filled image become more noticeable after multi-looking is performed. This can be seen below in Figure 7.29 (Centre right) and (Far right) where smaller distinct regions in the sea ice are more clearly visible after the multi-looking was performed.

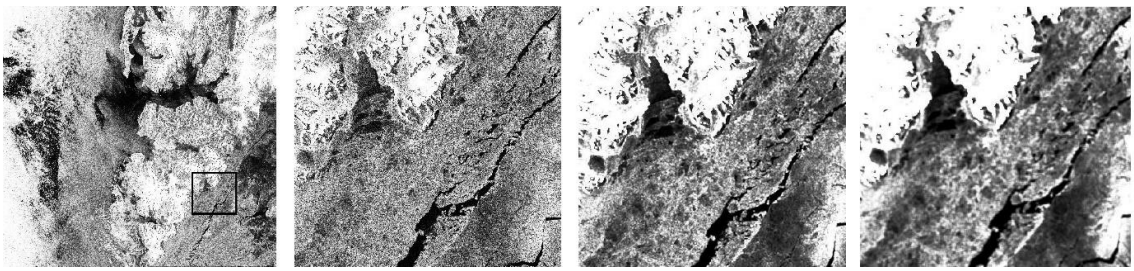

Figure 7.29: (Far left) Original ScanSAR Narrow HH image taken on 21 March 2013. (Centre left) Portion of the (Far left image) zoomed in. (Centre right/ Far right) Image shown in the (Centre left) panel mulilooked averaged with window sizes of 10x10 and 20x20 respectively. As can be seen, the image that underwent more averaging, shown in (Far right) has a more degraded resolution but more distinguished features.

7.3.10 Feature Extraction (RS2)

After multi-looking was performed, features that would be later used to segment the scene in question were generated. The "extended polarimetric feature space" (EPFS) method, as outlined by (Moen, et al., 2013) and (Doulgeris, et al., 2014) was chosen. (Moen, et al., 2013) describes this method as relatively simple to use, quite generic and was shown to give good results for the classification of sea ice. The feature space includes a basic set of five polarimetric features;

- Multi-variate Radar Cross Section (MRCS)
- cross-pol fraction (R_{CR})
- co-pol ratio (R_{CO})
- co-polarisation correlation magnitude ($|\rho|$)
- co-polarisation correlation angle ($<\rho$)

and a non-Gaussianity feature;

- Relative Kurtosis (RK)

Depending on the type of SAR data that is used, different numbers of these features will be able to be generated. This is shown below in Table 7.4 where + is used to indicate whether a feature can be generated and where – indicates a feature is unable to be generated. Since this study deals with both QuadPol (HH,HV,VH,VV) and Dual-pol (HH,HV) data sets, all six features can be generated for the case of QuadPol data and only the first three features can be generated for the case of Dual-pol data.

Table 7.4: Table showing the features that can be generated from the SAR data. Table taken from **(Doulgeris, 2013)**

	Quad	dual-co/cross	dual-co/co	mono
RK	+	+	+	+
MRCS	+	+	+	+
R_{CR}	+	+	-	-
R_{CO}	+	-	+	-
$\|\rho\|$	+	-	+	-
$<\rho$	+	-	+	-

The following section describes how these set of features are extracted from the radar data and the general meaning and interpretation behind them. Their interpretation is presented as it is given in (Moen, et al., 2013).

7.3.10.1 The Covariance Matrix

The ScanSAR dualpol data contains the detected amplitude of two possible combinations of transmit and receive polarization, those being HH and HV. In the theory of EM vector scattering operations the amplitude A, is magnitude of the complex scattering coefficient z. The two are related by the following formula

$$A = |z| = \sqrt{x^2 + y^2} \tag{7.5}$$

Where x is the real part of the signal and y is the imaginary part of the signal. The amplitude is related to the intensity via the equation

$$I = A^2 = |z|^2 \tag{7.6}$$

The covariance matrix, C, is constructed by assuming that the two channels, HH and HV, are uncorrelated. C is then given by

$$C = \langle \begin{bmatrix} I_{HH} & 0 \\ 0 & I_{HV} \end{bmatrix} \rangle = \frac{1}{L} \sum_{i=1}^{L} \begin{bmatrix} I_{HH} & 0 \\ 0 & I_{HV} \end{bmatrix} \tag{7.7}$$

Where L is the number of looks.

The RS2 QuadPol data contains the complex scattering coefficients for all the possible polarization combinations of transmit and receive. The scattering vector is given by

$$s = [s_{HH}, s_{HV}, s_{VH}, s_{VV}]^T \tag{7.8}$$

From this the reduced scattering vector is calculated

$$s_{red} = [s_{HH}, s_X, s_{VV}]^T = \left[s_{HH}, \frac{1}{\sqrt{2}}(s_{HV} + s_{VH}), s_{VV} \right]^T \tag{7.9}$$

s_{red} is constructed under the assumption of reciprocity i.e. $s_{HV} \approx s_{VH}$. The operator $(\ )^T$ indicates the presence of a transpose operation and the $\frac{1}{\sqrt{2}}$ factor establishes that the s_X term maintains the power contained in the two terms s_{HV} and s_{VH}. The covariance matrix is then constructed by averaging over a neighbourhood of the product of reduced scattering vectors. This is given by the equation

$$C = \frac{1}{L} \sum_{i=1}^{L} s_i s_i^H = \begin{bmatrix} \langle S_{HH} S_{HH}^* \rangle & \langle S_{HH} S_{HV}^* \rangle & \langle S_{HH} S_{VV}^* \rangle \\ \langle S_{HV} S_{HH}^* \rangle & \langle S_{HV} S_{HV}^* \rangle & \langle S_{HV} S_{VV}^* \rangle \\ \langle S_{VV} S_{HH}^* \rangle & \langle S_{HH} S_{HV}^* \rangle & \langle S_{VV} S_{VV}^* \rangle \end{bmatrix} \tag{7.10}$$

Where the operator $(\ )^H$ indicates the presence of the Hermitian transpose operation and $\langle\ \rangle$ indicates the average over L reduced scattering vectors in the defined local neighbourhood.

7.3.10.2 Relative Kurtosis

The relative kurtosis is given by the following formula

$$RK = \frac{1}{Ld(d+1)} \sum_{i=1}^{L} \left[s_i^H C^{-1} s_i \right]^2 \tag{7.11}$$

Where d is the dimensionality of the input vectors, $d = 2$ for the case of the DualPol data and $d = 3$ for the case of the QuadPol data. The above expression can be easily evaluated for the QuadPol data as these data products contain the complex scattering coefficients *s*. The dual pol data only contains the amplitude of the scattering coefficients and so all phase information is lost. By evaluating the above equation further, we can see that this is not a problem.

Consider the inverse of the covariance matrix. Since the covariance matrix is diagonal, the inverse will be simply be the inverse of its elements on the main diagonal. This is shown below

$$C^{-1} = \begin{bmatrix} \frac{1}{\langle I_{HH} \rangle} & 0 \\ 0 & \frac{1}{\langle I_{HV} \rangle} \end{bmatrix} \tag{7.12}$$

This means that

$$\frac{1}{Ld(d+1)} \sum_{i=1}^{L} \left[s_i^H C^{-1} s_i \right]^2 = \frac{1}{Ld(d+1)} \sum_{i=1}^{L} \left[\begin{bmatrix} S_{HH}^* & S_{HV}^* \end{bmatrix} \begin{bmatrix} \frac{1}{\langle I_{HH} \rangle} & 0 \\ 0 & \frac{1}{\langle I_{HV} \rangle} \end{bmatrix} \begin{bmatrix} S_{HH} \\ S_{HV} \end{bmatrix} \right]^2 \tag{7.13}$$

$$\frac{1}{Ld(d+1)} \sum_{i=1}^{L} \left[s_i^H C^{-1} s_i \right]^2 = \frac{1}{Ld(d+1)} \sum_{i=1}^{L} \left[\begin{bmatrix} S_{HH}^* & S_{HV}^* \end{bmatrix} \begin{bmatrix} \frac{1}{\langle I_{HH} \rangle} S_{HH} \\ \frac{1}{\langle I_{HV} \rangle} S_{HV} \end{bmatrix} \right]^2 \tag{7.14}$$

$$\frac{1}{Ld(d+1)} \sum_{i=1}^{L} \left[s_i^H C^{-1} s_i \right]^2 = \frac{1}{Ld(d+1)} \sum_{i=1}^{L} \left[S_{HH}^* \frac{1}{\langle I_{HH} \rangle} S_{HH} + S_{HV}^* \frac{1}{\langle I_{HV} \rangle} S_{HV} \right]^2 \tag{7.15}$$

$$\frac{1}{Ld(d+1)}\sum_{i=1}^{L}\left[s_i^H C^{-1} s_i\right]^2 = \frac{1}{Ld(d+1)}\sum_{i=1}^{L}\left[\frac{S_{HH}^* S_{HH}}{\langle I_{HH}\rangle} + \frac{S_{HV}^* S_{HV}}{\langle I_{HV}\rangle}\right]^2 \tag{7.16}$$

By the above equations;

$$S_{HH}^* S_{HH} = I_{HH} \text{ and } S_{HV}^* S_{HV} = I_{HV} \tag{7.17}$$

This gives us a formula for the RK for the case of DualPol data

$$S_{HH}^* S_{HH} = I_{HH} \text{ and } S_{HV}^* S_{HV} = I_{HV} \tag{7.18}$$

$$RK = \frac{1}{Ld(d+1)}\sum_{i=1}^{L}\left[s_i^H C^{-1} s_i\right]^2 = \frac{1}{Ld(d+1)}\sum_{i=1}^{L}\left[\frac{I_{HH}}{\langle I_{HH}\rangle} + \frac{I_{HV}}{\langle I_{HV}\rangle}\right]^2 \tag{7.19}$$

Since the data in its original form represents amplitude, and the intensity is the square of the amplitude, this expression can be evaluated pixel per pixel.

The RK is a measure, statistical in nature, that gives some indication of the shape of the distribution. The kurtosis in general, is a measure of the cumulative weight of the tail of a distribution relative to the rest of the distribution. It is this kurtosis measure, divided by the absolute kurtosis of a Gaussian distribution that results in the RK. This is what the term 'relative' in the quantity's name refers to.

If the RK has a high value, the distribution will have a distinctive sharp peak near the mean of the distribution and a rapid decline away from the mean. Gaussian distributions occur when there is a large number isotropic scatterers. Thus if the RK has a large value it can be indicative of rubble fields, ice deformities, ice edges or any other ice characteristic that can create strong backscatter.

7.3.10.3 Geometric Brightness (MRCS)

This quantity is given by the equation

$$B = \sqrt[d]{\det(C)} \tag{7.20}$$

and represents the intensity of the backscatter. This quantity is related to the roughness and geometric shape of the target as well as its orientation with respect to the sensor.

7.3.10.4 Cross-polarization ratio

This quantity is given by the equation

$$R_{cross} = \frac{\langle s_{HV} s_{HV}^* \rangle}{B} \tag{7.21}$$

Based on the work of (Scheuchl, et al., 2001) it was found that the HV channel is able to discriminate between sea ice and open water quite well. The ratio presented above serves to provide an estimate on the amount depolarization which is indicative of the age and ice type that is in question. According to (Haykin, et al., 1994) the degree of depolarization is not constant across the sea ice but varies with the ice type and structure as it relies on factors such as volume scattering and multiple bounce reflections. They state that sea ice of the volume scattering variety i.e. cold, old, multi-year ice will have relatively high depolarization ratios while rough surface scattering ice will, typically first year ice will have lower depolarization ratios. Fracture features such as ridges and ice edges can produce large-scale surface scattering and have very high depolarization ratios.

7.3.10.5 Co-polarization ratio

This quantity is given by the formula

$$R_{VV/HH} = \frac{\langle s_{VV} s_{VV}^* \rangle}{\langle s_{HH} s_{HH}^* \rangle} \tag{7.22}$$

According to (Scheuchl, et al., 2001) this measure provided good results for separating open water from thin ice. The value for this ratio is primarily determined by the dielectric constant of the material in question. According to (Onstott, et al., 2004), largest ratios will be seen for new, young sea ice and open water as they have high dielectric values. Older sea ice, like first year ice and multiyear ice will have values less than roughly equal to 1.

7.3.10.6 Co-polarization correlation magnitude

This quantity is given by the formula

$$|\rho| = \left| \frac{\langle s_{HH} s_{VV}^* \rangle}{\sqrt{\langle s_{HH} s_{HH}^* \rangle \langle s_{VV} s_{VV}^* \rangle}} \right| \tag{7.23}$$

(Gill, et al., 2012) showed that the value of $|\rho|$ tended to increase with an increase of incidence angle and deformation. They found that the values for this quantity were largest for the open water, followed by smooth first year ice. Despite this, its purpose in sea ice research is still a matter of active research according to (Onstott, et al., 2004).

7.3.10.7 Co-polarization correlation angle

This quantity is given by the formula

$$< \rho = < (\langle s_{HH} s_{VV}^{*} \rangle) \tag{7.24}$$

According to (Thomsen, et al., 1998) this measure has been good at discriminating between open water and sea ice and has been used as a method of determining the thickness of sea ice less than or equal to 30cm. the value for this measure is mainly determined by the dielectric constant of the sea ice (Onstott, et al., 2004).

7.3.11 Down sampling to 250m resolution (RS2)

After the three ScanSAR feature images (RK, MRCS and R_{CR}) were generated and then georeferenced they were down sampled to the common resolution of 250m in order to have them in alignment with the MODIS images. The objective of this step is to have the ScanSAR feature images at the same pixel spacing as the MODIS PCA image before classification is performed.

When the resize factor is less than one, as it is here, ENVI offers two resampling options to resize the data; those being the nearest neighbour method and the pixel aggregate method. The nearest neighbour method was again chosen as the method to down sample the data, due fact that it is less computationally intensive than the pixel aggregate method and that image smoothing was already performed at an earlier stage i.e. the multi-looking stage.

The diagram in Figure 7.30 shows the process of down sampling in this way. This Figure shows a 16 pixel image on the left that was down sampled, using the nearest neighbour method, by a factor of a half, to produce the 4 pixel image on the right. As can be seen here, the 'nearest neighbours' in this case are considered the green, pink, brown and light green pixels in the left hand image. The other pixels are discarded.

Note: while this may seem like a loss of information it is worth remembering that in images of natural scenes, neighbouring pixels tend to be correlated, this is stated in section 7.3.7.1 and is based on the work of (Cliff, et al.) and (Campbell, 1981).

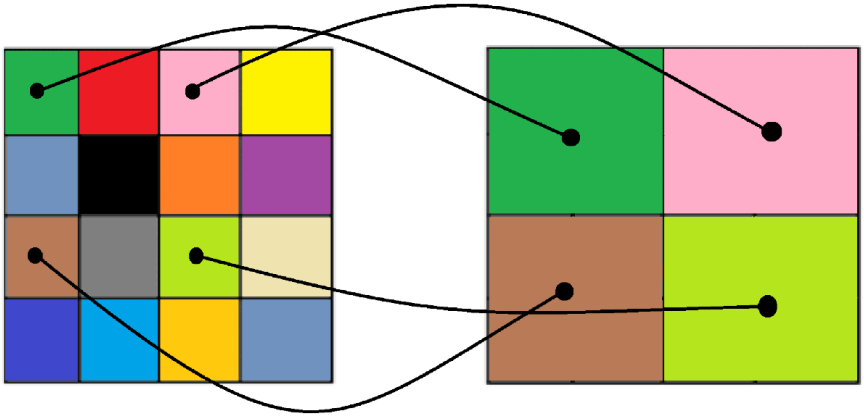

Figure 7.30: Image showing the process by which nearest neighbour down sampling occurs.

7.4 Mixture of Gaussian with Markov Random Field Smoothing

The method of segmentation chosen was the Mixture of Gaussian Method with Markov Random Field contextual smoothing performed after classification. This segmentation algorithm is applied to both the PCA image for the MODIS data and the polarimetric features generated for the SAR data. The sections below provide a basic introduction to the theory of this segmentation and smoothing method. The theory outlined in the sections below were sourced from the books by (McLachlan, et al., 2000) and (Theodoridis, et al., 2009) as well as the papers by (Doulgeris, 2014).

The Mixture of Gaussian modelling method belongs to a certain class of statistical modelling techniques called Finite Mixture Modelling (FMM). FMM has its origins in the work of Karl Pearson, who in 1894 (Pearson, 1894), was able to fit a mix of two Gaussian probability density functions that had two different mean values, μ_1 and μ_2, and two different values for variance, var_1 and var_2 to the data composed of measurements of the ratio of forehead to body length of 1000 crabs sourced of the coast of Italy. As already stated this is one of the earliest examples of mixture of Gaussian modelling being applied to study real world phenomena. Over the last 25 years, corresponding to the availability of high-speed computers, these methods have gained increasing interest in estimation for Gaussian mixtures, particularly since notable work by (Lindsay, et al., 1993) was performed.

A Gaussian Mixture model is one that assumes that all data points in a data set are composed from a mixture of a finite number of Gaussian distributions. The parameters for these Gaussian distributions are unknown. In the simplest case, it is assumed that *N* Gaussian distributions contribute to the overall formation of a probability distribution function (pdf). In this way this modelling technique assumes that each point *x*, can be drawn from any of the *N* model distributions with a probability of $P_j, j = 1,2, \dots, J$. The Mixture of Gaussian model attempts to optimize the fit between the data and the model. Many pdf's that are not Gaussian in nature may be approximated by a discrete mixture of several of these Gaussian distributions. The benefit of this is that a pdf that can be modelled as a mixture of several Gaussian distributions can allow for easier numerical solutions as the solutions for Gaussians are known reasonably well. The reader is referred to (Theodoridis, et al., 2009) for a more in depth discussion

Markov Random Field (MRF) smoothing was a smoothing method that was applied after the segmentation process. This method smooths over a set of discrete areas that are defined using a set of area labels. The result is that the final segmentation classes look more homogenous.

The method applied in this thesis is the same as outlined in (Doulgeris, 2013) and (Doulgeris, et al., 2010). All MATLAB code that was used to perform the segmentation of data was provided by Dr. Anthony Doulgeris.

7.5 Method of Comparison

A simple visual comparison was the method chosen to compare the results of the segmentation algorithm. Although it is assumed the segmentation of these two different data types will provide information on the spatial distribution of ice types in the fjord, there is little information available on the class labels, beyond some large-scale ice types as seen in the meteorological ice charts in section 7.1.1, for the distribution of sea ice in Storfjorden. This complicates the matter of comparing the segmentation results considerably as there is little a posteriori information available.

The difficulty in comparing these results is also compounded by the fact that the physical principals, in which these two data types were acquired, differ greatly. As already mentioned, SAR, when it is detecting young, FYI, is sensitive to primarily the surface roughness properties of the material, while MODIS is sensitive to the thickness of the material. Any unsupervised clustering of images from these two data types is expected to provide information about the ice in terms of its thickness or roughness. While the two characteristics are known to be somewhat related according to (Peterson, et al., 2008) and (Onstott, et al., 2004), it is not possible, definitively, to draw simplistic conclusions such as 'ice that is thick is also rough', or vice versa, due to the multitude of ways sea ice can form and under different conditions.

Thus, it was decided to compare the results of the segmentation in a qualitative fashion rather than a quantitative one. This involved acquiring a priori information about the fjord from various scientific papers, some notable ones are (Preußer, et al., 2015) and (Haarpainter, et al., 2001), and acquiring atmospheric data from the Norwegian meteorological office from the two weather stations that are closest to Storfjorden. Based this preliminary information , which is outlined in the first few sections of this chapter, and the theory related to sea ice, SAR and optical sensors, which is outlined in chapters 2-4 of this thesis, a case is built for any similarities and differences that are observed in the segmentation results.

It should be noted that some quantitative comparison measures were considered for the purposes of comparing the results of the segmentation of the RS2 and MODIS images. A notable one is the Jaccard similarity coefficient. This gives a measure of the degree of overlap between identified classes. This coefficient is calculated by dividing the area of the intersection of two classes by the area of the union of the two classes. This coefficient ranges from zero to one; zero indicating no overlap and 1 indicating 100% overlap. This is demonstrated below in Figure 7.31. In this image, we see two classes A and B. The Jaccard similarity coefficient is calculated by dividing the area of the red region, which is the intersection of the two sets, by the area of the orange region, which is the area of the union of the two sets. This measure could prove useful for comparing the results between simple surface features from the two sensors that are known to be present. For example, we could use this measure to compare how well SAR compared to optical in retrieving water from a scene. This is not explored further in this thesis but does constitute a line of investigation for the future.

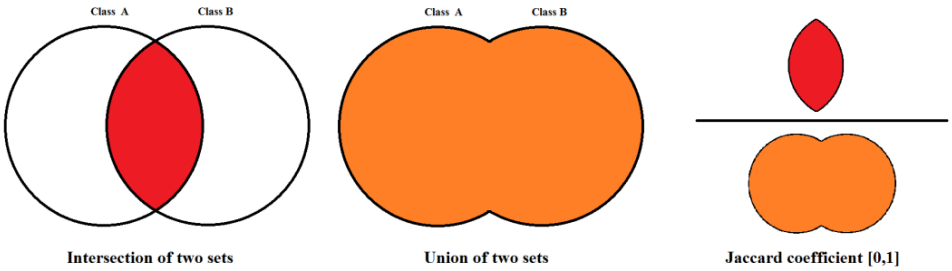

Figure 7.31: Method by which the Jaccard similarity coefficient is calculated. The area of the intersection of the two sets, A and B is divided by the area of the union of the two sets. The result is a coefficient between zero and one.

8 Results and Discussion

The following chapter contains the results of this study and their interpretation. In total, four comparisons were made for the purpose of comparing and contrasting segmentation results from both MODIS and RS2. The comparisons are as follows;

- Comparison 1 attempts to explain the differences and similarities seen between segmentation results for data taken on March 21. This is a comparison between MODIS and RS2 dual-pol ScanSAR Narrow data.
- Comparison 2 attempts to explain the differences and similarities seen between segmentation results for data taken on May 12. This comparison is between MODIS and RS2 ScanSAR Wide data.
- Comparison 3 attempts to compare and contrast data taken from MODIS on May 12 and RS2 QuadPol data taken on May 10.
- Comparison 4 attempts to compare the thickness of the landfast ice, acquired from HEM and a roughness characteristic derived from the HEM measurements. This comparison was made with reference to the MODIS and RS2 May 12 ScanSAR Wide segmentation results.

The comparisons are designed to answer the following questions; is it possible for MODIS and RS2 to detect the same, spatially homogenous regions of similar ice type? In addition, is it possible for MODIS and RS2 to derive different classification results for ice types in similar regions i.e. can one sensor see a particular aspect of the ice that the other cannot?

Each comparison begins with a short recap on the conditions that are known/strongly believed to be present in the Fjord at the time of data acquisition. This is followed by a short discussion on the individual features that were derived from the pre-processing stage and then inputted into the segmentation algorithm, which is then followed by comparing classification results for two specific cases.

In the first case, the scene was segmented into a number of regions that were strongly believed to best represent the major, large scale ice types present in the fjord i.e. landfast ice, drift ice etc. This means that segmentation was stopped after it was decided the algorithm found the best representation of these major ice types.

The second case deals with comparing classification results between the two scenes after they were segmented further.

The reasoning behind comparing classification results in this way is that it is reasoned the segments found in case one will broadly represent the major ice types known to be present in the fjord and the segments found in case two will be indicative of the smaller scale ice types that comprise these major ice types.

8.1 Comparison 1: March 21 (MODIS to RS2 (Dual-Pol ScanSAR Narrow))

8.1.1 Preliminary

Based on a priori knowledge, some general information can be drawn about the scene before any segmentation is performed. Figure 8.1 shows a true colour MODIS image (pixel spacing: 500m, R= band 2, G = band 1, B = band 4) of the scene next to the same image with homogenous ice types manually

discriminated. This image shows that there is land fast ice to the left of the scene, which corresponds, to the westerly part of the fjord. Thin drift ice can be seen next to the land fast ice in the middle background of the image, which corresponds to the northern and North Eastern parts of the fjord. This is in direct agreement with the findings of (Preußer, et al., 2015) who showed that there is a high frequency of ice with thickness less than 20cm in this part of the fjord between January and March for the year 2013. This is also in agreement with (Haarpainter, et al., 2001) who stated that there is typically a polynya in this part of the fjord due to the prevalence of northerly to northeasterly winds. The presence of these northeasterly winds for the time this data was acquired is also confirmed by the wind direction chart in Figure 7.8 from Hopen Island.

Located in the centre middle ground to left foreground we can see thicker drift ice followed by the same type of drift ice but with a more 'spotty' appearance to it. This can be seen in the right foreground of the image. Note; it is supposed that this rough, 'spotty' like ice, are large pieces of ice that have frozen in place. Also can be seen are open leads. It is suspected that these leads are comprised of either open water or grease ice as these structures appeared sometime between mid-day of the 20th March and 21st March. This is shown in Figure 8.2 below. This figure shows Storfjorden during the afternoon of 20 March and again on 21 March, demonstrating that the leads present in the data set appeared at some point during this period.

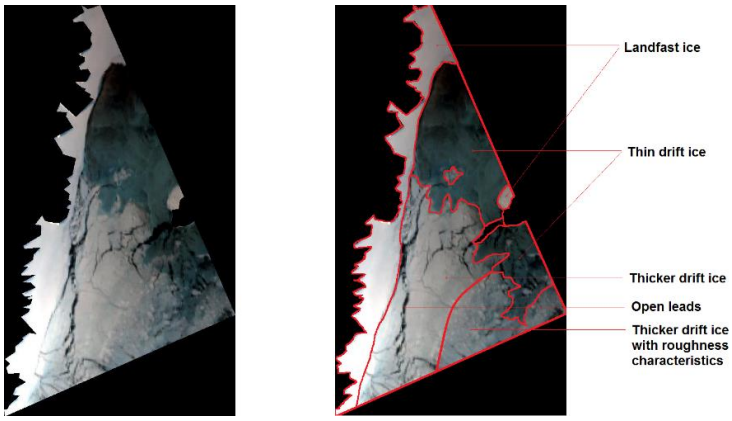

Figure 8.1: MODIS true colour image of the scene under investigation on 12 May. In this image, four different ice types can be seen. These include landfast ice, thin drift ice, thicker drift ice

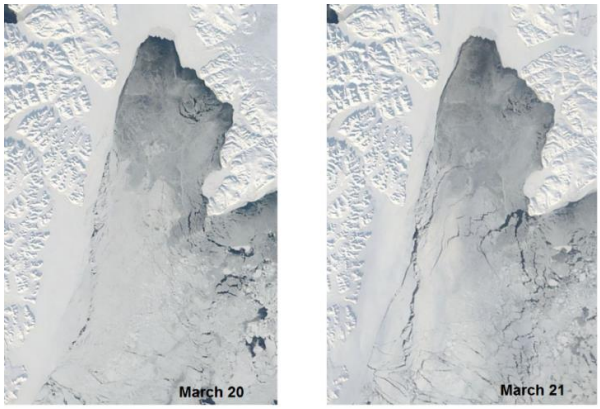

Figure 8.2: (Left) MODIS true colour image taken on 20 March. (Right) MODIS true colour image taken on 21 March. as can be seen, the leads in (Right) appeared sometime between midday 20 March and 21 March implying the leads in the 21 March observation are either open water or new ice.

8.1.2 Features Segmented

8.1.2.1 ScanSAR Narrow Features

Figure 8.3 shows the three features that were generated from the ScanSAR Narrow data. The top three panels show the features as they were generated for the entire scene. The bottom three panels show the three features but with the region of interest i.e. Storfjorden, segmented out. As can be seen in this Figure, the region of interest lies at the very edge of this scene. Examining these features, it is easy to see the different characteristics that are captured by these features. The RK captures a lot of the information related to the texture of the scene. The open leads are quite prominent which is to be expected as these areas will be more textured/rougher than the relatively flatter and smoother areas of open water and sea ice. The MRCS seems to show a clear distinction between the very thin drift ice and the thicker drift ice and landfast ice. The Cross-pol ratio does not seem to show much distinction between the various ice types but does seem to show a clear distinction between sea ice in general and open water.

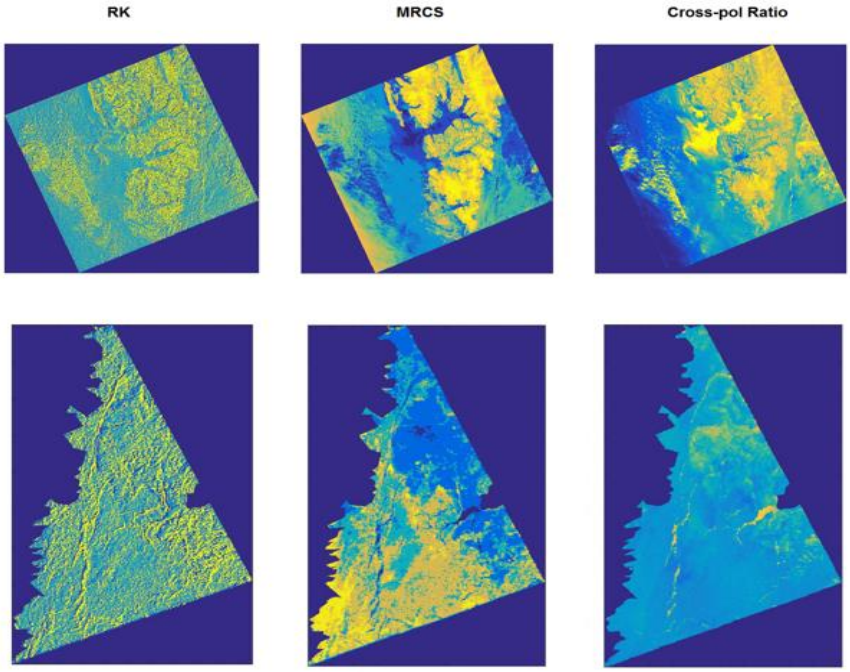

Figure 8.3: (TOP) ScanSAR Narrow features that were generated. (Bottom) The three features in the top row with the roi segmented out.

8.1.2.2 MODIS Features (PCA image)

As stated in section 7.3.7, not all bands will be suitable for use due to corruptions that occur in the retrieved data. After the data was pre-processed via georeferencing, atmospheric correction, down sampling etc., the 36 data bands were inspected for these anomalous corruptions. Table 8.1 on the next page highlights the bands that were kept and the ones that were discarded. The bands that were kept were transformed into a new space via PCA. It was found that the first three principal components contributed the most variance to the new feature space so these were kept and used for segmentation. Figure 8.4 shows an RGB image made using the first three principal components. Figure 8.5 shows a bar graph showing, in percent, how much each component contributes to the variance. Table 8.2 displays both the cumulative percentages of the contributions from each component and the individual percentage contribution from each component. As can be seen from this table, the first three components contribute

93,16, 4,49 and 1,40% of the variance respectively. Cumulatively, they contribute 99,05% of the variance.

Table 8.1: Bands that were kept and those that were discarded.

Band	Kept or Discarded
1 (250m)	Kept
2 (250m)	Kept
3 (500m)	Discarded
4 (500m)	Kept
5 (500m)	Discarded
6 (500m)	Discarded
7 (500m)	Discarded
8 (1km)	Discarded
9 (1km)	Discarded
10 (1km)	Discarded
11 (1km)	Discarded
12 (1km)	Kept
13 (1km)	Kept
14 (1km)	Discarded
15 (1km)	Kept
16 (1km)	Discarded
17 (1km)	Discarded
18 (1km)	Kept
19 (1km)	Kept
20 (1km)	Kept
21 (1km)	Kept
22 (1km)	Discarded
23 (1km)	Kept
24 (1km)	Discarded
25 (1km)	Discarded
26 (1km)	Kept
27 (1km)	Discarded
28 (1km)	Discarded
29 (1km)	Discarded
30 (1km)	Discarded
31 (1km)	Discarded
32 (1km)	Discarded
33 (1km)	Kept
34 (1km)	Kept
35 (1km)	Discarded
36 (1km)	Discarded

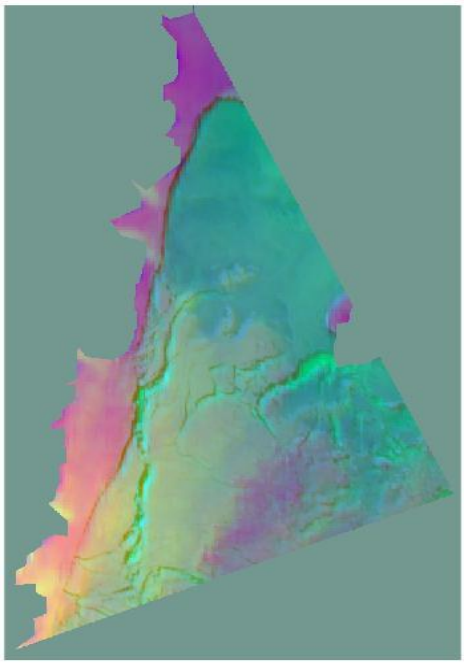

Figure 8.4: PCA image generated from the 14 bands that were kept.

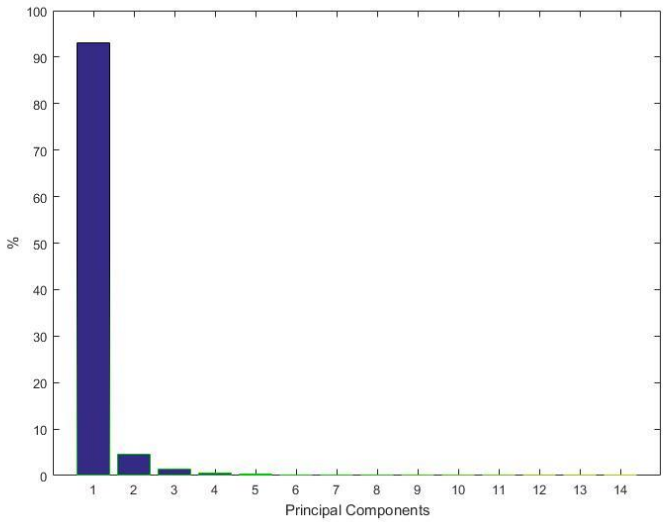

Figure 8.5: Bar graph showing the amount of variance contained within each principal component.

Table 8.2: Top row: Cumulative percentage variance contributed to each component. Bottom row: individual percentage contributed to each component.

1st	2nd	3rd	4th	5th	6th	7th	8th	9th	10th	11th	12th	13th	14th
93,16	97,65	99,05	99,48	99,75	99,87	99,95	99,97	99,9881	99,9939	99,9967	99,9984	99,999	100
93,16	4,49	1,40	0,42	0,27	0,11	0,08	0,02	0,017	0,0058	0,0027	0,0017	0,001	0,0003

8.1.2.3 Anomalous SAR artefacts and feature modifications

Before the results are presented, a brief description of two anomalous artefacts that are visible in the SAR images is presented, as well as modifications that was made in order to curtail them. The first artefact that was observed is the presence of a banding effect at the edge of the scene. Figure 8.5 shows a SAR image segmented into seven classes, for an example, with this banding effect visible at the edge of the scene. It is not known exactly what is the cause of this artefact, but it is suspected it is due to an effect called inter-scan banding (ISB). This effect is due to the operational mechanics of the SAR in ScanSAR mode. When in this mode the SAR takes scans sequentially across the range direction. This banding effect appears between two neighbouring scans as an intensity difference between their borders (Iqbal, et al., 2012). The scanning process can be seen below in Figure 8.6. In order to mitigate this effect the mask, as seen below as the black area in Figure 8.5 was inset to cover the banding that occurred at the edge of the scene. This is why in the subsequent discussion both segmented features from SAR and MODIS have a mask that is slightly inset to the ones seen in Figure 8.3 and 8.4. As the removal of this effect is currently an active area of research, the removal of this effect is beyond the scope of this study. Thus, it was decided to remove this anomalous region via altering the mask rather than have it possibly skew results in the segmentation stage.

It should also be mentioned that a grainy like pattern was observed in the SAR images that seemed to run along the azimuth direction. It is highly likely this effect was due to scalloping, which is common to ScanSAR images. In order to mitigate this the RS2 images were multilooked to 500m resolution rather than 250m resolution. The averaging window was large enough to average over this effect. Note; the removal of this too is an active area of research so addressing here was beyond the scope of this study.

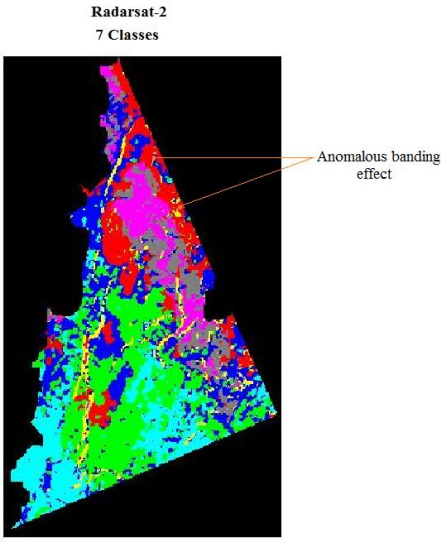

Figure 8.5: Anomalous banding effect can be seen in this RS2 image that was segmented into seven classes.

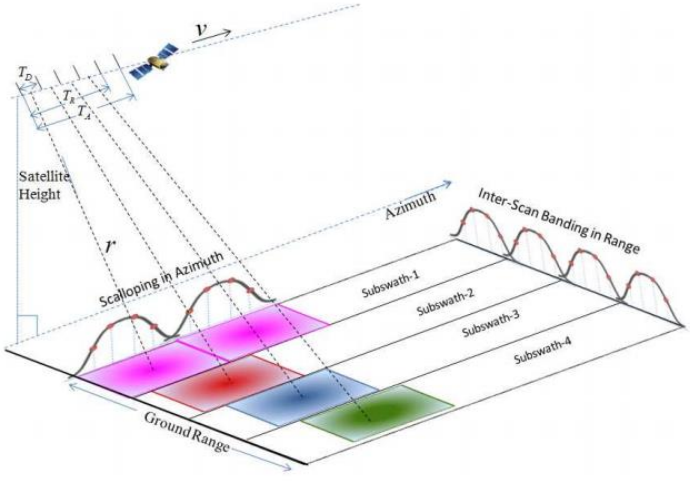

Figure 8.6: image taken from **(Iqbal, et al., 2012)** showing the mechanism by which this banding effect occurs.

8.1.3 Case 1: Comparison between low number of clusters

8.1.3.1 Description

For MODIS, five classes was determined to be the best number of clusters for representing the large scale ice types found in the fjord. For RS2, 5 was also determined to be the best number. The results are shown below in Figure 8.7 for both data types. The decision to stop at five clusters was reached by inspecting what happens when the scene is segmented beyond 5 classes. Figure 8.8 shows both scenes segmented for 6 and 7 classes. As can be seen beyond, 5 clusters the major ice types that were able to be derived, begin to be segmented further. This can be seen in the MODIS image by how different regions within the land fast ice begins to be further discriminated and in the RS2 images by how areas of the thicker drift ice begin to be segmented further**.** These cases will be discussed in more detail in section 8.1.4.

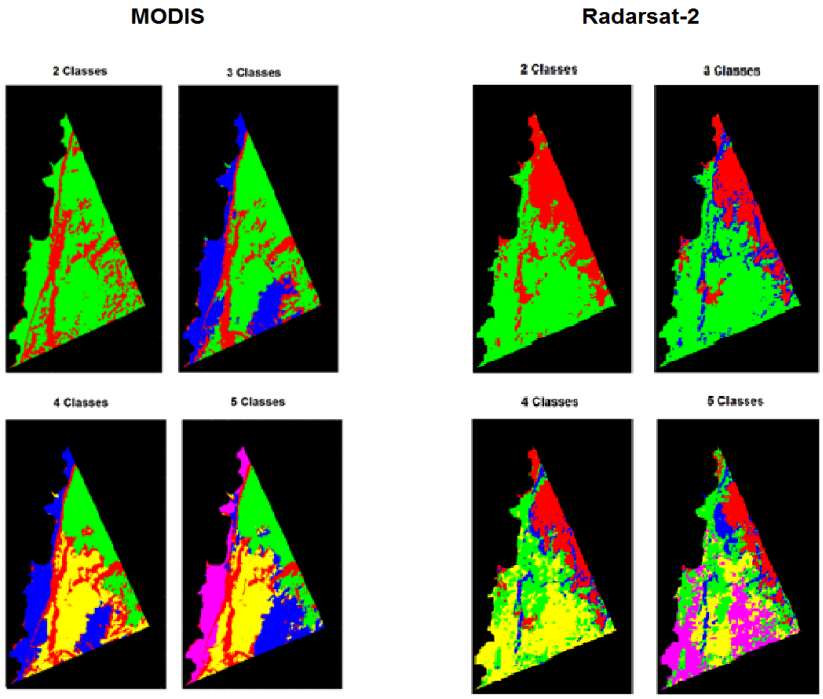

Figure 8.7: MODIS and RS2 features segmented to 2, 3, 4 and 5 classes. These classes were estimated to best represent the major ice types present in the fjord.

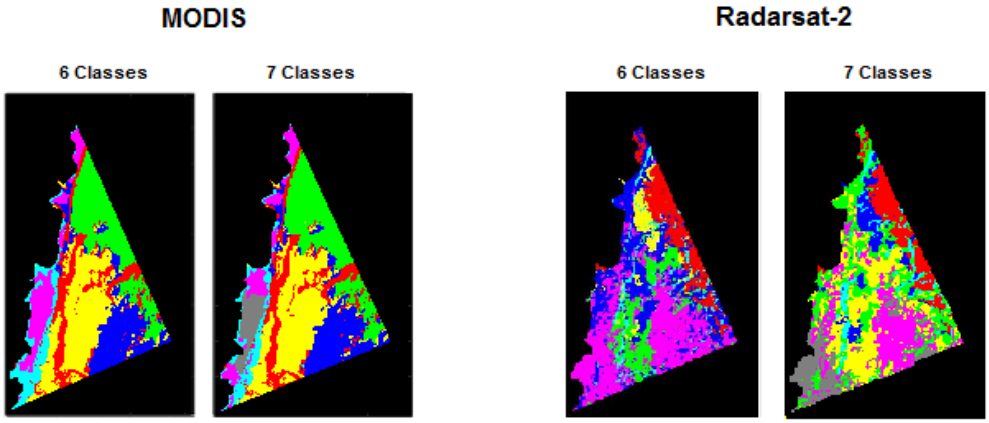

Figure 8.8: MODIS and RS2 features segmented to 6 and 7 classes. As can be seen, the major ice types begin to be further divided in these images. This is especially apparent in the MODIS segmentation results.

8.1.3.2 Discussion

One of the most obvious differences that can be seen in the Figure 8.7 between the MODIS segmentation results and the RS2 segmentation results is that MODIS easily segments the scene into distinct and separate regions. Consider the 5-class MODIS image from Figure 8.7. This is shown again in Figure 8.9 below. In this image, all the ice classes that are presented in Figure 8.1 are able to be discriminated. Areas of open water i.e. open leads, are marked in red, fast ice is marked in purple, the very thin drift ice is marked in green, thicker drift ice is marked in yellow and that area of the of the thicker drift ice that appeared to be textured, is marked in blue. The main characteristic of this image is that all regions seem to be highly localized.

This is in contrast to the segmentation results of the RS2 scene. Consider the results obtained for the RS2 5 class scene. This is shown below in Figure 8.9. As can be seen the segments that were derived for the most part are not localized. The land fast ice was found mainly to be a mixture of two classes, denoted by the blue and purple. The same is true for the thicker drift ice. This region seems to be a mixture of three classes marked in blue, green and purple. It should be noted that the area of the thicker drift ice, delineated in green, seems to share the same orientation as the yellow segment in the MODIS 5 class image, and the purple segment of the thicker drift ice in the RS2 image roughly corresponds to the area of the 5 class MODIS image that delineates the area with the roughness characteristic. More on this in the next section.

Despite these differences, it can be seen that both images clearly show the same regions that correspond to open leads and very thin drift ice. In the MODIS 5 class image, the open leads are shown in red and are highly distinct. In the RS2 5 class image, the open leads are shown in yellow/red. The very thin drift ice in the MODIS 5 class image is denoted in green. In the RS-2 image, this area is denoted mainly by the red and yellow.

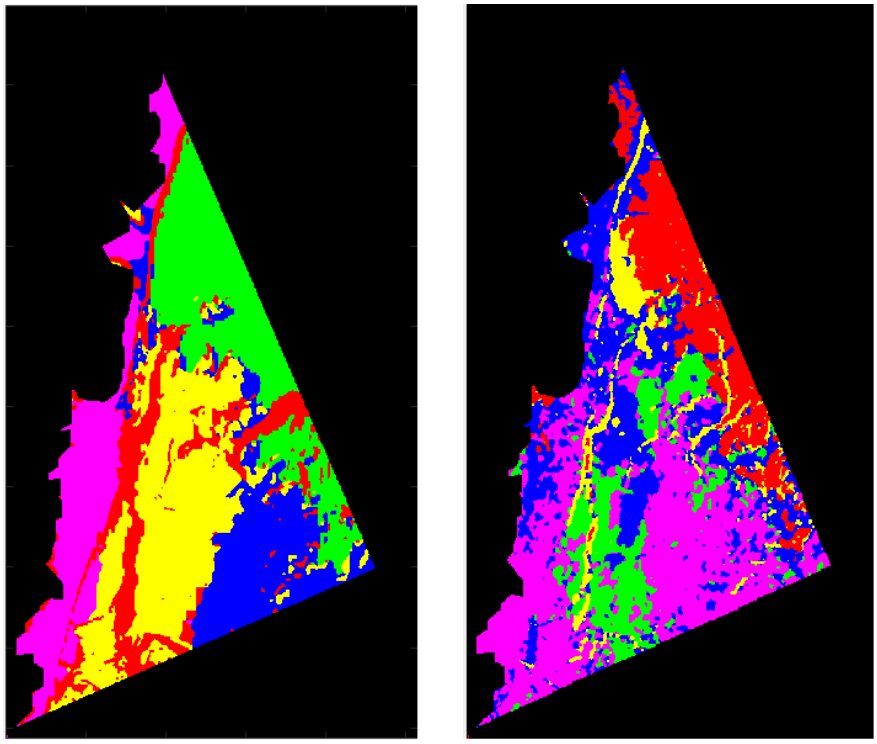

Figure 8.9: (Left) MODIS 5 class image. (Right) RS2 5 class image

It is hypothesized that the reason the thinnest ice types can be clearly distinguished in both images is due to the fundamental nature of both data types. MODIS is sensitive to thickness as explained in section 2.3.4. The different ice types shown in the MODIS 5 class image in Figure 8.9 can all be characterized by their thickness, which MODIS is sensitive to. RS2 is sensitive to the surface roughness of the material. In section 2.3.2 it is explained that we can ignore the dielectric effects on the backscattered radiation as the scene only contains high loss materials (open water, first year ice etc.). Thus open water will appear as a homogenous category as it is thought it will have the same degree of roughness throughout. According to the preliminary section, 8.1.1 the area of very thin ice is most probably grey ice, as it is thought this area contains a high proportion ice with thicknesses less than 20cm. This is explained in (Preußer, et al., 2015). According to the theory outlined in section 2.2.2 this type of ice is more likely to raft when force is applied to it, rather than forming ridges, thus keeping its relative smoothness.

8.1.3.1 Conclusion

The images above consider the case where data from both sensors are classified into a low number of clusters. It is assumed that the algorithm models and selects the largest, most distinct categories (or groups of categories) first and outputs them as a single cluster. As can be seen, open water and areas of very thin ice (probably less than 20 cm) can be clearly distinguished from both data sets. In this regard, the two sensor can provide similar information.

Differences occur when one considers the thicker ice types. In the RS2 5 class image in Figure 8.9 The purple class seems to be spread over both the landfast ice type and the drift ice. The interpretation here is that while MODIS can provide information on ice types locally, RS2 can provide information on the roughness of the ice which appears not to be confined to any particular ice category.

8.1.4 Case 2: Comparison between higher number of clusters

8.1.4.1 Description

There is a maximum number of clusters that could be achieved by each data set. For the MODIS data set, this was 90, while for the SAR data this was 26. Both of these images are shown below side by side in Figure 8.10. One possible reason for the disparate number of clusters that were achieved between both data types, is that for MODIS, we are segmenting data that represents 14 data bands, while for the RS2 data we are segmenting three generated features. Given that the three PCA bands, that were inputted into the segmentation algorithm, represent 99.05% of the variance (as shown in Table 8.2) of the original 14 bands, it is expected that we would be able to find groupings that are more distinct. However, it is clear that by looking at the MODIS image it is difficult to draw any meaningful insights from this image given the variety of clusters that were found.

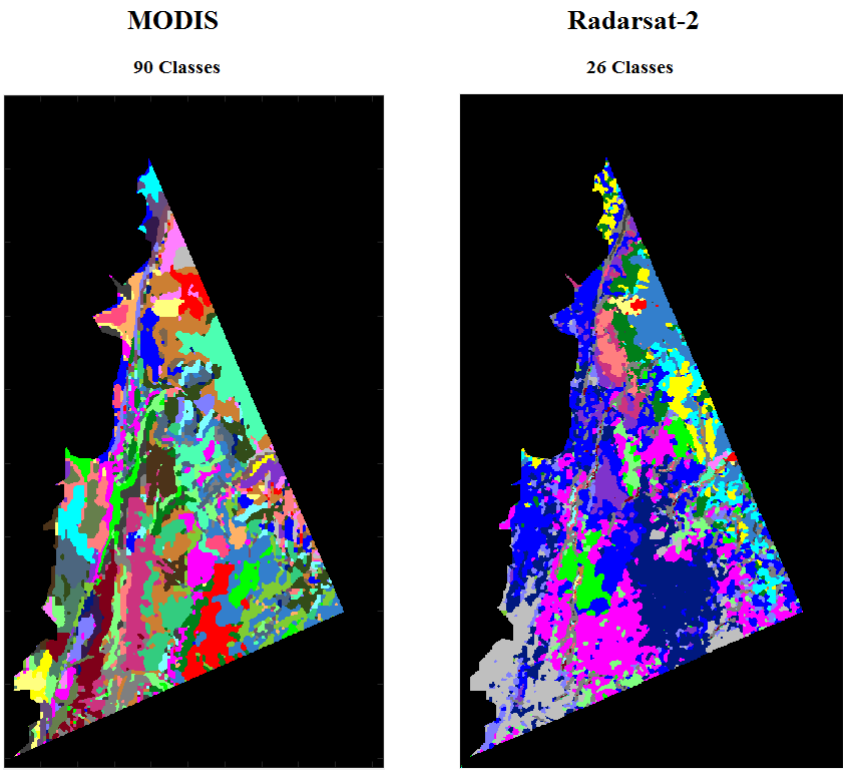

Figure 8.10: (Left) MODIS 90 class image. (Right) RS2 26 class image.

We can however look at the MODIS images for progressively higher number of clusters and try to determine if there are any general trends that can be drawn about the way the scene became segmented. Consider the MODIS images that were segmented to 10, 20, 30 and 40 classes shown below in Figure 8.11. The same can be done for RS2 images. Figure 8.12 shows the RS2 images segmented to 10, 15, 20 and 25 classes. Note; In the following discussion, a maximum of 40 classes were considered for the MODIS data as it is believed that segmenting the scene further would provide little additional information. It is easy to see why this is from inspecting the MODIS 90 class image shown above in Figure 8.10 (Left). We can see in this image the ice classes are difficult to interpret.

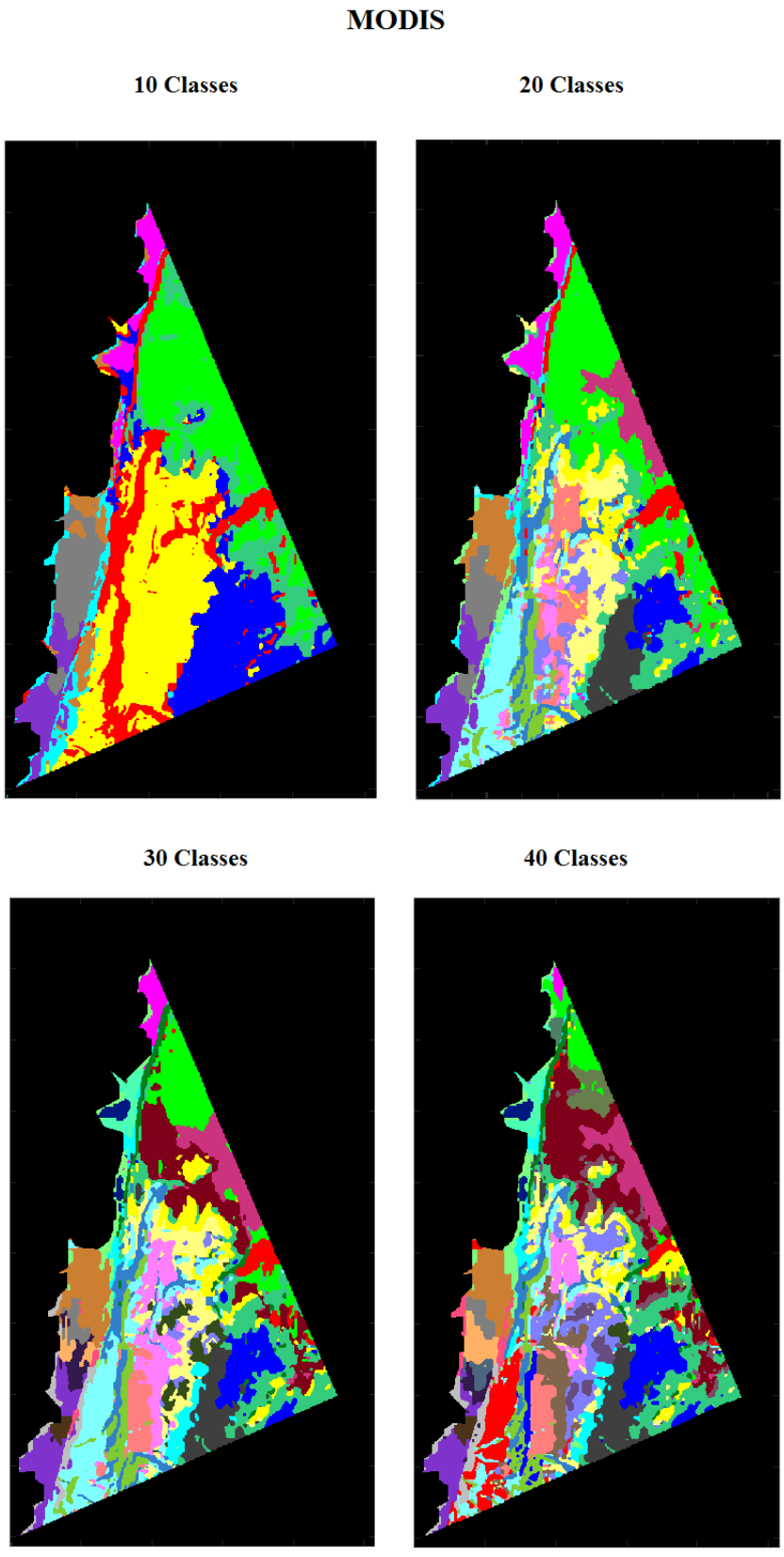

Figure 8.11: The MODIS scene segmented into 10, 20, 30 and 40 classes

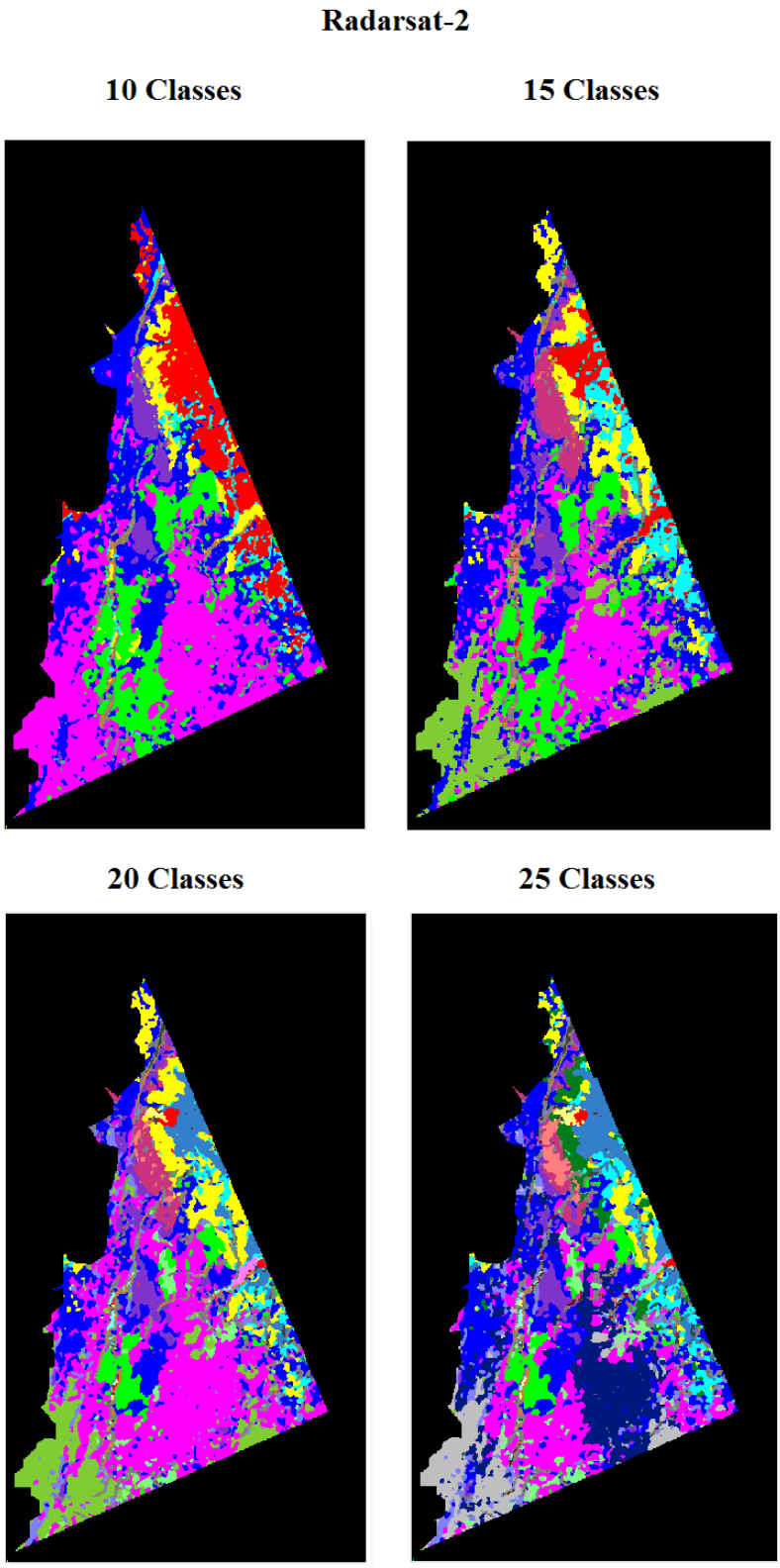

Figure 8.12: The RS2 scene segmented into 10, 15, 20 and 25 classes

8.1.4.2 Discussion

Similar to Case 1, when the MODIS data is segmented into progressively higher numbers of clusters the clusters are highly localized. This means that if a cluster is represented in one part of the image it is not represented in another part. This can be clearly seen in Figure 8.11 above. As can be seen for the 20 class case the landfast ice, the thin drift ice, the thicker drift ice and the textured drift ice are all visible as they are in the 5 class case in Figure 8.7. The difference here is that the landfast ice is more segmented as well as the thin drift ice. As clustering is further performed, these distinct categories of ice are further subdivided. This can be seen for the 20 class case where the thicker drift ice has been sub divided into many different categories. This is followed by the 30 and 40 class case where the thin drift ice is subdivided.

As in case one for the segmentation of the RS2 data, it cannot be said that the clusters that were found are highly localized. Figure 8.12 shows that with the exception of the open water leads and the very thin drift ice, the RS2 images do not appear to group the ice into localized categories. This is very apparent for example when the dark blue category that is seen clustered in the area where a lot of land fast ice is also represented in the area where there is a lot of drift ice above in Figure 8.12 for the 10 and 15 class case.

Despite this, there are some areas where similarities can be seen in both images. Consider the case of the MODIS 30 class image and the RS2 25 class image. This is shown below in Figure 8.13.

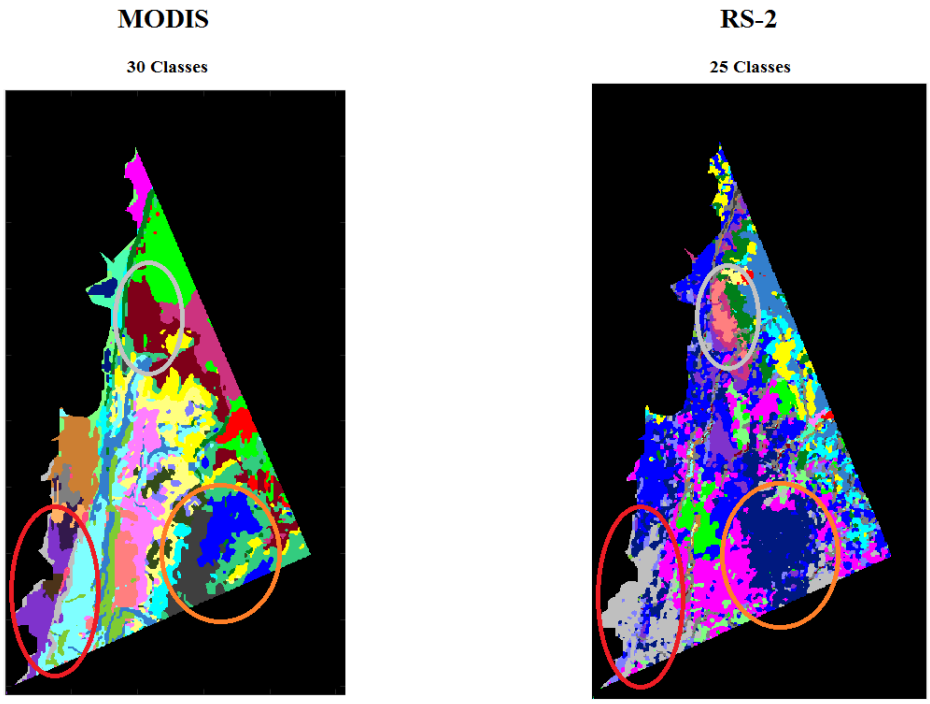

Figure 8.13: (Left) MODIS 30 class image. (Right) RS2 25 Class image. Areas of apparent similarity are marked with ovals in both images.

The area marked with the red oval corresponds to a section of landfast ice. This section is clearly defined in the MODIS 30 class image and is coloured purple. In the RS2 25 class image, this area is also seen and is coloured as grey. The difference between the two is that in the RS2 image a section of the drift ice is also classified as grey. If we examine this region, we see that there is a lead running between these two sections. This lead is also seen in the MODIS 30 class image. Examining Figure 8.1 in section 8.1.1

we can see its very probable that these two sections were joined at one stage, and so may share the same roughness characteristics.

The area marked with the orange oval corresponds to the region where the textured drift ice is. All though it is classified as two distinct classes in the MODIS 30 class image, it can be seen as one distinct class in the RS2 25 class image. It is interesting that this particular class does not appear in the RS2 10, 15 or 20 class image but instead appears after many other clusters have been found. The implication is that this region is not as rough as previously thought from examining the MODIS image in Figure 8.1.

The area marked with the grey oval corresponds to the area of very thin drift ice. This area seems to be represented in both images. The two sensor could be detecting the same region of open water here. In both data types, sections of the scene that represent open water seem to be able to be distinguished. This can be seen below in Figure 8.14. This image shows the MODIS scene segmented into 30 classes and the RS2 scene segmented into 15 classes. As can be seen, the sections that correspond to the areas where it is highly believed open water resides are apparent in both images.

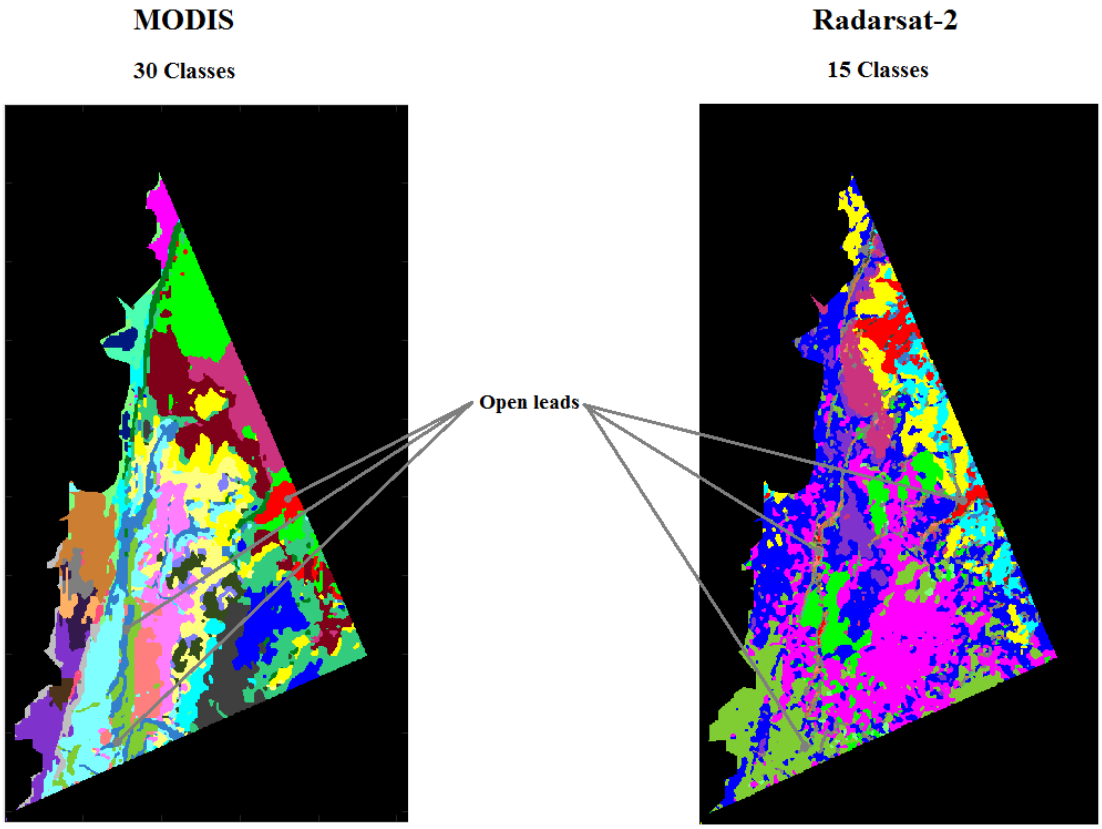

Figure 8.14: (Left) MODIS 30 class image, (Right) RS2 15 class image. Areas of open water, i.e. leads seem to be able to be distinguished in both images.

8.1.4.3 Conclusion

Like in case 1, open water seems to be easily distinguished from both data types. This is shown by the fact that both sensors are able to see open leads quite easily.

The area of landfast ice marked with a red oval in both images in Figure 8.13 is particularly interesting, given that these two classes look to be nearly identical in size, shape and location. It is postulated that both sensors are seeing an ice type that is simultaneously homogenous in both thickness and roughness for this particular case.

8.2 Comparison 2: May 12 (MODIS to RS2 Dual-Pol)

8.2.1 Preliminary

Like section 8.1.1 it is possible make some comments about the conditions in the Fjord before segmentation is performed. Consider the image shown in Figure 7.5. This image is shown again below in Figure 8.15. Based on the ice charts in Figure 7.5, it is possible to determine a few broad categories of ice type in this image. The landfast ice is clearly visible and can be seen attached to the land which is masked out in this image. Drift ice is also visible and is divided into two broad categories; the first being close drift ice with a concentration of 7/10 – 8/10, and the second being very close drift ice, with a concentration of 9/10 – 10/10. The difference between these two types of ice can be seen by how they differ in colour shades. Between the landfast ice and the drift ice, open water can be clearly seen.

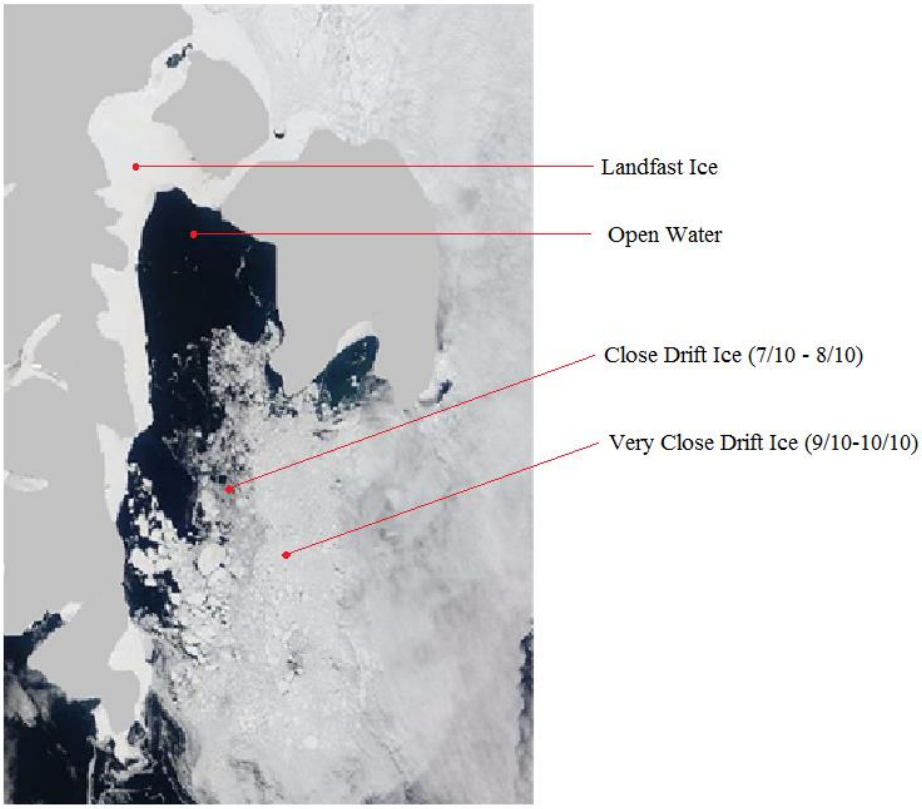

Figure 8.15: Storfjorden as on 12 May 2013. A few broad ice categories can be seen in this image including, landfast ice, open water and drift ice of two concentrations

8.2.2 Features Segmented

8.2.2.1 ScanSAR Features

Figure 8.16 below shows the three features that were generated from the ScanSAR Wide data. The top three panels show the features as they were generated for the entire scene. The bottom three panels show the three features but with the MODIS cloud mask applied. Note; these features were segmented after the land and cloud mask was applied. The MODIS land and cloud mask was applied to the SAR data to ensure that only the pixels in the MODIS data that were visible were compared to the corresponding pixels in the SAR data. As is the case for Comparison 1, inspecting the features visually it can be seen that the RK feature details the texture of the scene. The MRCS shows a clear distinction between the open water, the close drift ice and the very close drift ice. The Cross-pol Ratio seems to show a clear distinction between the open water and ice in general without showing much distinction between the different concentrations of drift ice.

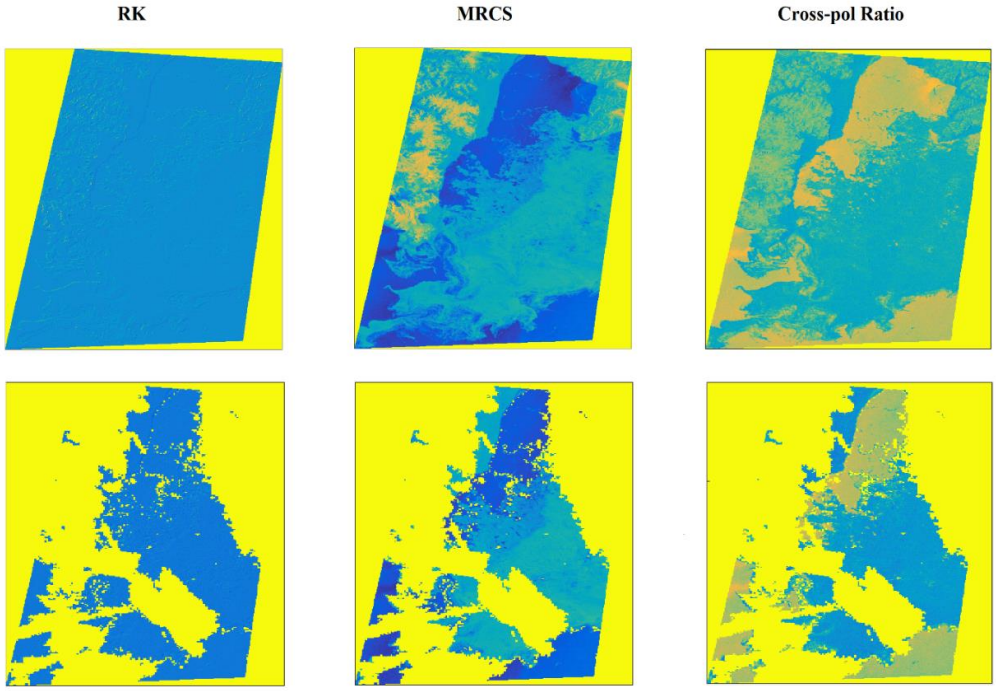

Figure 8.16: (TOP) ScanSAR Narrow features that were generated. (Bottom) The three features in the top row with the cloud mask applied.

8.2.2.1 MODIS Features (PCA image)

As in section 8.1.2.2, bands that were corrupted were identified and excluded after the preprocessing stage. Table 8.3 on the next page highlights the bands that were kept and the ones that were discarded. The bands that were kept were transformed into a new space via PCA. It was found that the first four PCs contributed the most variance to the new feature space so these were kept and used for segmentation. Figure 8.17 shows an RGB image made using the first three PCs. Figure 8.18 shows a bar graph showing, in percent, how much each component contributes to the variance. Table 8.4 displays both the cumulative percentages of the contributions from each component and the individual percentage contribution from each component. As can be seen from this table, the first four components contribute 81.83%, 9.89%, 3.77% and 2.06% of the variance respectively. Cumulatively, they contribute 97,56% of the variance.

Table 8.3: Bands that were kept and those that were discarded.

Band	Kept or Discarded
1 (250m)	Kept
2 (250m)	Kept
3 (500m)	Kept
4 (500m)	Kept
5 (500m)	Kept
6 (500m)	Discarded
7 (500m)	Kept
8 (1km)	Kept
9 (1km)	Kept
10 (1km)	Kept
11 (1km)	Discarded
12 (1km)	Discarded
13 (1km)	Kept
14 (1km)	Discarded
15 (1km)	Discarded
16 (1km)	Discarded
17 (1km)	Kept
18 (1km)	Kept
19 (1km)	Kept
20 (1km)	Kept
21 (1km)	Discarded
22 (1km)	Kept
23 (1km)	Discarded
24 (1km)	Discarded
25 (1km)	Discarded
26 (1km)	Discarded
27 (1km)	Discarded
28 (1km)	Discarded
29 (1km)	Discarded
30 (1km)	Discarded
31 (1km)	Kept
32 (1km)	Kept
33 (1km)	Kept
34 (1km)	Discarded
35 (1km)	Discarded
36 (1km)	Discarded

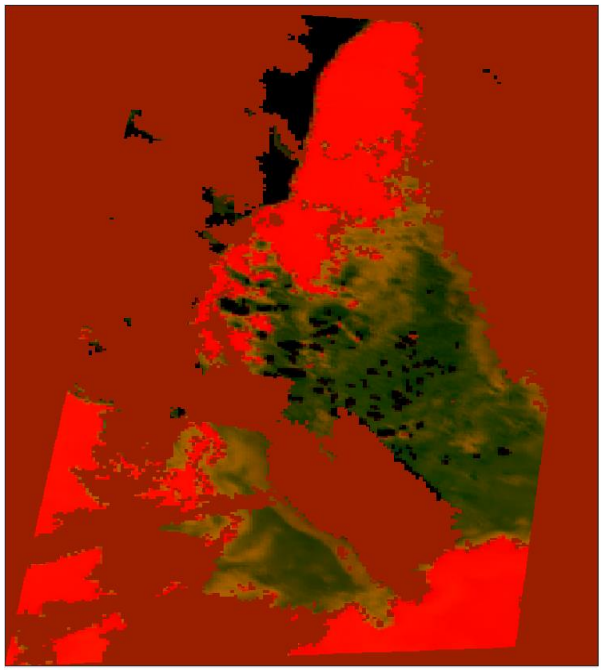

Figure 8.17: PCA image made from the first 3 PCs

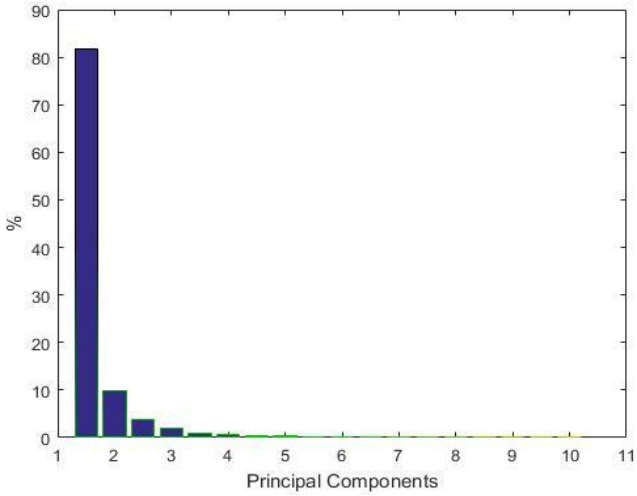

Figure 8.18: Bar graph showing the amount of variance contained within each principal component.

Table 8.4: Top row: Cumulative percentage variance contributed to each component. Bottom row: individual percentage contributed to each component.

1st	2nd	3rd	4th	5th	6th	7th	8th	9th
81,83	91,73	95,50	97,56	98,52	99,17	99,46	99,73	99,85
81,83	9,89	3,77	2,06	0,97	0,64	0,29	0,27	0,13

10th	11th	12th	13th	14th	15th	16th	17th	18th
99,93	99,98	99,988	99,992	99,995	99,997	99,998	99,999	100
0,07	0,05	0,007	0,004	0,003	0,002	0,0016	0,0014	0,00019

8.2.3 Case 1: Comparison between low number of clusters

8.2.3.1 Description

For MODIS, 3, 4 and 5 were determined to be the best number of clusters for displaying the major ice types in the fjord. For RS2 2, 3 and 4 were determined to be the best number of clusters for displaying the major ice types in the fjord. Once again, the decision to stop at these number of clusters was reached by segmenting the scene beyond these numbers of clusters and observing that the major ice types that are known to present in the fjord, at this time appeared to be segmented further. Figure 8.19 below shows the image for these segmentations. Note; the MODIS 2 class case is excluded as the segmentation result did not distinguish between the open water and the drift ice.

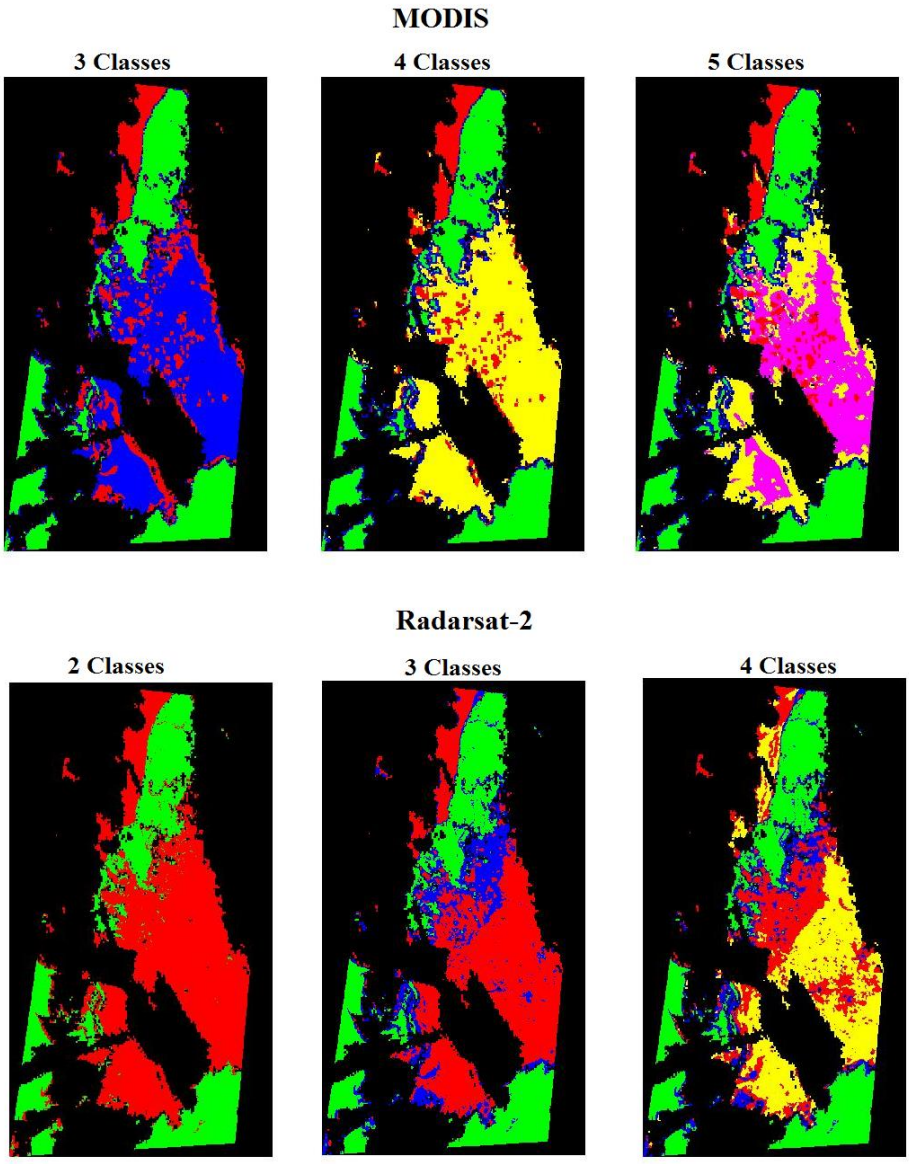

Figure 8.19: (Top) MODIS segmentation results for 3, 4, and 5 clusters. (Bottom) RS2 segmentation results for 2, 3 and 4 clusters.

8.2.3.2 Discussion

Looking at the results in Figure 8.19 it can be seen that both RS2 and MODIS are able to clearly distinguish areas where ice is present and areas where open water is present. The areas of open water are all shown in green. This is a particularly interesting result, as being able to distinguish areas that are navigable for ships is of immense importance. Just examining the images above visually, it appears that the areas showing open water are equivalent, i.e. an area of open water detected in the segmented image of one sensor directly corresponds to an area of open water detected in the segmented image of the other sensor.

It can also be seen that MODIS makes a distinction between the landfast ice and drift ice early in the segmentation process. All the MODIS segmentation images in Figure 8.19 show landfast ice marked in red with very little of this class being represented in the drift ice. RS2 however shows little distinction between the landfast ice and the drift ice. This can be seen in the 4 class segmentation image. In this image, the landfast ice is shown in red and yellow, which is also the colour the drift ice is represented as.

The RS2 images are able to segment the drift ice into two distinct categories. This can be seen in the 3 and 4 class images in Figure 8.19 above. The 4 class image seems to be in direct agreement with the ice concentration chart seen in Figure 7.9 made for 12 May 2013 and the MODIS true colour image shown in Figure 8.15. While this image shows two distinct categories delineating areas of different concentrations of drift ice, the MODIS 5 class image does not seem to make the same distinction. One possible reason for this discrepancy is that the ice concentration is a measure of how tightly packed an ice flow is. If the SAR observes an ice floe that is tightly packed it will appear rougher than a region that is less densely packed as the increased concentration of ice gives greater opportunity for deformation. This can be used to give some measure on the ice concentration. Looking at the MODIS images in Figure 8.19, it is clear the MODIS isn't as sensitive to the concentration of the ice floe as one would expect. This could be a result of the MRF smoothing that was performed on these classified images.

Consider the 3 images shown below in Figure 8.20. The centre image shows the same MODIS true colour image shown in Figure 7.9 (Note; this image is not georeferenced). The image to the left shows the MODIS 5 class image from Figure 8.19 and the image to the right shows the RS2 4 class image from Figure 8.19. The orange oval in the centre image shows the boundary between regions that contain drift ice with concentration of 7/10-8/10 and 9/10-10/10. This boundary can be seen in both the MODIS and RS2 images and is denoted by a corresponding orange oval. This indicates that both sensors are detecting a boundary here.

Now consider the light blue oval in the centre image. This region of the drift ice shows pieces of ice that are very large in size. This is demonstrated in Figure 8.21 below. In this image, the MODIS 250m band 1 is shown. The largest piece of drift ice is highlighted. As can be seen in the zoomed in portion, the length along the highlighted strip of pixels is 8000m showing that the pieces of ice in the light blue oval are on the scale of kilometres. It is interesting to note that MODIS makes no distinction between the very concentrated drift ice, which is what you would expect, as large, solid pieces of ice are by definition, very concentrated areas of ice. The RS2 however sees these large pieces as being more similar to the less concentrated area of drift ice. The reason for this is unclear at the present time.

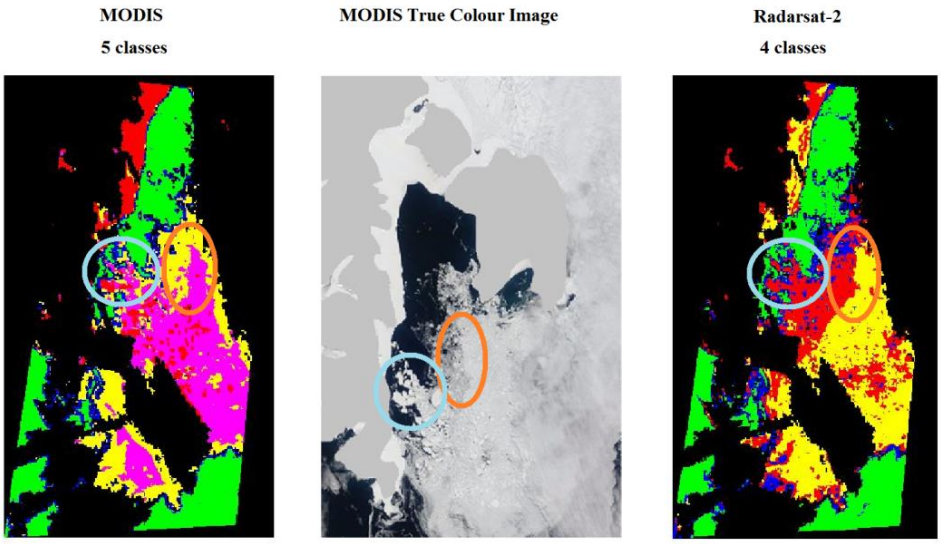

Figure 8.20: (Left) MODIS 5 class image. (Middle) MODIS true colour image. (Right) RS2 4 class image. Similar regions are marked by both the orange and blue ovals.

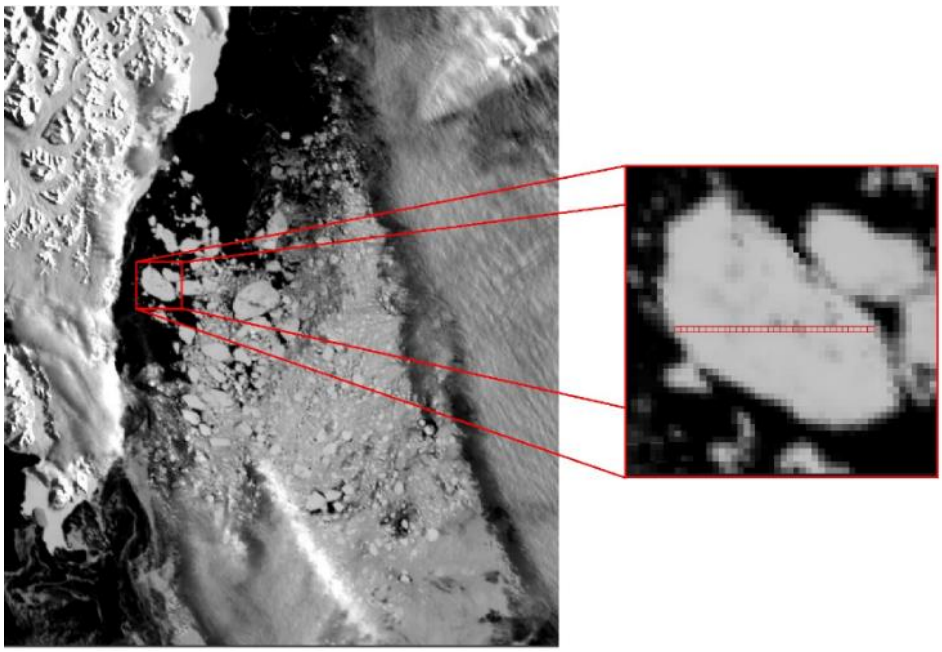

Figure 8.21: Zoomed in portion of a large piece of drift ice observed in the ice floe. Counting the pixels that are marked in red, this piece of ice is determined to be about 8 km in width.

It should be noted that the MODIS scene seems to show some anomalous behaviour concerning the cloud mask. Consider the case of the 3 class and 5 class MODIS image, both shown below in Figure 8.22. A distinct class is seen skirting area on the edge of the cloud mask in both images. As this cloud mask was taken from the MODIS MYD29 data product there is a high degree of confidence in this cloud mask. However, (Hall, et al., 2004) outlines that cloud masks that are generated in times of low illumination tend to be less accurate than those generated during mid-day. As this observation was made at 04.15, this could be an inaccuracy in the cloud mask and the segmentation algorithm is seeing a small region of cloud cover as a distinct ice type. Another possible reason for this anomalous effect is that these observations were made early in the morning and these could be the shadows of the clouds projected onto the ground. This is probable, as this effect appears to occur primarily on the left sides of the cloud mask. As the sun rises in the East, which would be the right side of the images below, the clouds shadow could be getting projected onto the ground.

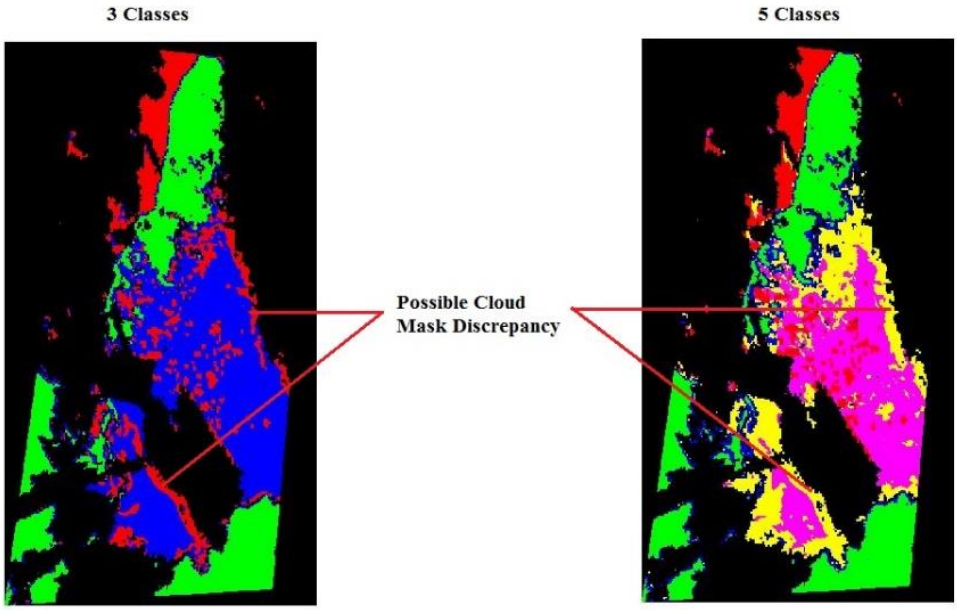

Figure 8.22: MODIS 3 and 5 class image. An area of anomalous cloud mask behaviour is observed.

8.2.3.3 Conclusion

As is the case for the March 21observation, the two sensors seem to be able to distinguish between open water and sea ice in general quite well. However, for the March 21 observation the 'open water' could have been a combination of water and new ice as the only open sections in the ice were leads. In the case for May 12, open water is clearly shown and accounts for a vast portion of the image. In all segmented images the open water is clearly segmented as by both sensors.

It seems that MODIS and RS2 appear to be able to segment between areas of concentrated and less concentrated ice floes. This is evidenced by the detection of the edge between the less concentrated ice region and the more concentrated ice region in Figure 8.20 denoted by the orange oval. However, the presence of the large ice pieces, shown in Figure 8.21, seem to alter the segmentation results. As a result, MODIS identifies these large ice pieces as concentrated areas of ice but RS2 does not.

8.2.4 Case 2: Comparison between higher number of clusters

8.2.4.1 Description

The maximum number of classes that were able to be achieved from the MODIS PCA features in this case was about 100 while the maximum number of classes achieved from RS2 was 10. Once again, there is a large disparity between these two numbers. As already explained in section 8.1.4.1 it is believed that this disparity is due to the large amount of variance that is captured by the MODIS input bands, 4 in this case, that capture 97,56% of the variance of 18 bands. The MODIS 10, 20 30 and 40 class image are shown below in figure 8.22. The RS2 segmented images for the 5 to 10 class case is shown below in Figure 8.23.

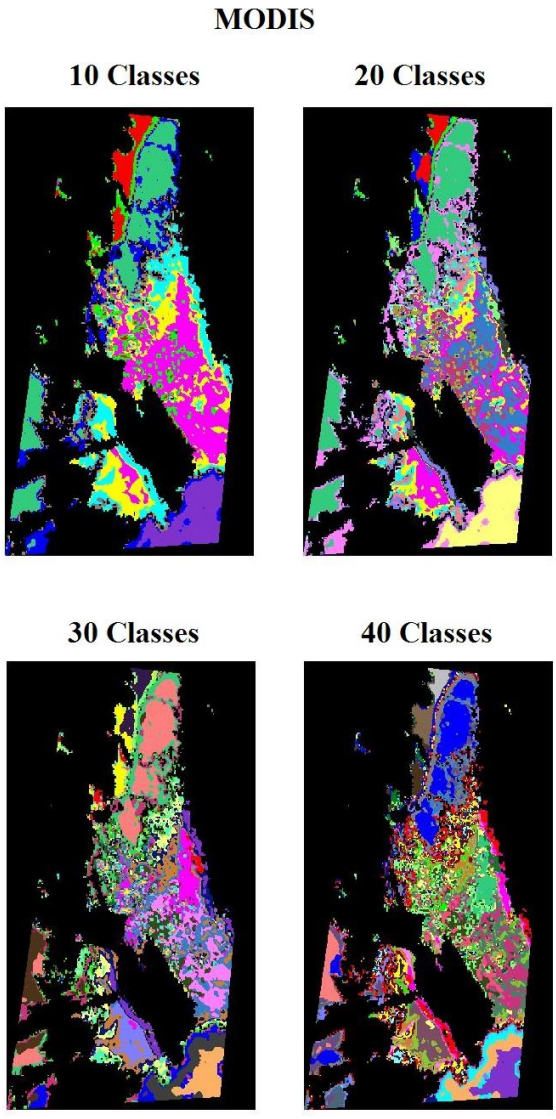

Figure 8.22: MODIS 10, 20, 30 and 40 class segmented images.

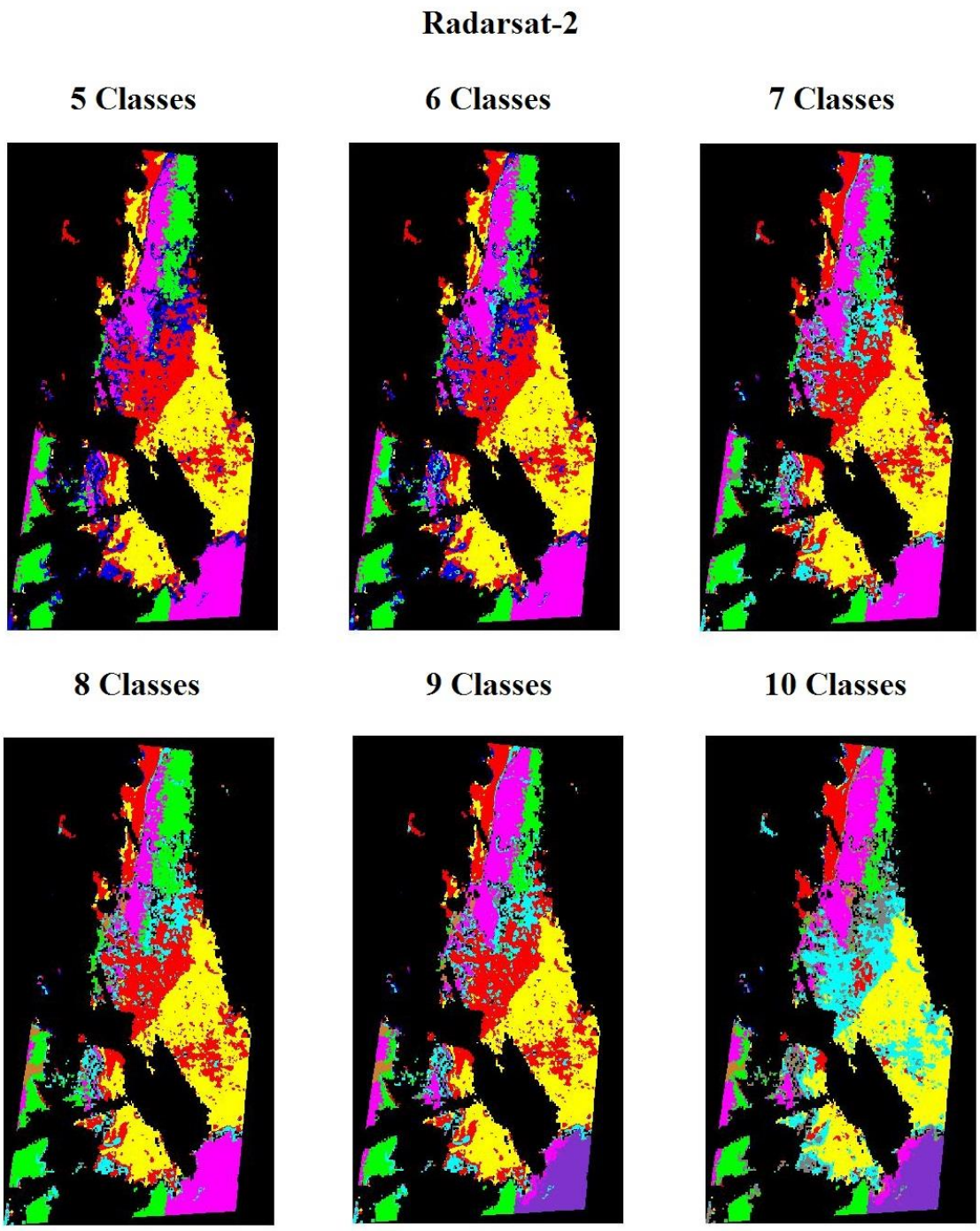

Figure 8.23: RS2 segmented images for the 5 to 10 class case.

8.2.4.2 Discussion

The first thing to be noted about the segmented images for the RS2 data, shown above in Figure 8.23, is that there is little variation between successive segmented images. The images for the 5 and 6 class results are very similar to each other and the results for the 7, 8 and 9 classes are also similar to each other. The differences between successive images is almost imperceptible. For this reason, all comparisons will be done between the MODIS segmentation results and the 10 class RS2 segmented image as it is thought this constitutes a representative RS2 segmented image.

The second thing to note about the segmented images for the RS2 data is that the banding effect that was explained in section 8.1.2.3 appears to be visible. This is shown below in Figure 8.24 for a 10 class image. Shown in Figure 8.25 is the original HV RS2 image. In this image, the banding effect is clearly visible. As already stated in section 8.1.2.3 the removal of this effect is beyond the scope of this study, but as can be seen, it has a visible effect on the final results, primarily over water.

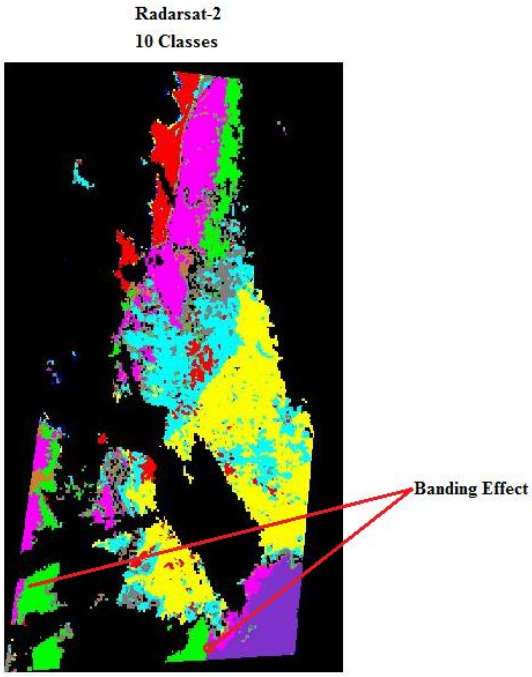

Figure 8.24: A possible banding effect is visible.

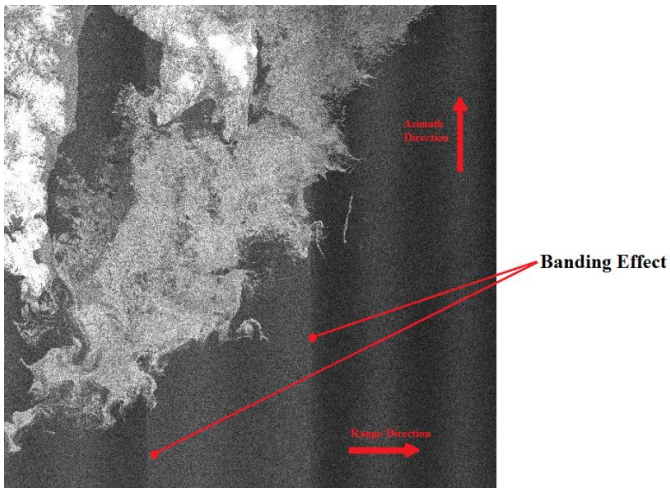

Figure 8.25: Banding effect as seen in the original HV RS2 band.

Similar to Comparison 1, the results for the segmentation of the MODIS images are all are highly localized. This can be seen in Figure 8.22. In contrast to Comparison 1 however, the RS2 segmentations results are also highly localized and the results of the segmentation are restricted to the particular ice type. This can be seen above in Figure 8.23. In this figure, all the landfast ice is red, the concentrated drift ice is primarily yellow and the less concentrated drift ice is coloured blue and grey.

In terms of comparing the segmentation results from MODIS and RS2, consider the image shown in Figure 8.26 below. This image shows 4 of the MODIS images segmented into 10, 20, 30 and 40 classes. Next to this is the RS2 10 Class image.

The area bounded by the blue oval in Figure 8.26 shows the land fast ice in the scene. In the MODIS 10 class image this ice type is designated as one class, in the 20 and 30 class images this is type is designated as 2 classes and in the 40 class image, this ice type is designated as 3 classes. This shows that the segmentation algorithm identified variations in this ice type. The corresponding blue oval in the RS2 image shows that the land fast ice here has been identified as one class. Thus, it can be seen that the SAR sees this as one ice category while MODIS is seeing this as three ice types, according to the 40 class image.

The area bounded by the red oval in Figure 8.26 below shows the same boundary between the concentrated drift ice and the less concentrated drift ice as displayed in Figure 8.20 from the previous section. This boundary region is apparent in all the MODIS images and in the RS2 image.

The area bounded by the orange oval shows, what is believed to be another boundary between ice of two different concentrations. It is believed that this is a boundary between two different ice regions and not ice and water as the MODIS segmentation results from the previous section showed this area to contain only sea ice and not water. As can be seen, this boundary appears to have the same shape in both the MODIS images and the RS2 images.

Note, In the 10 class segmentation image for RS2. The landfast ice has been segmented as one class rather than 2 classes, as it was for 2-6 classes.

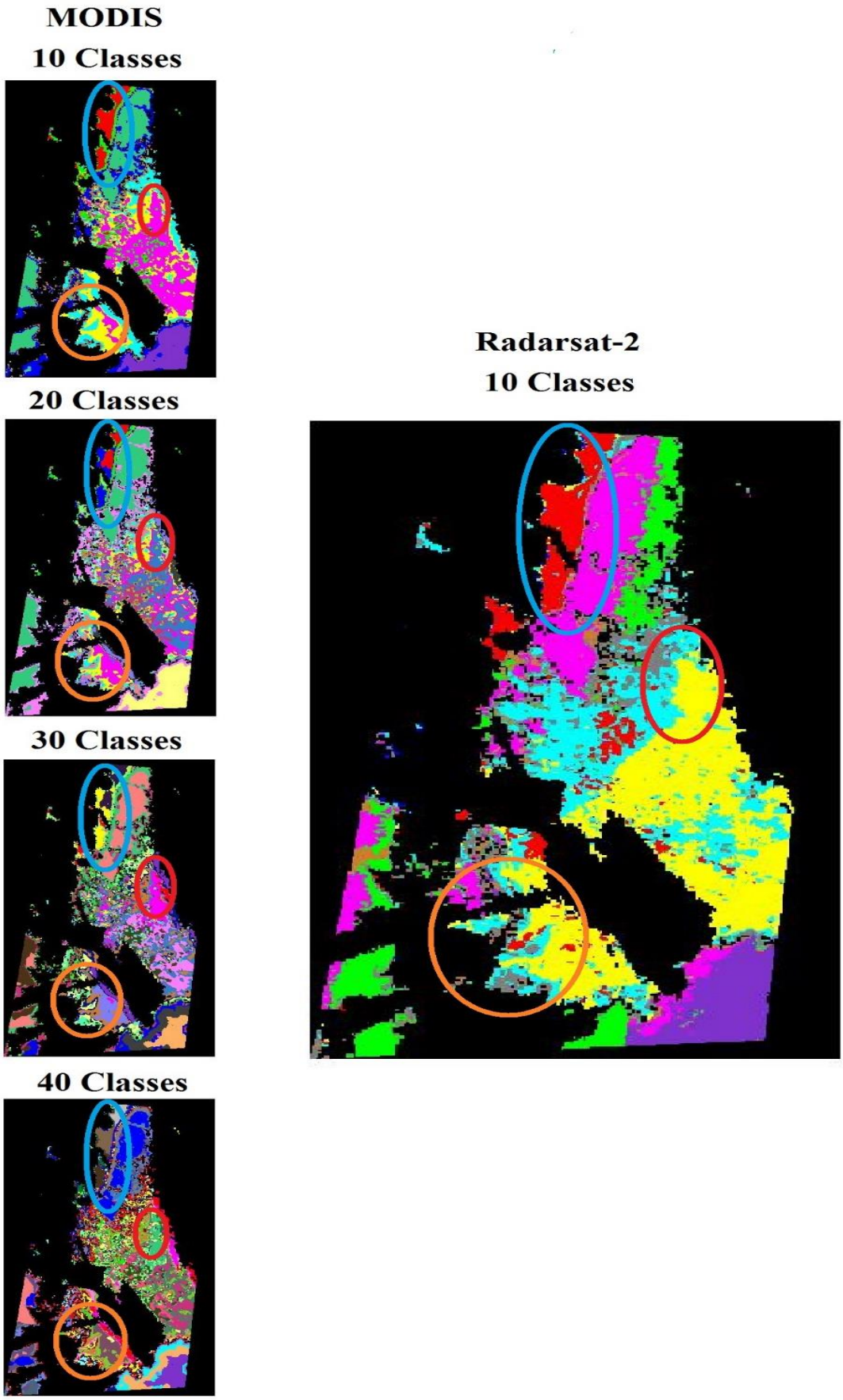

Figure 8.26: (Left) MODIS 10, 20, 30 and 40 class segmentation images. (Right) RS2 10 class segmentation image.

8.2.4.3 Conclusion

For this case, the MODIS and RS2 showed high agreement between identifying boundaries within the drift ice. This is evidenced by the area displayed by the red and orange ovals in Figure 8.26. This is a particularly interesting result as both sensors are displaying common information about the ice present in the scene. If one ignores the banding effects over water in the RS2 image in Figure 8.26, then it can be seen that, not only are both sensors identifying the same areas of water and ice, but are also identifying roughly the same types of ice. This is especially true if you compare the MODIS 30 class image with the RS2 10 class image in Figure 8.26. Both sensors for this case are seeing one class for the landfast ice, they are both distinguishing between the concentrated drift ice and the less concentrated drift ice and as can be seen the shape of the ice floe is also similar in both images.

If one compares the MODIS 40 class image with the RS2 10 class image, we see that more detail can be seen. Given the high level of agreement between the MODIS 30 class image and the RS2 10 class image, it can be reasoned that the 40 class image is now providing suplemental information on the conditions of the ice present in the scene. This is especially true if one considers the landfast ice which has gone from being one class in the MODIS 30 class image to 3 classes in the MODIS 40 class image.

8.3 Comparison 3: May10/12 (MODIS to RS2 QuadPol)

8.3.1 Preliminary

This comparison is between the RS2 QuadPol data that was taken on 10 May 2013 and the MODIS PCA bands that were taken 2 days later on 12 May 2013 over the same geographic region that the QuadPol data was acquired. These MODIS PCA bands are the same ones that are used in Comparison 2. This geographic region is shown below in Figure 8.27.

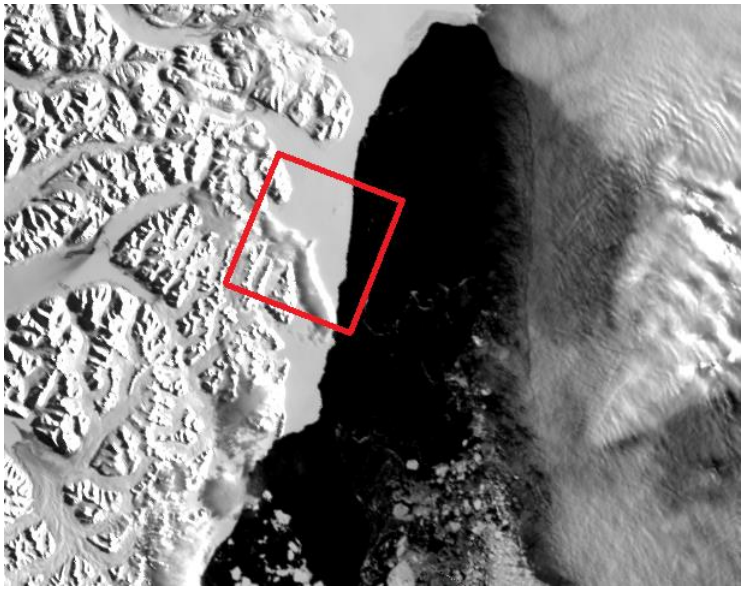

Figure 8.27: MODIS red band image taken 12 May. The red square shows the footprint of the QuadPol data set. As can be seen in this image, a cloud obscures much of the QuadPol scene.

Before a comparison is made, a few things that should be noted. The first is that the observations of the two data sets is 2 days apart. Given that Storfjorden is a highly dynamic fjord and that temperatures above zero were measured over the two days in between the observations (this is shown in section 7.1.1) it is possible that the conditions of the ice present could have changed in between the observation times. The second thing to note, is that the swath width of the QuadPol scene is only 25km and MODIS has pixel spacing's of 250m. This implies that this swath is equivalent to only a small portion of the MODIS scene, approximately only 100 x 100 pixels in size. Adding to this is the fact that nearly half of the scene is obscured by either cloud or occupied by land so the portion of the scene available for comparison decreases.

8.3.2 Description and discussion

Shown below in Figure 8.28 is the segmentation results for the portion of the MODIS PCA bands that correspond to the swath of the QuadPol data. As can be seen, these images are able to be segmented into many classes. Shown below in Figure 8.28, this small scene was able to be segmented into 30 classes. Note; the segmentation was stopped at 30 classes because given the size of the scene and the coarseness of the data, any further segmentations would have been uninterpretable. The most notable thing about the nine images in Figure 8.28 is that they show a very clear distinction between the sea ice and the open water. For reference, the water in the 4 class image is marked in green with the ice mostly marked in yellow for example. All the ice in this scene is landfast ice. Given that many classes were able to be derived, it could be argued that these ice types must have had different optical properties, on the scale of tens of kilometres, that allowed them to be segmented like this. However, the low number of individual pixels that were available for segmentation could also be a source of error.

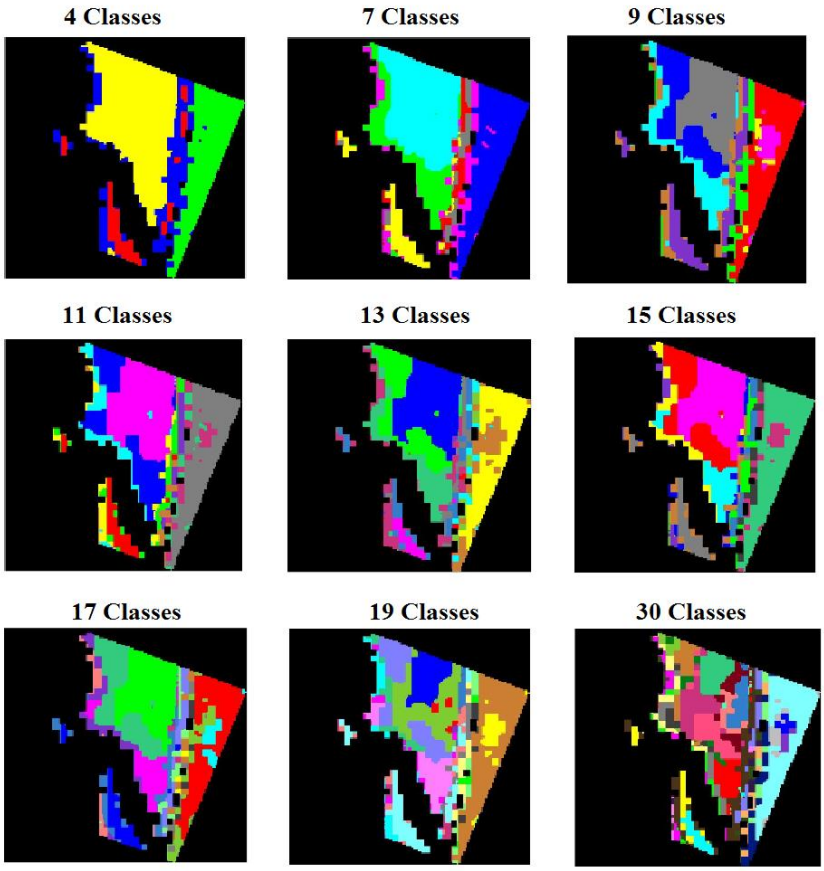

Figure 8.28: MODIS PCA features that correspond to the footprint of the RS2 QuadPol data. The black regions indicate a cloud/land mask.

The RS2 QuadPol image shown below in Figure 8.29 was segmented into 13 classes using the 6 features outlined in section 7.3.10. 13 classes was the maximum number of classes the segmentation algorithm found. Note, at the time of writing it was not possible to georeference the segmented image and apply the cloud mask.

As can be seen in this image, open water is clearly distinguished by the green and pink areas. The ice seems to be composed of 3 main surface classes, those being yellow, purple and brown. Examining the

images in Figure 8.28 however, it is difficult to see any similarities between the segmented MODIS images and the segmented QuadPol images aside from the two being able to distinguish ice in general and open water.

The most striking thing about the segmented RS2 QuadPol image shown in Figure 8.29 is that it is able to provide a lot of detail about the ice surface. In the image shown in Figure 8.29, individual features such as 'cracks' or ridges are seen on the ice, coloured in blue. These types of features are impossible to be retrieved from MODIS imagery as the resolution of this sensor is far too coarse.

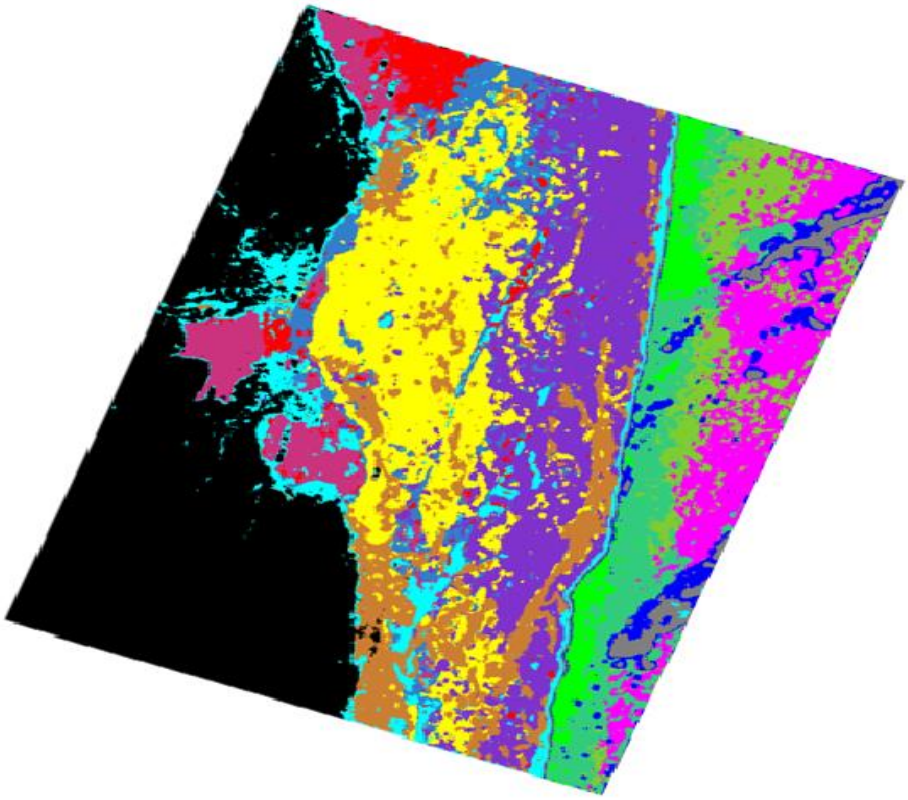

Figure 8.29: RS2 QuadPol image, segmented into 13 classes. Shown in black is a primitive land mask. The open water can be seen in green and purple. The landfast ice is composed mainly of 3 surface types coloured, yellow, purple and brown.

8.3.3 Conclusion

The benefits that can be gained from data acquired in SAR QuadPol mode are numerous. The spatial resolution in QuadPol mode is higher, allowing for greater surface detail to be achieved. There is the possibility of using data that is in 4 polarimetric channels, as opposed to 2 in dual-pol, which allows for the greater retrieval of information. The drawback to using data acquired in this mode is that its spatial extent is limited. As can be seen from the images in Figures 8.28 and 8.29, RS2 QuadPol mode is suitable when a high degree of information is required about a confined area. MODIS is better suited for monitoring areas that are many hundreds of kilometres in extent.

8.4 Comparison 4: Comparison between HEM ice thickness and HEM derived ice roughness

8.4.1 Preliminary

The following discussion is designed to determine if a relationship between the thickness of the sea ice, as measured by the HEM on 11 May 2013, and the derived ice roughness can be seen. The roughness is derived from the laser altimeter data that accompanies the thickness measurements and was determined by calculating the r.m.s. of the helicopter height value over a certain number of data points. According to (Peterson, et al., 2008) these two aspects of sea ice, i.e. roughness and thickness, are expected to be closely related due to the theory of isostasy. In the simplest terms, isostasy is the principle of buoyancy where an object that is suspended in a fluid is buoyed with an opposing force that is equal to the weight of the fluid that was displaced. (Geiger, et al., 2015) describes sea-ice isostasy as a vertical buoyancy balance, in that a mass per unit volume of seawater is supporting a mass per unit volume the overlying sea ice and snow. The relationship between thickness and roughness is also elaborated by (Sandvin, et al., 2006) who stated that in general, as ice grows and becomes thicker, it can become rougher for a variety of reasons, including exposure to the elements and interactions with other ice floes

The tracks of the HEM are shown below in Figure 8.30. This image shows the ScanSAR Wide MRCS feature that was derived for the 12 May measurement, with the HEM tracks, marked in red. As can be seen in this image, the measurements were made primarily over the area of the fjord that contained land fast ice.

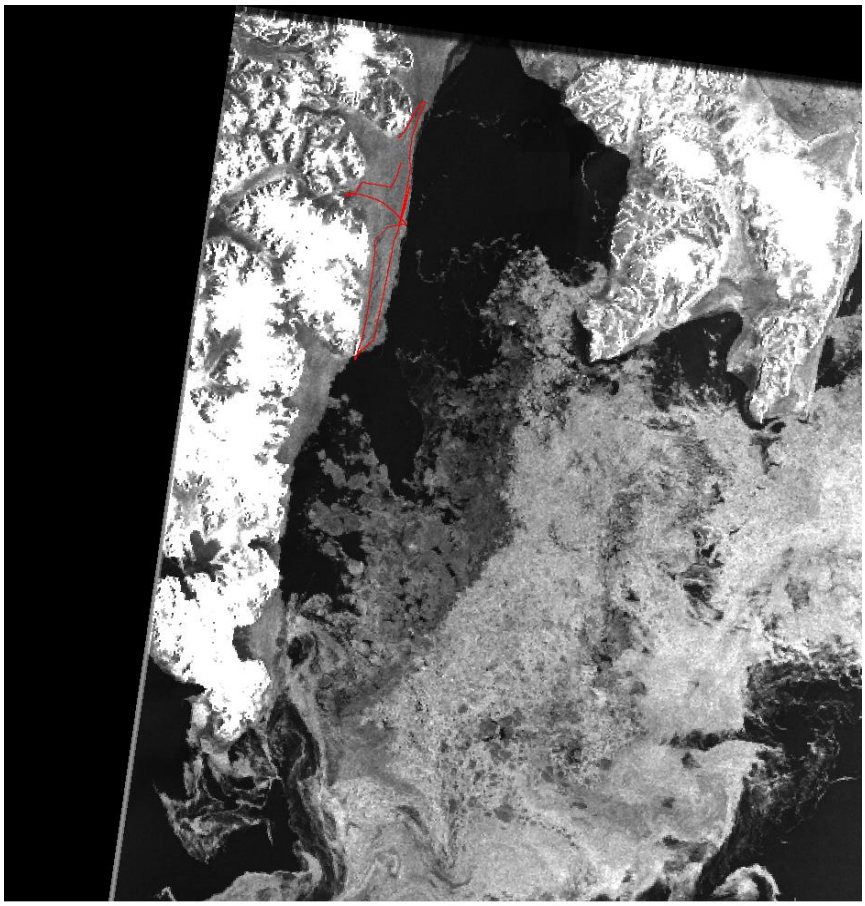

Figure 8.30: MRCS feature image for 12 May measurement. The HEM data track are shown in red.

It should be noted that when dealing with HEM data, the helicopter that took the measurements is not guaranteed to be flying at a level trajectory with respect to sea level. As a result, the height measurements between the helicopter and the sea ice-atmosphere interface very likely contain variations due to the helicopters flight deviations. The removal of these height variations has been studied since the 70's. A notable study was conducted by (Hibler III, 1972) who showed that it is possible to remove these variations by subjecting the initial height profile to a series of high and low-pass filters.

However, as this was beyond the scope of this study, it was chosen to derive the roughness without removing the helicopter variation, and calculating the r.m.s. of the measured height values over a sliding window of suitable size. As it is believed that the altitude of the helicopter did not vary drastically, the resulting profile would have low-frequency altitude variations. By choosing a sliding window of small enough size and calculating the r.m.s. value from this sliding window, it is believed that the variations due to the ice surface characteristics would be captured only.

The entire HEM ice thickness data set is shown below in Figure 8.31. As can be seen in the graphs below, there are regions where the HEM did not take measurements. These are denoted by the gaps in the data sets. Also can be seen are three large 'humps'. These humps seem to correspond to the area where no ice thickness measurements were made. It is not known exactly what these humps represent but it is thought they are either regions where the helicopter climbed to pass over areas of land, or where they climbed to an altitude in order to calibrate the EM bird. In the following analysis only the areas that are between the two vertical, red, dashed lines in Figure 8.31 are considered. This portion of the data is shown below in Figure 8.32. The helicopter track that corresponds to this portion of the graph is shown below in Figure 8.33.

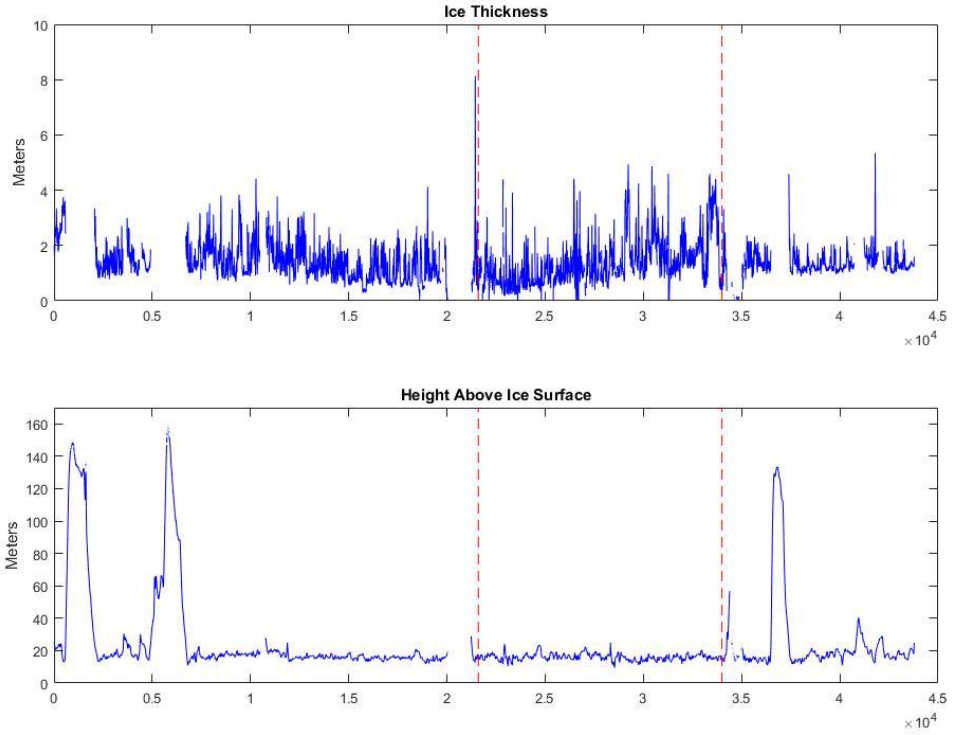

Figure 8.31: (Top) HEM ice thickness data as measured by the EM bird, (Bottom) Laser altimeter measurements from the EM bird. The two vertical, red dashed lines show the portion of the data that will only be considered in this analysis.

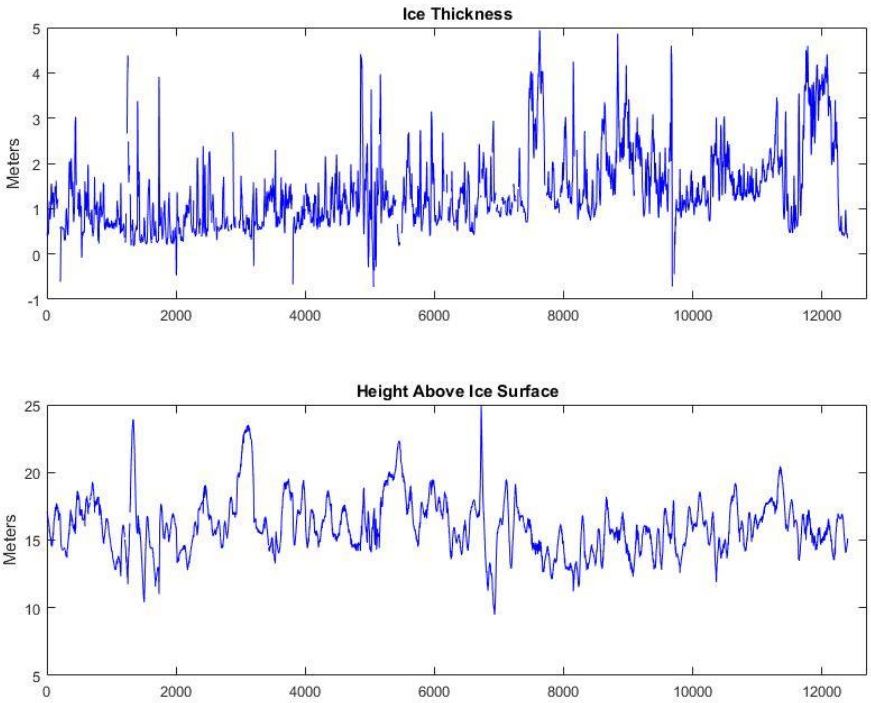

Figure 8.32: HEM ice thickness measurements and the laser altimeter measurements that are displayed between the two vertical, red dashed lines in the previous image.

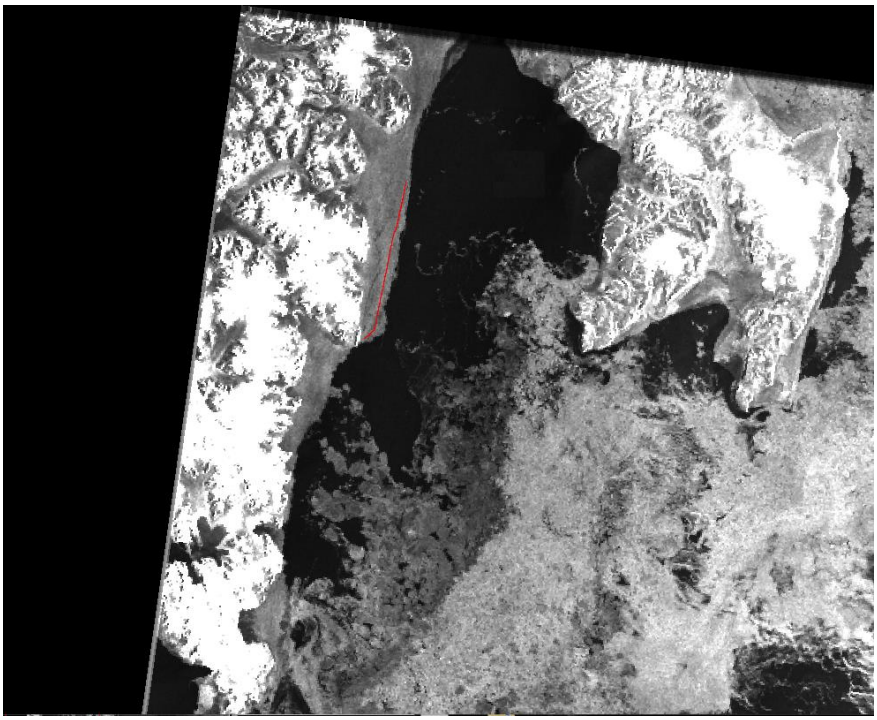

Figure 8.33: The data track on the landfast ice that corresponds to the selected region of data in Figure 8.31.

The size of the window chosen was 20 points. As each measurement was taken in intervals of 4.5 meters approximately this 20-point sliding window amounts to roughly 90 meters. The derived roughness and the ice thickness are shown below in Figure 8.34.

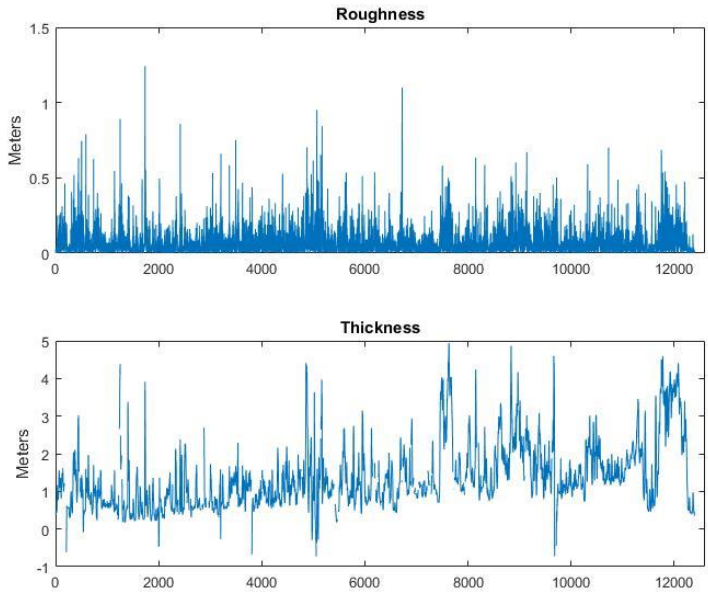

Figure 8.34: The roughness characteristic that was derived from the HEM laser altimeter measurements and the corresponding ice thickness measurements.

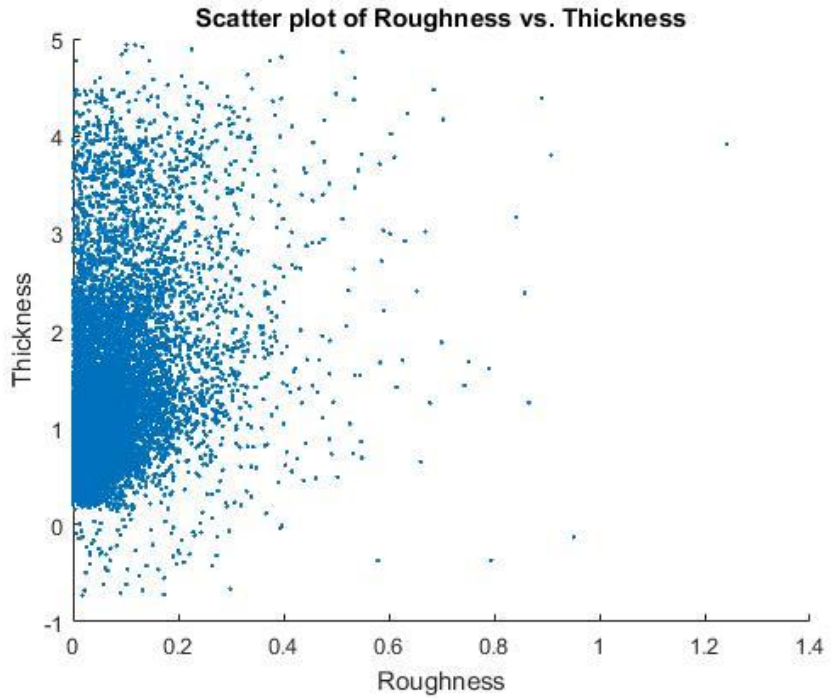

Figure 8.35: A scatter plot of the data points displayed in the previous image. As can be seen it appears this swath of landfast ice has a thickness range of several meters, while the roughnes has a range of roughly 1 meter.

8.4.2 Discussion and Conclusion

As can be seen from Figure 8.35 above, there appears to be some relationship between the derived roughness and the thickness of the ice. It is important to remember that the ice that was under investigation is all landfast ice and is attached to the shore. This ice is highly static and the portion of the data showed above represents a swath of ice running parallel to the shore and slightly in from the ice edge. The expectation is that, this ice, which is not rafting and so not interacting with other ice in an ice floe, will be relatively smooth. Also, given that there may be snow cover on the ice and that temperatures greater than 0^0 *C* were recorded at Longyearbyen airport and on Hopen Island the day before (see the atmospheric weather charts in section 7.1.1) the roughness of the ice, in this case, may have been altered and not as representative of ice the roughness of landfast ice that is newly forming for example.

Despite this, the graph in Figure 8.35 seems to suggest that the landfast ice present in the Storfjorden at this time is relatively smooth, but its thickness values have a larger dynamic range, roughly 0 to 4.5m in this case. It is interesting to note the comparison between the landfast ice in Figure 8.26. This is shown below again in Figure 8.36 for the MODIS 40 class case and the RS2 10 class case for the portion of the scene that contains the landfast ice zoomed in. The position of the helicopter track is approximately shown as a grey line. As can be seen the HEM track in the MODIS image crosses two major classes denoted by the dark brown and the light brown. The HEM track in the RS2 image covers only one major class, denoted in red. Looking at the thickness measurements in Figure 8.34 (Bottom) it is easy to see that there is an upwards trend in values going from less thick to thicker. Looking at the MODIS 40 class image this seems to correspond to the dark brown region being segmented into one thickness class and the light brown region being segmented into another. The fact that there is one roughness class is expected as the dynamic range of the roughness values, as seen in Figure 8.35 is not the high. The interesting thing to note here is that MODIS seems to be implying the presence of two distinct thickness classes based on the MODIS 40 class image in Figure 8.36 (Left), RS2 seems to be implying the presence of one distinct roughness class. It could be argued that this constitutes information of a complimentary nature as both sensors are providing distinct information about the condition of the ice. If this hypothesis is true, then it can be stated that in this case MODIS is showing that the thickness of the landfast ice is varying from region to region while the surface roughness is staying nearly the same.

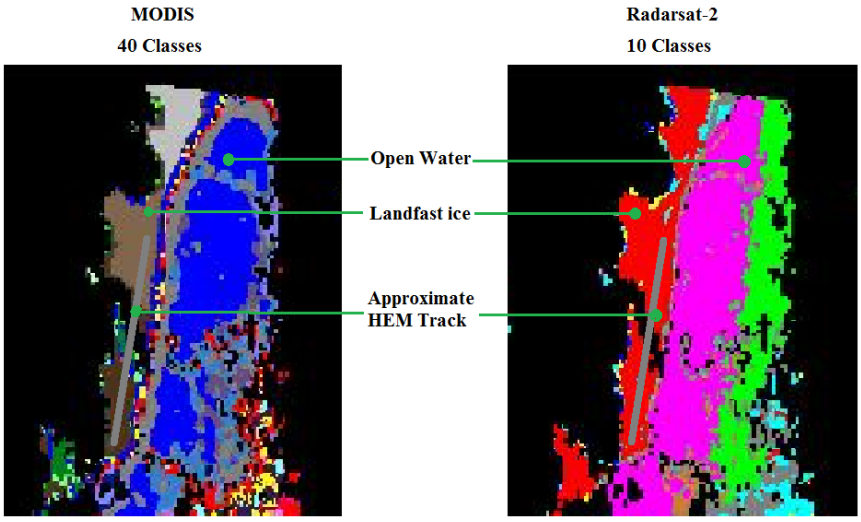

Figure 8.36: (Left) 40-class MODIS image, (Right) 10 class RS2 image. As can be seen the HEM track transverses two classes in the MODIS image and one class in the RS2 image. Note; the HEM track is approximately drawn on the two images, but it is highly believed this corresponds to the areas where the actual HEM flew over.

9 Conclusion

9.1 Summary

In this study, the complimentary nature of optical sensors and SARs, for the investigation of thin sea ice is explored. The degree to which these two sensors complement each other, was addressed from two points of view.

The first point of view, was concerned with the similarities in segmentation results that could be determined from each sensor. This involved looking at segmented images of scenes that contained thin sea ice in Storfjorden, and trying to determine if both sensors could distinguish similar ice types and under what conditions could these similar ice types be distinguished. The second point of view was concerned with the differences in segmentation results. This involved examining the same segmented images of Storfjorden and attempting to determine for what known ice classes does SAR and optical sensors arrive at a different number of classification results. In this way, it was hoped that one sensor could provide information that the other sensor could not.

This study began by choosing data that was acquired at the same time, or nearly the same time, obtained over Storfjorden, in the Svalbard archipelago, from the MODIS and RS2 sensors, at periods of low cloud cover. A variety of operational data types from RS2 were used. These included data in the form of dual-pol ScanSAR Narrow mode and dual-pol ScanSAR Wide mode. QuadPol data was also downloaded and used in a comparison against MODIS data for completeness. Data from a HEM campaign was also incorporated for the purpose of determining if the thickness of sea ice and its roughness are in some way related.

This work began by choosing a convenient segmentation algorithm to classify the ice types observed by both sensors. It was found that the Mixture of Gaussian method with MRF smoothing provided satisfactory results as well as flexibility in deriving segmented images.

In the preprocessing stage, all data was georeferenced and resampled to a common resolution in order to derive images from both sensors that were spatially aligned. Additional, sensor specific operations were implemented on each data set as required. It is interesting to note the fundamental importance of aligning data from different sensors to a common map projection. For the purposes of comparing data from different sources, or fusing data from different sources, this step is of vital importance as imagery from these two sources have different imaging geometries and resolutions. With the exception of multilooking the SAR data, and deriving the ScanSAR features, all preprocessing was conducted entirely in ENVI.

In this study, a set of 6 polarimetric features were extracted from the QuadPol data and 3 features from the ScanSAR data. These features were chosen as they were reported to give good segmentation results for sea ice by (Moen, et al., 2013). The MODIS data was inspected for any corrupted bands, which were then discarded. The resulting bands that captured the full view of the scene in question were projected to another space via PCA. Only the first few PCs were kept as it was discovered they contained most of the variance of the entire data set.

This study was comprised of 4 comparisons. The first two are regarded as the most interesting as they aimed to compare MODIS to the operational SAR modes; ScanSAR Wide and ScanSAR Narrow. In the comparison between ScanSAR narrow and MODIS it was found that MODIS produced segments that were localized to the major ice types that were known to be in the Fjord at the time of data acquisition. Major ice types being landfast ice, drift ice, leads etc. RS2 produced segments that were independent of

these major ice types. Using prior knowledge about Storfjorden, it was determined that the dominant scattering mechanism was due to the surface roughness of this ice material. In this way, it can be argued that MODIS was providing information related to the thickness of the sea ice and RS2 was providing information related to the roughness of the material. As the locations of these clusters did not seem to correlate with well with each other it was determined that for this case the two sensors were measuring two completely different aspects related to the sea ice. A case can be made, however, that both sensors detected the open leads that were present at the time of data acquisition. As it is strongly believed these leads were mainly comprised of open water, it is highly possible, given the results seen, that both SAR and MODIS are sensitive to areas of open water in contrast to sea ice.

This was confirmed in the second comparison. This comparison was between MODIS and ScanSAR Wide. When the clustered images were examined a clear distinction between open water and sea ice was seen. This was seen for a low number of clusters. When the MODIS data was segmented to 30 clusters, it was found that the scenes became almost identical when compared to the RS2 10 class image. When the MODIS image was segmented to 40 classes, the areas of sea ice specifically displayed further segmentation. This ion some way demonstrates that MODIS is capable of providing complimentary information to SAR.

This was demonstrated in the fourth comparison between the Hem thickness vales and the derived roughness characteristic. A scatter plot of between these two quantities was shown. In this plot, the dynamic ranges of both quantities are displayed. As can be seen the range of roughness values is quite small but the range of thickness values is relatively large. In fact looking at a graph for the ice thickness values an upwards trend was observe from one side of the profile to the other. Because of this, the area in the image where the HEM flew over was able to be further segmented in the MODIS image. This implies that for this case, MODIS can provide information beyond what RS2 is capable of providing.

The third comparison, between MODIS and RS2 demonstrates the interpretative power of RS2 when in QuadPol mode. When segmented, images provided by this imaging mode were able to distinguish ground features. While the resolution of MODIS was too coarse to derive any meaningful information, it should be noted that it is possible to distinguish between water and sea ice from both MODIS and RS2 QuadPol mode.

As can be seen by the comparisons performed in this thesis, it can be seen that, MODIS and RS2, can provide complimentary information to the user.

9.2 Future Work

In order to derive more meaningful results from RS2 the banding effect that corrupts the ScanSAR images needs to be addressed. As this is currently an active area of research this is a possible line of enquiry to take this research.

As this thesis compared classification results using a qualitative, subjective method. A quantitative method that compares these two data types could be further developed. In section 7.5, it was suggested to use a similarity measure such as the Jaccard coefficient. As some of the surface types that were derived in both MODIS and RS2 are believed to be identical, areas of open water for example, a measure such as this could provide a numerical value to compare between MODIS and RS2 at different levels of clustering.

As stated previously, fusion of optical and SAR data for the investigation of sea ice in the arctic appears to be an underdeveloped area of research, possibly due to the prevalence of cloud cover and the polar night. Attempting to classify thin sea ice images based on fused data is another possible line of research.

10 References

Ackerman S.A. [et al.] Discriminating clear sky from clouds with MODIS [Journal] // J. Geophys. Res. - December 27, 1998. - D24 : Vol. 103. - pp. 32,141-32,157.

Adams S. [et al.] Daily thin-ice thickness maps from MODIS thermal infrared imagery [Journal] // IEEE. - 2012.

Allison I., Brandt R.E. and Warren S.G. East Antartic Sea Ice: Albedo, Thickness Distribution, and Snow Cover [Journal] // Journal of Geophysical Research. - 1993. - C7 : Vol. 98. - pp. 12417-12429.

Bernstein R. [et al.] Analysisand processing of Lansat-4 sensor data using advanced image processing techniques and technologies [Journal] // IEEE Transaction on Geoscience and Remote Sensing. - 1984. - Vols. GE-22. - pp. 192-221.

Bogdanov A.V. [et al.] Multisensor approach to automated classification of sea ice image data [Journal] // Ieee Transactions on Geoscience and Remote Sensing. - 2005. - 7 : Vol. 43. - pp. 1648-1664.

Campbell J.B. Spatial correlation effects upon accuracy of supervised classification of land cover [Journal] // Photogrammetric Engineering and Remote Sensing. - 1981. - Vol. 47. - pp. 355-363.

Carsey F.D. Microwave Remote Sensing of Sea Ice [Book]. - [s.l.] : American Geophysical Union, 1992.

Chuvieco E. and Huete A Fundamentals of Satellite Remote Sensing [Book]. - [s.l.] : Taylor and Francis Group, 2010.

Clausi D.A. and Yue B. Comparing cooccurrence probabilities and Markov random fields for texture analysis of SAR sea ice imagery [Journal] // Ieee Transactions on Geoscience and Remote Sensing. - 2004. - 1 : Vol. 42. - pp. 215-228.

Clausi D.A. Comparison and fusion of co-occurrence, Gabor and MRF texture features for classification of SAR sea-ice imagery [Journal] // Atmosphere-Ocean. - 2001. - 3 : Vol. 39. - pp. 183-194.

Clement V. [et al.] Interpretation of remotely sensed images in a context of multisensor fusion using a multispecialist architecture [Journal] // Geoscience and Remote Sensing, IEEE Transactions on. - 1993. - 4 : Vol. 31. - pp. 779-791.

Cliff A.D. and Ord J.K. Spatial Autocorrelation [Journal]. - London:Pion : [s.n.].

Coakley J.A. Reflectance and albedo, surface. [Book Section] // Encyclopedia of the Atmosphere / ed. Holton J.R. and Curry J.A.. - [s.l.] : Academic Press, 2003.

Deng H. and Clausi D.A. Unsupervised segmentation of synthetic aperture radar sea ice imagery using a novel Markov random field model [Journal] // Ieee Transactions on Geoscience and Remote Sensing. - 2005. - 3 : Vol. 43. - pp. 528-538.

Divine D.V. [et al.] Atmospheric-driven state transfer of shore-fast ice in the northeastern Kara Sea [Journal]. - [s.l.] : Journal of Geaophysical Research, 2005. - C09013 : Vol. 110.

Doulgeris A.P. A Simple and Extendable Segmentation Method for Multi-Polarisation SAR Images [Conference] // Proc. POLinSAR. - Frascati, Italy : [s.n.], 2013. - p. 8.

Doulgeris A.P. An Automatic U-distribution and Markov Random Field Segmentation Algorithm for PolSAR Images [Journal]. - [s.l.] : IEEE, 2014.

Doulgeris A.P. and Eltoft T. PolSAR image segmentation — Advanced statistical modelling versus simple feature extraction [Conference] // 2014 IEEE Geoscience and Remote Sensing Symposium. - 2014.

Doulgeris A.P. and Eltoft T. Scale Mixture of Gaussian Modelline of Polarimetric SAR data [Journal] // EURASIP Journal on Advances in Signal Processing. - 2010.

Drinkwater M.R. Limex'87 ice surface characteristics: Implications for c-band sar backscatter signatures. [Journal] // IEEE Transcations on Geoscience and Remote Sensing. - 1989. - 5 : Vol. 27. - pp. 501-513.

Eltoft T. [et al.] Imaging sea ice structure by remote sensing sensors [Conference] // Proc. of Port and Ocean Engineering under Arctic Conditions. - 2015.

Frey R.A. [et al.] Cloud Detection with MODIS. Part 1: Improvements in the MODIS Clou Mark for Collection 5 [Journal]. - [s.l.] : J. Atmos. Oceanic Technol.. - 7 : Vol. 25. - pp. 1057 - 1072.

Galley R.J. [et al.] Replacement of multiyear sea ice and changes in the open water season duration in the Beaufort Sea since 2004 [Journal] // Journal of Geophysical Research. - 2016. - 3 : Vol. 121. - pp. 1806-1823.

Geiger C. [et al.] On the uncertainty of sea-ice isostasy [Journal] // Annals of Glaciology. - 2015. - 69 : Vol. 56.

Geldsetzer T. and Yackel J.J. Sea ice type and open water discrimination using dual co-polarized C-band SAR [Journal] // Canadian Journal of Remote Sensing. - 2009. - 1 : Vol. 35. - pp. 73-84.

Gill J. and Yackel J. Evaluation of C-band SAR polarimetric parameters for discrimination of first-year sea ice types [Journal] // Can. J. Remote Sens.. - 2012. - Vol. 38. - pp. 306-323.

Groves J.E. and Stringer W.J. The Use of AVHRR Thermal Infrared Imagery to Determine Sea Ice Thickness within the Chukchi Polynya [Journal] // Arctic. - 1991. - Vol. 44. - pp. 130-139.

Haarpainter Jorg and Gascard Jean-Claude Ice production and brine formation in Storfjorden, Svalbard [Journal] // Journal of Geophysical Research. - July 15, 2001. - C7 : Vol. 106. - pp. 14,001-14,013.

Haas C. [et al.] Airborne electromagnetic measurements of sea ice thickness: methods and applications [Book Section] // Arctic Sea Ice Thickness: Past, Present and Future / ed. Wadhams P., and G. Amanatidis. - [s.l.] : European Commission, Climate Change and Natural Hazards Series , 2007.

Haas C. Airborne EM sea-ice thickness profiling over brackish Baltic sea water [Conference] // Proceedings of the 17th international IAHR symposium on ice. - St.Petersburg,Russia : All-Russian Research Institute of Hydraulic Engineering (VNIIG), 2004. - Vol. 2. - pp. 12-17.

Haas C. and Jochmann P. Continuous EM and ULS thickness profiling in support of ice force measurement [Conference] // Proceedings of the 17th International Conference on Port and Ocean Engineering under Arctic Conditions, POAC '03. - Trondheim, Norway : [s.n.], 2003. - pp. 849-856.

Haas C. Evaluation of ship-based electromagnetic-inductive thickness measurements of summer sea-ice in the Bellingshausen and Amundsen Seas, Antartica [Journal] // Cold Regions Science and Technology. - 1998. - Vol. 27. - pp. 1-16.

Haas C., Hendricks S. and Doble M. Comparison of the sea-ice thickness distribution in the Lincoln Sea and adjacent Arctic Ocean in 2004 and 2005 [Journal] // Annals of Glaciology. - 2006. - 1 : Vol. 44. - pp. 247-252.

Haas C., Rupp K.-H. and Uuskallio A. Comparison of along track EM ice thickness profiles with ship performance data [Conference] // Proceedings of the 15th International Conference on Part and Ocean Engineering under Arctic Conditions. - Espoo,Finland : [s.n.], 1999. - pp. 343-353.

Hajnsek I. and Papathanassiou K. Estimation of surface characteristics, polarimetric SAR data processing and educational tool V4.0 [Report] / ESA, Paris. - 2005.

Hall D.L. and Llinas J. An introduction to multisensor data fusion [Conference] // Proceedings of the IEEE. - 1997. - Vol. 85(1). - pp. 6-23.

Hall Dorothy K. [et al.] Sea Ice Surface Temperature Product from MODIS [Journal] // IEEE Transactions on Geoscience and Remote Sensing. - May 2004. - 5 : Vol. 42.

Hallikainen Martti and Winebrenner Dale, P. The Physical Basis for Sea Ice Remote Sensing [Book Section] // Microwave Remote Sensing of Sea Ice / ed. Carsey Frank D.. - [s.l.] : American Geophysical Union, 1992.

Haverkamp D., Soh L.K. and Tsatsoulis C. A COMPREHENSIVE, AUTOMATED APPROACH TO DETERMINING SEA-ICE THICKNESS FROM SAR DATA [Journal] // Ieee Transactions on Geoscience and Remote Sensing. - 1995. - 1 : Vol. 33. - pp. 46-57.

Haykin S. [et al.] Remote Sensing of Sea Ice and Icebergs [Book]. - [s.l.] : John Wiley and Sons, Inc., 1994.

Hecht E. Optics [Book]. - [s.l.] : Addison Wesley, 2002. - 4th.

Hibler III W.D. Removal of aircraft variations from laser profiles of the Arctic ice pack [Journal] // Journal of Geophysical Research. - 1972. - 36 : Vol. 77. - pp. 7190-7195.

Ho J. The implications of Arctic sea ice decline on shipping [Journal] // Marine Policy. - 2009. - pp. 713-715.

Hunke E.C. [et al.] The multiphase physics of sea ice: a review for model developers [Journal]. - [s.l.] : The Cryosphere, 2011. - Vol. 5. - pp. 989-1009.

IPCC Climate Change 2007: Synthesis Report [Report] / WMO. - [s.l.] : Intergovernmental Panel on Climate Change, 2008.

Iqbal M. [et al.] Kalman filter for removal of scalloping and inter-scan banding in scansar images [Journal] // Progress in Electronics Research. - 2012. - Vol. 132. - pp. 443-461.

Johannessen O. [et al.] Remote Sensing of Sea Ice in teh Northern Sea Route: Studies and Applications [Book]. - [s.l.] : Springer, 2007.

Johansson A.M. [et al.] Combined observations of Arctis sea ice with near-coincident co-located X,C and L-band SAR satellite sensing and helicopter-borne measurements [Journal] // Journal of Geophysical Research. - 2017. - Vol. 122.

Jolliffe I.T. Principal Component Analysis [Book]. - [s.l.] : Springer, 2002.

Joshi N. [et al.] A Review of the Application of Optical and Radar Remote Sensing Data Fusion to Land Use Mapping and Monitoring [Journal] // Remote Sensing. - 2016. - 70 : Vol. 8.

Kim Y. [et al.] Towards identification of optimum radar parameters for sea ice monitoring [Journal] // Journal of Glaciology. - 1985. - 109 : Vol. 31. - pp. 214-219.

Kovacs A. and Holladay J.S. Sea-ice thickness measurements using a small airborne electromagnetic sounding system. [Journal] // Geophysics. - 1990. - Vol. 55. - pp. 1327-1337.

Kovacs A., Valleau N.C. and Holladay J.S. Airborne electromagnetic sounding of sea ice thickness and sub-ice bathymetry. [Journal] // Cold Regions Science and Technology. - 1987. - Vol. 14. - pp. 289-311.

Launiainen J. and Vihma T. Derivation of Turbulent Surface Fluxes - An Iterative Flux-Profile Method Allowing Arbitrary Observing Heights [Journal]. - [s.l.] : Envirnomental Software, 1990. - 3 : Vol. 5.

Le Moigne J., Netanyahu N.S. and Eastman R.D. Image Registration for Remote Sensing [Book]. - [s.l.] : Cambridge University Press, 2011.

Lindsay B.G. and Basak P. Multivariate Normal Mixtures: A Fast Consistent Method of Moments [Journal] // American Statistical Association. - 1993. - 422 : Vol. 88.

Liu M. [et al.] PCA-based sea-ice image fusion of optical data by HIS transform and SAR data by wavelet transform [Journal] // Acta Oceanologica Sinica. - 2014. - 3 : Vol. 34. - pp. 59-67.

Lu Z, Qu Y and Qiao S. Geodesy: Introduction to Geodetic Datum and Geodetic Systems [Book]. - [s.l.] : Springer, 2014.

Maillard P., Clausa D.A. and Deng H.W. Operational map-guided classification of SAR sea ice imagery [Journal] // Ieee Transactions on Geoscience and Remote Sensing. - 2005. - 12 : Vol. 43.

MANICE Manual of Standard Procedures for Observing and Reporting Ice Conditions [Book]. - [s.l.] : Canadian Ice Service, 2005.

Massom R. and Comiso J.C. The classicication of Arctic Sea ice types and the determination of surface temperature using advanced very high resolution radiometer data [Journal] // Journal of Geophysical Research. - March 15, 1994. - C3 : Vol. 99. - pp. 5201-5218.

Maykut G.A., and Untersteiner N. Some Results from a Time-Dependent Thermodynamic Model of Sea Ice [Journal] // Journal of Geophysical Research. - February 20, 1971. - 6 : Vol. 76.

McCandless Samuel W. and Jackson Christopher, R. Principles of Synthetic Aperture Radar [Book Section] // Synthetic Aperture Radar Marine User's Manual / book auth. Apel C. Jackson and J. R.. - Washington DC, USA : U.S. Department of Commerce, National Oceanic and Atmospheric Administration, 2004.

McLachlan G. and Peel D. Finite Mixture Models [Book]. - [s.l.] : John Wiley & Sons, Inc., 2000.

Moen M.-A.N. [et al.] Comparison of feature based segmentation of full polarimetric SAR satellite sea ice images with manually drawn ice charts [Journal] // The Cryosphere Discuss. - 2013. - Vol. 7. - pp. 1693–1705.

Moreira Alberto [et al.] A Tutorial on Synthetic Aperture Radar [Article] // IEEE Geoscience and Remote Sensing Magazine. - 2013. - p. 7.

Multala J.H. [et al.] An airborne electromagnetic system on a fixed wing aircraft for sea ice thickness mapping. [Journal] // Cold regions science and technology. - Vol. 24. - pp. 355-373.

NASA MODIS Level 1B Product User's Guide [Report] / NASA/Goddard Space Flight Center . - 2009.

Nishihama M. [et al.] MODIS Level 1A Earth Location: Algorithm Theoretical Basis [Report] / Laboratory for Terrestrial Physics ; NASA Goddard Space Flight Center. - Greenbelt, MD : [s.n.], 1997.

Ochilov S. and Clausi D.A. Operational SAR Sea-Ice Image Classification [Journal] // Ieee Transactions on Geoscience and Remote Sensing. - 2012. - 11 : Vol. 50. - pp. 4397-4408.

Ohno Y. Spectral Color Measurement [Book Section] // Colorimetry : Understanding the CIE System / ed. Schanda J.. - [s.l.] : John Wiley and Sons,Inc., 2007.

Onstott R.G. Sar and scatteromter signature of sea ice [Journal] // Geophysical Monograph Series. - 1992. - Vol. 68. - pp. 73-104.

Onstott Robert G. and Shuchman Robert A. SAR Measurements of Sea Ice [Book Section] // Synthetic Aperture Radar Marine Users Manual / ed. Jackson Christopher R. and Apel John R.. - [s.l.] : NOAA, 2004.

Paterson J. [et al.] In situ measurements of micro-scale surface roughness of sea ice [Journal] // Arctic. - 1991. - 5 : Vol. 44. - pp. 140-146.

Pearson K. Contributions to the theory of mathematical evolution [Journal] // Philosophical Transactions of the Royal Society of London A. - 1894. - Vol. 185. - pp. 71-110.

Perovich D.K. Observetaions of the polarization of light reflected from sea ice [Journal] // Journal of Geophysical Research. - 1998. - C3 : Vol. 103. - pp. 5563-5575.

Peterson A.K. Observations of brine plumes below Arctic sea ice [Journal] // Ocean Science Discussions. - 2017.

Peterson I.K., Prinsenberg S.J. and Holladay J.S. Observations of sea ice thickness, surface roughness and ice motion in Amundsen Gulf [Journal] // JOURNAL OF GEOPHYSICAL RESEARCH. - 2008. - C06016 : Vol. 113.

Petrich Chris and Eicken Hajo Growth, structure and properties of sea ice [Book Section] // Sea Ice. - 2010.

Pohl C. and Van Genderen J.L. Review article Multisensor image fusion in remote sensing: concepts, methods and applications [Journal] // International journal of remote sensing. - 1998. - 5 : Vol. 19. - pp. 823-854.

Prakash Anupma Thermal Remote Sensing: Concepts, Issues and Applications [Conference] // International Archives of Photogrammetry and Remote Sensing. - Amsterdam : [s.n.], 2000. - Vol. Part B1 XXXIII.

Preußer A. [et al.] Thin-ice dynamics and ice production in the Storfjorden polynya for winter seasons 2002/2003–2013/2014 using MODIS thermal infrared imagery [Journal] // The Cryosphere. - 2015. - Vol. 9. - pp. 1063-1073.

Raney R.K. A perspective on compact polarimetry [Journal] // IEEE Geoscience and Remote Sensing Newsletter. - 2011. - Vol. 160. - pp. 12-18.

Rees W.G. Infrared emissivities of Arctic land cover types [Journal] // International Journal of Remote Sensing. - 1993. - 5 : Vol. 14.

Sandvin S., Johannessen O.M. and Kloster K. Sea ice monitoring by remote sensing [Book Section] // Encyclopedia of Analytical Chemistry. - 2006.

Scheuchl B. [et al.] Automated sea ice classification using spaceborne polarimetric SAR data [Journal] // IGARSS. - 2001. - pp. 3117-3119.

Serreze M.C. and Francis J.A. The Arctic on the fast track of change [Journal] // Weather. - 2006. - 3 : Vol. 61.

Simone G. [et al.] Image fusion techniques for remote sensing applications [Journal] // Information Fusion. - 2002. - 1 : Vol. 3. - pp. 3-15.

Snyder J.P. Map Projections-A Working Manual [Book]. - [s.l.] : U.S. Geological Survey Professional Paper 1395, 1987.

Soh L.K. [et al.] ARKTOS:An intelligent system for SAR sea ice image classification [Journal] // Ieee Transactions on Geoscience and Remote Sensing. - 2004. - 1 : Vol. 42. - pp. 229-248.

Souri A.H. and Azizi A. Removing Bowtie Phenomenon by Correction of Panoramic Effect in MODIS Imagery [Journal] // International Journal of Computer Applications . - April 2013. - 3 : Vol. 68. - pp. 0975 - 8887.

Theodoridis S. and Koutroumbas K. Pattern Recognition [Book]. - [s.l.] : Elsevier Inc., 2009.

Thomsen B., Hghiem S. and Kwok R. Polarimetric C-band SAR observations of sea ice in the Greenland Sea [Journal] // Proc. IGARSS. - 1998. - pp. 2502-2504.

Townshend J.R.G. The spatial resolving power of Earth resources satelites: A review [Report] / Goddard Spaceflight Center ; NASA. - Greenbelt,MD : [s.n.], 1980.

Varshney P.K. Multisensor data fusion [Journal] // Electronics and Communication Engineering Journal. - 1997. - 6 : Vol. 9. - pp. 245-253.

Vihma T. Effects of arctic sea ice decline on weather and climate: A review [Journal] // Surveys in Geophysics. - 2014. - 5 : Vol. 31. - pp. 1175-1214.

von Saldern C. [et al.] Analysis of Sea Ice Roughness and Thickness Variation for Improvement of SAR Ice Type Classification [Conference] // Proceedings of the 2004 Envisat & ERS Symposium / ed. Lacoste H. and Ouwehand L. - 2004.

Vulpiani G. [et al.] On the use of Dual-polarized C-Band radar for operational rainfall retrieval in mountainous areas [Journal] // Americal Meteorological Society. - 2012.

Wang X., Key J.R. and Liu Y. A thermodynamic model for estimating sea and lake ice thicjness with optical satellite data [Journal] // Journal of Geophysical Research. - 2010. - C12035 : Vol. 115.

Willmes S and Heinemann G. Pan-Arctic lead detection from MODIS thermal infrared imagery [Journal] // ANNALS OF GLACIOLOGY. - 2015. - 69 : Vol. 56. - pp. 29-37.

Willmes S and Heinemann G. Sea-IceWintertime Lead Frequencies and Regional Characteristics in the Arctic, 2003-2015 [Journal] // REMOTE SENSING. - Jan 2016. - 1 : Vol. 8.

World Meteorological Organization WMO Sea Ice Nomenclature. [Report] / WMO. - Geneva : [s.n.], 1970.

Wright R. [et al.] Automated volcanic eruption detection using MODIS [Journal] // Remote Sensing of Envirnoment. - [s.l.] : Elsevier, 2002. - Vol. 82. - pp. 135-155.

Xiong X and Che Nianzeng,Barnes,W. Terra MODIS On-Orbit Spatial Characterization and Performance [Journal] // IEEE Transaction on Geoscience and Remote Sensing. - 2005. - 2 : Vol. 43.

Yu Y. and Rothrock D.A. Thin ice thickness from satellite thermal imagery [Journal] // Journal of Geophysical Research. - November 15, 1996. - C10 : Vol. 101. - pp. 25,753-25,766.

Yu Y., Rothrock D.A. and Zhang J. Thin ice impacts on surface salt flux and ice strength: Inferences from advanced very high resolution radiometer [Journal] // Journal of Geophysical Research. - 2001. - C7 : Vol. 106. - pp. 13975-13988.

Zakhvatkina N. [et al.] Operational algorithm for ice–water classification on dual-polarized RADARSAT-2 images [Journal] // The Cryosphere. - 2017. - Vol. 11. - pp. 33-46.

Zakhvatkina N.Y. [et al.] Classification of Sea Ice Types in ENVISAT Synthetic Aperture Radar Images [Journal] // Ieee Transactions on Geoscience and Remote Sensing. - 2013. - 5 : Vol. 51. - pp. 2587-2600.